Hierarchical Self-Assembly of Nanoparticles Using Reversible Addition-Fragmentation Chain-Transfer Block Copolymers

by

Fraser Burns
B. Sc., Mount Allison University, 2013

A Thesis Submitted in Partial Fulfillment
of the Requirements for the Degree of

MASTER OF SCIENCE

in the Department of Chemistry

Supervisory Committee

Hierarchical Self-Assembly of Nanoparticles Using Reversible Addition-Fragmentation Chain-Transfer Block Copolymers

by

Fraser Burns
B.Sc., Mount Allison University, 2013

Supervisory Committee

Dr. Matther Moffitt, Department of Chemistry
Supervisor

Dr. Alexandre Brolo, Department of Chemistry
Departmental Member

Abstract

Supervisory Committee
Dr. Matthew Moffitt, Department of Chemistry
Supervisor
Dr. Alexandre Brolo, Department of Chemistry
Departmental Member

The hierarchical self-assembly of cadmium based quantum dots through the use of RAFT block copolymers have been investigated. The formation of cadmium selenide quantum dots within the core of tetrablock RAFT copolymers in three different solvents, dioxane, THF and DMF was investigated experimentally and computationally. It was determined that aggregation of the PAA core-forming blocks prevented the formation of stable dispersions of the CdSe quantum dots in DMF and THF, while dioxane was found to be a suitable solvent. The cadmium selenide quantum dots exhibit a near band-edge emission centered at 520 nm with a hydrodynamic diameter of 20 nm.

The assembly of RAFT copolymer encapsulated cadmium sulfide quantum dots with gold nanoparticles was explored. It was determined that with increasing concentration of gold nanoparticles, there was an increase in emission amplification. Subsequent self-assembly into large compound micelles with PS-*b*-PAA block copolymer was investigated and determined to form large, water-soluble compound micelles.

Table of Contents

List of Tables

List of Figures

List of Abbreviations

-*b*- - block
λ_{max} – Wavelength of the maximum of a peak
λ_{thresh} – Wavelength of the quantum dot band edge absorption threshold
A_2 – Second virial coefficient
ATRP – Atom transfer radical polymerization
AuNP – Gold nanoparticle
c_0 – Initial solids concentration
CRP – Controlled radical polymerization
CTA – Chain transfer agent
D_h/r_h – hydrodynamic diameter/radius
DLS – Dynamic light scattering
dn/dc -
DNA – Deoxyribonucleic acid
D_{thresh} – Diameter of quantum dots from band-edge calculations
EA – Emission amplification
E_F – Fermi Energy
FI_{corr} – Corrected fluorescence intensity
$F_{QDM\text{-}AuNP}$ – Blending ratio of QDM-AuNPs compared to total solids content
LSPR/SPR – Localized surface plasmon resonance
MALDI-TOF – Matrix assisted laser desorption ionization – time of flight mass spectrometry
MD – Molecular dynamics
M_n – Number averaged molecular weight
M_w – Weight averaged molecular weight
NMP – Nitroxide mediated polymerization
PAA – Poly(acrylic acid)
PDI – Polydispersity index
PL - Photoluminescence
PS – Polystyrene
QD – Quantum dot
QDM – Quantum dot micelle
QDCM – Quantum dot compound micelle
QD-AuCM – Quantum dot – gold nanoparticle compound micelle
RAFT – Reversible addition-fragmentation chain-transfer polymerization
r_B – Bohr radius
R_g – Radius of gyration
R_{GNP} – Ratio of gold nanoparticles per micelle
RI – Refractive index
r_{NP} – Nanoparticle radius
SEC-MALS – Size exclusion chromatography – multiple angle light scattering
SLS – Static light scattering
TEM – Transmission electron microscopy
TTC - Trithiocarbonate

Acknowledgments

I would like to give my sincere thanks to **Dr. Matthew Moffitt** for his guidance and support over the course of my degree. He has taught me how to be an observant, and rational scientist while also serving as one of the few Maritimers in the department for me to talk with! Thank you for everything.

I would especially like to thank my parents, **Paul and Gail Burns**, and my siblings **Owen and Emily Burns** for their support throughout my life. I would not be the person I am today without them and am eternally in their debt. Beyond my immediate family I am deeply appreciative of all my Aunts, Uncles, and Cousins who have been a great source of laughter, insight and companionship.
Additionally, I would like to thank the following people:
-The Moffitt research group (past and present) for valuable conversations and companionship, this includes:

- **Dr. Aman Bains** who introduced me to the research group and provided me with many insights into research and life.
- **Sundiata Kly**, for his upbeat demeanor and insight.
- **Brian Coleman** for his help on many different aspects of my research work.
- **Dr. Tânia Ribeiro** for being a constant source of support and knowledge on my project, with my work in Portugal and for sample preparation.
- **Ruyao Chen, Yimeng Cao, Alex Leung, and Abby Xu** as well as many undergraduate students for making the long hours in the lab seem not so long!

- My friends **Paul Gray, Eric Janusson, Elvis Ting, Corey Sanz, Erica Hong, David Halley** (and for that matter most of the Grad Students in the department) for acting as constant sources of entertainment, insight and help.
- **Dr. Jose Paulo Farinha** at IST in Lisbon
- **Dr. Frank van Veggel** for numerous conversations across an incredibly wide range of topics, and providing perspective on many different aspects of research.
- **Dr. Alex Brolo** for serving on my supervisory committee as well as providing valuable insight on various aspects of my project
- **Dr. Reuven Gordon** from the department of Electrical and Computer Engineering
- **Andrew MacDonald** for his assistance with pretty much every piece of equipment I had to use.
- **Dr. Alan Taylor** who has served as a source of inspiration for patience when dealing with students.
- The Department of Chemistry staff and faculty for their help on many, many occasions.
- To anyone I have omitted/forgotten, my apologies, and thank you!

Chapter 1 - General Introduction

1.1. General Introduction

Control over the assembly of inorganic nanoparticles has been of interest in the scientific community in part because of their vast potential for the creation of new materials. These materials may be imparted with desirable physical properties, be it mechanical, electrical, optical, etc. based upon their constituent components. Control over these assemblies is typically classified into two primary methods of approach: top-down and bottom-up.[1] Top-down methods encompass any process which begins with macroscale materials and produces nanoscale structures; this comprises a variety of lithographic methods (chemical, photo, electro, etc.)[2–5] in addition to techniques such as microfluidics.[6–8] Alternatively, bottom-up methods begin with small molecules and through careful manipulation of the kinetic and thermodynamic parameters of the system, create the desired final product. Self-assembly utilizing bottom-up approaches are an important avenue of research as they typically do not require the costly specialized equipment commonly seen in top-down methods, in tandem with typically higher throughput relative to their top-down counterparts. Additionally, through careful understanding of the kinetic and thermodynamic parameters that govern these systems it is possible to generate a wide array of materials from fundamental building blocks. Bottom-up assembly methods can be used for nanoparticle synthesis and stabilization, forming spheres, rods, cubes, etc. and can subsequently dictate the assembly of these particles into superstructures.[9–12]

Block co-polymers are an increasingly popular approach to bottom-up self-assembly as a result of the myriad possible combinations of physical and chemical properties available to them through selective polymer selection. Of particular interest to

our group is the creation and use of polymer brush functionalized nanoparticles (PBNPs). PBNPs that are designed for controlled self-assembly can be divided into 3 categories: Type 1, Type 2 and Type 3.[13] Type 1 PBNPs are nanoparticles functionalized with isotropic, single component polymer brushes, *e.g.* gold nanoparticles functionalized with a polystyrene brush.[14,15] These particles typically form periodic nanoparticle arrays during self-assembly, with variable assemblies being made possible via the addition of additives, such as homopolymers or appropriate block copolymers. The manner in which these additives interact with PBNPs will be discussed in more detail in subsequent sections. Type 2 and Type 3 PBNPs are related in that both govern anisotropic particles. Type 2 PBNPs are functionalized with anisotropic brushes, wherein the distribution of the polymer chains about the surface results in anisotropic patterning with distinct chemical environments. Type 2 PBNPs may either be described as Janus – two faced – particles where the particles have two distinct regions on opposite hemispheres of the particle; or Patchy, where there are patches of different chemical environments around the surface of the PBNP.[16–18] Type 3 PBNPs meanwhile are functionalized with isotropic, multicomponent brushes that do not directly encode anisotropic nature on the surface chemistry of the particle; however, through a combination of chemical incompatibility, polymer flexibility, microphase separation or conformational changes can induce anisotropy in the particles.[13]

Controlled assemblies of nanoparticles, such as quantum dots (QDs) with gold nanoparticles (AuNPs), have been created by employing techniques such as biomolecular spacers[19–24], polymeric spacer (based around the PBNP functionality described above),[13,25–28] or template based methods,[29] among others. A major source of interest in these materials lies in the ability of the AuNPs, through their surface plasmon resonance,

to enhance the photoluminescence of the QDs. Conversely, it is possible to quench the quantum dot photoluminescence through chemical bonding or through non-radiative transmission of energy from the QD to the nanoparticle. This enhancement/quenching phenomenon is primarily predicated upon the spacing between the two components.[24,27,29] The spacing requirements for enhancement or quenching between the two components will vary based on the components themselves; this is due to the size dependent nature of QDs and AuNPs. Their size dependent nature is a result of a phenomenon known as the quantum confinement effect, details of which can be found in section 1.3. As a result of their nature, the individual components may be specifically synthesized to promote properties desired in the final assemblies. These systems have found use across a wide range of fields, with the most prominent being in sensing based applications such as pH, temperature, or chemical environment monitoring.[22–24,29,30]

Our research group has previously studied the assembly of gold nanoparticles and quantum dots utilizing a reversible addition-fragmentation chain transfer (RAFT) copolymer encapsulated quantum dots with gold nanoparticles.[27] Specifically, a symmetric poly(acrylic acid)-*block*-polystyrene-trithiocarbonate-polystyrene-*block*-poly(acrylic acid), PAA-*b*-PS-TTC-PS-*b*-PAA, RAFT copolymer was used as a reactor vessel for the formation of cadmium sulfide (CdS) quantum dots. These particles were then exposed to gold nanoparticles whereupon aminolysis was performed resulting in the cleavage of the TTC group, forming 2 thiol terminal groups capable of then binding the gold nanoparticles. It was determined that as a result of the length of the polymer chain (~20 nm in solution), the gold was kept at a sufficient distance to influence the emissive properties of the CdS quantum dots. At this distance it has been observed, both in this system and others[20,31,32]

that the surface plasmon of the gold nanoparticle is capable of interacting with the quantum dots in such a way as to enhance photoluminescence of the resulting system. The ability to control these interactions shows promising applications as sensors, in photonic devices, as biomarkers or probes.[27]

This thesis is comprised of a general introductory chapter (Chapter 1), two experimental chapters (Chapter 2 and 3) followed by a final chapter detailing conclusions and future work (Chapter 4). Chapter 1 will continue with an introduction of the various aspects of importance for this research: a discussion of polymers, the relevant subfields, and their properties; quantum dots and their properties; gold nanoparticles and surface plasmon resonance; and finally the goals of the thesis will be presented.

Chapter 2 will investigate my work on the formation of RAFT copolymer reverse-micelle encapsulated cadmium selenide quantum dot cores while the second half is work performed by our collaborators on the influence of solvent on the formation of reverse-micelles of the RAFT copolymer. The synthesis and characterization of the RAFT-CdSe micelles seeks to expand upon previous work[27] completed in our group with RAFT-CdS analogues. The CdSe variants will seek to demonstrate the general applicability of the RAFT reverse micelles as nanoreactors for the formation of cadmium based quantum dots. The second half of chapter 2 includes results on Size Exclusion Chromatography – Multiple Angle Light Spectroscopy (SEC-MALS) characterization and computational modelling of the RAFT copolymer within three different solvent systems. This work was completed by our collaborators in tandem with my research into the formation and characterization of CdSe micelles.

Chapter 3 will explore the formation of RAFT-CdS/AuNP compound structures to investigate emission amplification as a function of gold nanoparticle (AuNP) concentration. This builds upon previous work in our group[27] by working with a new RAFT copolymer, demonstrating the applicability of the system under different synthetic conditions. Subsequently this chapter will seek to investigate further self-assembly of the RAFT-CdS/AuNP system to form large compound micelles under a variety of experimental conditions based upon related work previously explored within our group.[25,26] The formation of compound micelles will result in water soluble dispersions of the RAFT-CdS/AuNP systems, with the potential for desirable photonic applications, such as stop-band filters.

1.2 Polymers

Polymers are large molecules composed of repeating units of covalently bonded small molecules (monomers).[33] The monomer units are typically referred to as *repeat units* following polymerization, while the number of repeat units that make up a polymer are known as the *degree of polymerization*. In the case where a polymer chain is comprised of only one monomer, the polymer is known as a *homopolymer*. In cases where the polymer is composed of two or more monomers the resulting polymer is known as a *copolymer*; the localization of these monomers within the chain gives rise to different categories of copolymer, *i.e.* block copolymer, alternating copolymer, random copolymer and graft copolymers (Figure 1-1). The chemical nature of these polymers will dictate subsequent terminologies, *e.g.* in the case of amphiphilic block copolymers, based on the relative block lengths, *star-like* or *crew-cut* micelles are generated for longer and shorter coronal block lengths respectively (Figure 1-2).

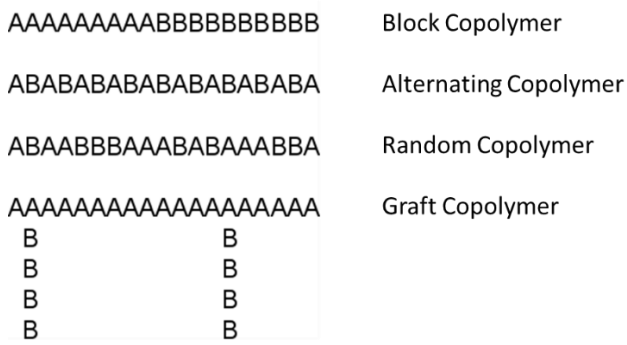

Figure 1-1. Four types of copolymers synthesized from monomers A and B. Adapted from ref. 75

A specific subset of block copolymers are generated through a controlled radical polymerization (CRP) technique: reversible addition-fragmentation chain-transfer (RAFT),[34] typically referred to as RAFT copolymers. RAFT is a desirable process as it is experimentally simpler than anionic polymerization, can accommodate a wide array of monomers and can be used to generate amphiphilic block copolymers.[34] The RAFT polymerization method can generate polymers with low polydispersity indexes (PDI) as well as additional functionality based on the monomers in question and the chain transfer agent (CTA) employed. For the purposes of this thesis, amphiphilic tetrablock RAFT copolymers are generated using a trithiocarbonate (TTC) CTA to form the tetrablock copolymer PAA-*b*-PS-TTC-PS-*b*-PAA (more details in Chapter 2). The TTC group is employed for this work to provide a thiol terminus group on the PS coronal chains following aminolysis with 1-hexylamine.

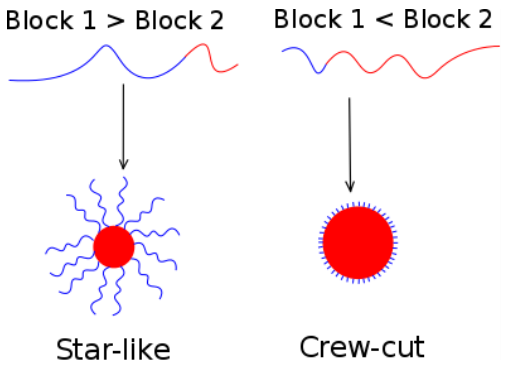

Figure 1-2. Cartoon diagram showing the formation of star-like and crew-cut micelles based on initial relative block copolymer lengths

1.2.1. Molecular Weight Distribution

Polymer synthesis differs from that of small molecule synthesis in that for a given polymer sample preparation, the product will contain a distribution of different molecular weights. The nature of this sample distribution arises from the random nature of most polymerization reactions themselves, e.g. side reactions that do not grow the chains, termination steps, etc. and as such the individual polymer chains will not grow at the same rate.[35] As a result of this aspect of polymer samples, two common types of averages are used to describe the average molecular weight in a sample comprised of a distribution of molecular weights; a weight averaged molecular weight (M_w) and a number averaged molecular weight (M_n). The weight average molecular weight refers to the average polymer molecular weight by mass, whereas the number average molecular weight refers to the molecular weight with the highest number of chains (see Figure 1-3).

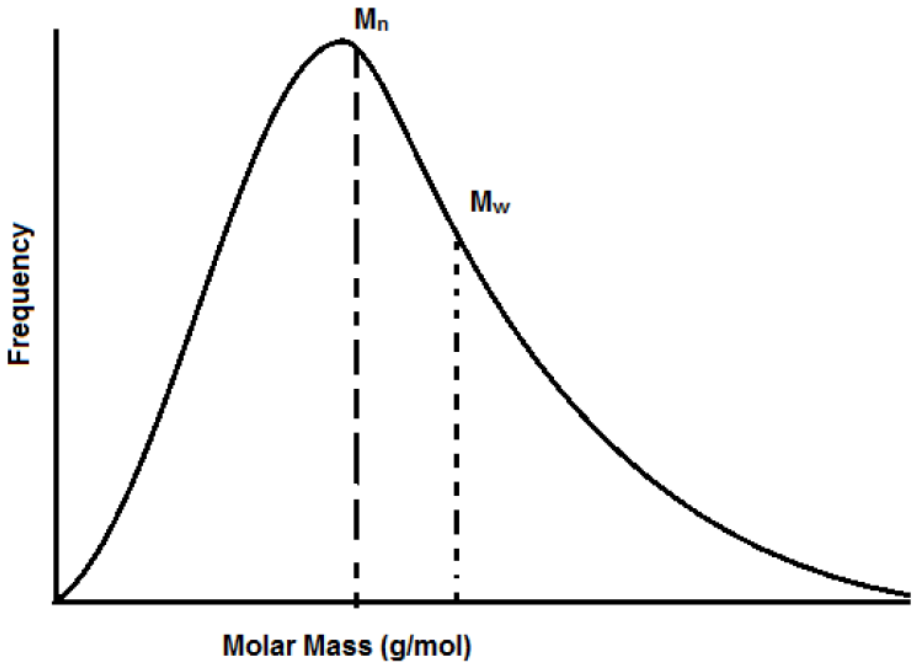

Figure 1-3. Representative diagram of the difference between Mw and Mn based on the molar mass distribution of a theoretical polymer. Image from Ref. 78.

The M_n is defined by equation 1.1:

$$M_n = \frac{\Sigma N_i M_i}{\Sigma N_i} \tag{1.1}$$

Where N_i is the number of polymer chains of molecular weight M_i. This value is typically determined through techniques that measure the colligative properties of samples, *e.g.* boiling point elevation/freezing point depression, and osmotic pressure.[35] The M_w of a sample is calculated from measurements sensitive to the size of the polymers in a given sample, *e.g.* light scattering, gel permeation chromatography/size exclusion chromatography, MALDI-TOF mass spectrometry. M_w is defined by equation 1.2:

$$M_w = \frac{\Sigma W_i M_i}{\Sigma W_i} = \frac{\Sigma N_i M_i^2}{\Sigma N_i M_i} \tag{1.2}$$

W_i is the weight of all molecules of all the species i of molar mass M_i, N_i is the same as in equation 1.1. The polydispersity index of a polymer sample, gives an indication of the distribution of particles within the sample. It should be noted that the PDI is defined by equation 1.3:

$$PDI = \frac{M_w}{M_n} \tag{1.3}$$

Samples with a PDI = 1 will contain only polymer chains of one molecular weight, or conversely the same number of repeat units, *i.e. monodisperse*. The majority of synthetic polymers have PDI values greater than 1 as a result of their synthetic process. In order to obtain consistent sample response from self-assembly it is key to work with samples of low PDI. This requirement is a function of the polymer thermodynamics which are heavily influenced by the relative lengths of polymer blocks, *e.g.* in a sample with high PDI, the larger (and longer) blocks will behave differently in solution compared to their shorter counter parts, the reasoning behind this will be examined in section 1.2.2. There has been a keen interest into the development of synthetic methods for control over the macromolecular structure, weight distribution, composition and architecture of polymers.

Of particular interest is the process of reversible addition-fragmentation chain transfer polymerization. The RAFT process is a type of living free radical polymerization, this means that the active end of the polymer chains is a free radical, and that polymerization termination is synthetically precluded. This technique utilizes a chain transfer agent (CTA) as a means to mask the radical end of the polymer chain from undergoing termination (combining with another free radical ending chain growth). The ability for these CTA groups to reversibly deactivate propagating radicals, and thereby rendering the living chains into a semi-dormant form undergoing rapid equilibrium

between active and dormant chains. As a result of this process, molecular weights can increase linearly with conversion between the two forms which results in narrow molecular weight distributions.[36]

1.2.2. Block Copolymer Thermodynamics of Micellization

Of particular interest is the field of block copolymers due to their ability to provide areas of different functionality based on block structure. Block copolymer notation is based around the composition of the copolymer, in the case of a polymer containing two blocks, *e.g.* polystyrene and poly(acrylic acid), the resulting block copolymer would be termed polystyrene-*block*-poly(acrylic acid). These long forms are typically abbreviated to the form: PS_{200}-*b*-PAA_{20} with subscripts denoting either the number of repeat units, or M_n. Block copolymers comprised of 2, 3, 4, *etc*… blocks are known as di-,tri-,tetrablocks, *etc.* copolymers respectively, irrespective of the orientation of the various blocks. Polymers comprised of these blocks can be created such that they are hydrophobic, hydrophilic or amphiphilic.[37] The solubility of these blocks relative to one another enable control over how these polymers will behave in solution, providing a handle for self-assembly. This control manifests itself as a complex interplay between enthalpic and entropic contributions between polymer-polymer and polymer-solvent interactions. Beginning from the Gibb's free energy (ΔG) (Eq. 1.4):

$$\Delta \mathrm{G} = \Delta \mathrm{H} - T\Delta \mathrm{S} \tag{1.4}$$

where ΔH is the change in enthalphy, T is temperature and ΔS is the change in entropy. Systems will tend to minimize the free energy, the implication being that favourable polymer/polymer and polymer/solvent interactions will lead to a negative ΔG. To display how the entropic and enthalpic components behave, the scenario of micelle formation of

an amphiphilic block copolymer will be presented: in organic solvents, the hydrophilic block will preferentially assemble to form the hydrophilic core of the micelle (this is a reverse micelle) whereas in aqueous media the inverse will occur (this is a regular micelle). Upon forming the micellar core an entropic penalty is imposed due to formation of a core/corona interface (loss of single chain flexibility) as well as chain stretching of the core forming blocks, additionally an enthalpic penalty is occurred from coronal chain repulsion. Counter to the conformational entropic and enthalpic penalties is a decrease in overall enthalpy resulting from the minimization of unfavourable polymer-solvent interactions and promotion of favourable polymer-polymer interactions through core formation. This enthalpic contribution is the primary driving force for micelle formation in organic solvents.[38,39]

In addition to the parameters above, certain additional aspects become important for micellar assembly when one (or both) block contains a charged repeat unit, *e.g.* PS-*b*-PAA.[37] In the case of PS-*b*-PAA, the difference in the electrostatic interactions between the ionic PAA block and the hydrophobic PS block enables the formation of micelles through phase separation upon addition of methanolic cadmium acetate dihydrate. It is this phase separation that drives the majority of the work presented within this thesis. Isolation of the cadmium salt within the hydrophilic core of the micelles the environment is primed for cadmium-based quantum dot formation. An example of this process is provided in Scheme 1 and is representative of the initial synthetic steps found in both Chapters 2 and 3 in addition to serving as a platform for future investigation. Note that while Scheme 1 indicates two chains being bound through the Cd^{2+} ion it is equally likely that other repeat units along the same chain may bind together in this manner.

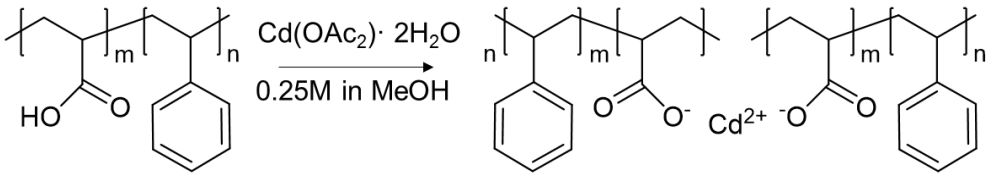

Scheme 1.1. Synthetic process for the formation of PS-b-PAA reverse micelles with cadmium acetate.

1.3 Gold Nanoparticles and Quantum Dots

Nanoparticles have seen a dramatic increase in research over the last several decades as a result of their wide array of physical properties which bridge between the molecular and the bulk. Nanoparticles are broadly defined as any particles with at least one dimension between approximately 1-100 nm, with special attention often given to the 1-10 nm range.[40] Note that as a general rule, individual molecules are not typically referred to as nanoparticles. The size of these nanoparticles is however incredibly important as within these size ranges particles begin to experience dramatic size-dependent properties, *e.g.* changes in electronic structure (see Figure 1-4), colour shifts, generation/loss of magnetism, etc.[41,42]

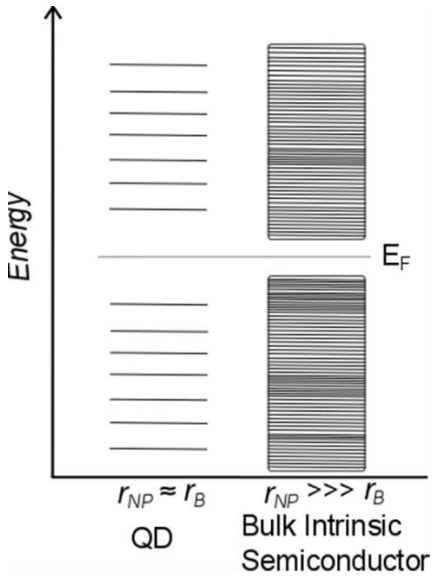

Figure 1-4. Example Jablonski diagram demonstrating the difference between a quantum dot (L) and a bulk intrinsic semiconductor (R).

The size dependent nature of these particles is a result of two key factors: significantly increased surface-to-volume ratio, and the alteration of the materials' electronic structure relative to their bulk counterparts, *e.g.* size reduction implies fewer atoms within the core and correspondingly fewer electronic states. In general the surface-to-volume ratio differential gives rise to the deviation of physical properties exhibited between bulk and nanoscale particles.[41,43,44]

In the bulk state there are metallic, semi-conducting and insulating materials. The difference between these materials is most easily represented through their electronic band structures: metallic materials have overlapped valence and conduction bands, semiconductors have a small energy difference between the valence and conduction bands, while insulators have large energy difference between the bands. When two identical atoms (*e.g.* Si) form a bond, the atomic orbitals must become molecular orbitals as a result of the Pauli Exclusion Principle (no two electrons can have the same quantum numbers in a

molecule). Therefore, upon formation of this molecule the atomic orbitals split into molecular orbitals of different energy, the electrons are then able to occupy these different levels without having the same energy. This concept is extended to large numbers of atoms, *e.g.* the formation of a crystal lattice, as the number of atomic orbitals increases, so too does the number of molecular orbitals until such a time as the energy difference between orbitals is so close together that they become a continuum, or band. Band gaps are ranges of energy that is not covered by any band. Between the bulk and atomic scales, a special type of nanoparticle exists, the quantum dot (QD). These semiconducting particles are typically between 1-10 nm in diameter, with electronic properties closely tied to particle size. The size dependence arises because there are so few atoms comprising the molecule, that the bands we observe in the bulk are now comprised of discrete energy levels.

When a semiconductor is exposed to a photon of sufficient energy, an electron can absorb this energy and be promoted to higher energy levels. The promotion of an electron results in a positively charged vacancy left behind by the electron, known as a "hole". The pairing of the electron and its corresponding hole form a particle referred to as an exciton, the size of which is characterized by the Bohr exciton radius (r_B). This phenomenon is visible both in the bulk and in quantum dots, key to QDs however is that when the size of the particle (r_{NP}) approaches r_B the material exhibits the quantum confinement effect.

The relationship between particle size and the band gap energy are described by Brus based on a three dimensional variant of the particle-in-a-box model.[45] This model establishes a "box" of infinitely high energy that is the size and shape of the nanoparticle, the electron in question is confined within this box and the energy required to promote this electron (forming an exciton) can be determined by equation 1.5.

$$E^* = E_g + \frac{\hbar^2\pi^2}{2R^2} * \left[\frac{1}{m_e} + \frac{1}{m_h}\right] - \frac{1.8e^2}{\epsilon R} + \ldots \quad (1.5)$$

E^* corresponds to the energy of the resulting exciton, E_g to the bulk band gap energy, R to the particle radius, m_e and m_h to the effective excited masses of the electron and hole respectively (note these are material dependent), e to the electron charge, and ϵ to permittivity. The size dependence of these systems can be visualized in the second and third terms on the right side of equation 1.5. While the third term shows a decrease in energy relative to R (negative), this term only scales linearly, whereas the second scales exponentially with R (positive). These two terms correspond to the *bound exciton energy* and *positive confinement* respectively. It becomes clear then that the increase in observed energy for QDs is more heavily dependent on the size confinement of the particle rather than the Coulombic attraction within the exciton.

Quantum dot systems exhibit what is commonly known as *band-edge* emission, this term is in reference to the process of emissive recombination of the exciton's electron and hole at approximately the same energy as the band gap energy. A slight Stokes-shift[46] (Figure 1-5) of the emitted photons from the band edge are common, resulting from non-radiative energy loss, *e.g.* heat. Many quantum dot systems will also exhibit another optical process known as *trapped-state* emission. This phenomenon is similar in concept to the process of Stokes shifting in small molecules in that non-

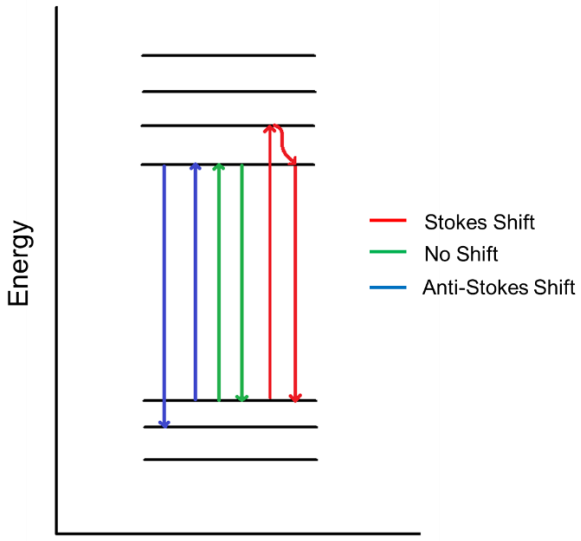

Figure 1-5. Simple Jablonski diagram demonstrating Stokes and anti-Stokes fluorescence shifts.

radiative energy loss (*e.g.* heat) results in a red-shift in the emission wavelength, note that while Anti-Stokes shifts are presented here they are rather uncommon outside of Raman spectroscopy and photon up-converting materials. The difference between the two processes arises from the presence of defects in the lattice or on the surface of the quantum dots, e.g. impurities, vacancies, dangling bonds, etc.[43] These defects will trap the charge carriers until they undergo recombination, hence the term trapped-state emission in cases where a photon is produced. Depending on the nature of these defect sites, their corresponding energy levels may fall within the band gap of the semi-conducting material (Figure 1-6).[43,47] As such, in a system containing trapped states it is possible for excited electrons to undergo some non-radiative relaxation to these trapped states and subsequently release considerably red-shifted photons once they relax to ground and recombine with their holes. Conversely the trapped states may be located at the bottom of the band gap resulting in a similar red shift. Trapped state emission is inherently a broader profile than

band-edge emission as a result of the wide variety of possible energy levels generated from defect sites. It should be noted that with decreasing quantum dot size, the influence of surface trapped states on the overall emission profile becomes more prominent as a result of the increasing surface area to volume ratio. Control over the formation of trapped states is a critical component of QD formation, whether it be for the promotion[48] or prevention of their formation.[49,50] A common methodology for the reduction or elimination of trapped state emission is called surface passivation, which typically entails either the formation of a core/shell complex or special selection of surfactants.[43,44,47] In both cases the concept behind the process is to either remove the trapped states, or create trapped states that are higher/lower such that they don't occupy the band gap. In core/shell materials this is typically achieved through the formation of a shell with a larger band gap than the core material and is able to match the crystal lattice structure of the core. These prevent both chemical defects between the surface and the environment as well as introduction of lattice defects during shell formation.

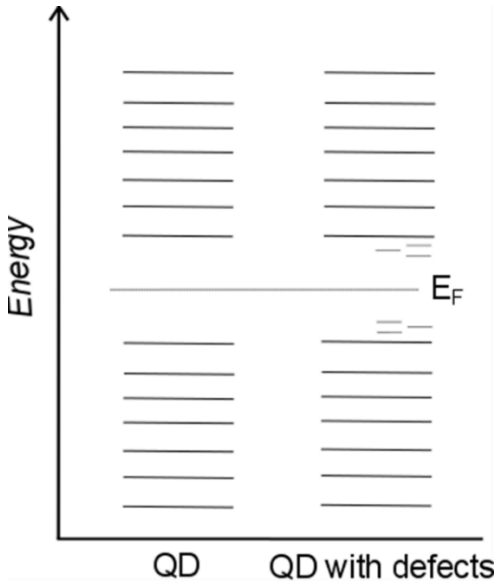

Figure 1-6. Jablonski diagram showing the difference in electronic configuration as a result of defect sites in QDs.

Following along with the interesting physical properties demonstrated by quantum dots above, nanoparticles exhibit another immensely interesting physical process: localized surface plasmon resonance (LSPR).[51,52] A plasmon is a coherent, delocalized oscillation of electrons at an interface, *e.g.* between the surface of a nanoparticle and the surrounding environment. Upon exposure to a size-dependent critical wavelength of incident light, the electrons on the surface of the nanoparticle will become excited. This excitation effectively serves to polarize the electron cloud to one side of the nanoparticle. Subsequently the particle experiences a restoring force to rebalance this charge across the material, resonance occurs when the wavelength of excited light is sufficient to continue this oscillation of polarization. The wavelength at which resonance occurs will depend on the size of the nanoparticle due to confinement of the surface plasmon to the particle, *e.g.* if the particle is smaller, the plasmon is confined to a smaller area and a correspondingly shorter wavelength of light is required to form the plasmon. In anisotropic samples (*e.g.* rods) there

will be a surface plasmon which corresponds to each axis, e.g. longitudinal and transverse.[52]

Under specific conditions, quantum dots are able to interact with the enhanced electric field arising from surface plasmons on neighboring particles. These hybrid structures have attracted attention for applications such as imaging probes,[53,54] sensors[55,56] and photcatalysts.[57] As indicated above the spacing between these two components will be critical for their interaction, and as such many different techniques have been explored for use as spacing materials from DNA,[20,31] polypeptides,[32] silica shells,[58,59] and synthetic polymers.[60,61] These various methods all serve to form a spacer of tunable, either through experimental conditions (*e.g.* temperature) or adjustment on synthetic parameters. Amongst all the methods, it was determined that in the cases where the gold nanoparticles were too close to the QD fluorophore emission quenching was observed, typically as a result of energy transfer from the QD to the AuNP becomes the dominant process which subsequently results in non-radiative energy loss. Above this distance, amplification of the emission signal from the QD was observed. This was a result of several different influences, specifically, the modification of the electric field near the QD, damping of energy transfer from the QD to the AuNP, in some cases through increase in the polarizing effects of the metal NPs.[58] The emission amplification phenomenon was observed to be optimal in the range of ~10 nm across these studies, and decreasing as the particles move further away or closer together. To this end, using a tunable spacer one can imagine that targeting this ~10 nm spacing distance is highly desirable for sensing purposes, *e.g.* a polymer spacer will be sensitive to both chemical environment and temperature, expanding or contracting to suit, effectively altering the distance between cores.

1.4. Primary Characterization Techniques

A series of techniques were employed throughout the synthetic process of the quantum dot micelles (QDM) for characterization purposes. The primary techniques employed were: Photoluminescence spectroscopy (PL), dynamic and static light scattering (DLS and SLS), absorbance measurements, and transmission electron microscopy (TEM). These various techniques were used to determine the size of the optical properties of the assemblies and their sizes in solution, with size analysis confirmation performed with TEM.

1.4.1. Photoluminescence Spectroscopy

Photoluminescence spectroscopy is a characterization method by which optical properties of a fluorophore can be determined, *e.g.* band gap size, emission wavelength, quantum yield, etc. All the various measurements operate around the same process, illumination of a sample with a source lamp/laser followed by the collection of emitted light as a function of wavelength and/or time. The energy of the band gap can be determined through the collection of an "excitation" measurement. An excitation measurement is performed by forcing the detector to scan at a specific wavelength, typically close to the wavelength of maximum emission (λ_{max}) and exciting the sample across a range of wavelengths. As the instrument scans from long wavelengths to short (low energy to high) the excitation profile will remain flat and low until such a time that there is sufficient energy to cross the band gap. At this time, a peak will be observed corresponding to an increase in emitted light as a result of the sample absorbing the excitation light. In a perfect, monodisperse sample free of surface defects this transition will be a vertical transition at the exact wavelength that corresponds to the energy of the band gap. In practical samples with polydisperse particles this will be a more gradual

increase. In tandem with excitation measurements, “emission” measurements can be collected under virtually identical sample parameters. This measurement monitors how the sample’s emission profile varies as a function of excitation wavelength. By exciting at one wavelength then monitoring the emitted light across a wide range of wavelengths, and repeating with several excitation wavelengths it is possible to provide a map of the emission profile for the entirety of a solution. In the case of sample with multiple species (*e.g.* QDs with gold nanoparticles) it is possible to determine if there is any influence from one particle on the other provided acceptable backgrounds have been collected. Quantum yield measurements are simply a measurement of the number of emitted photons divided by the number of absorbed photons.

It should be noted that there is another common photoluminescence technique used to study emissive samples known as a lifetime measurement. This technique monitors the amount of time it takes for a photoluminescent material to return to the ground state following excitation by incident light through monitoring of the intensity of emitted light. From this test, various physical properties may be determined such as the half-life of the excitation state, or the pathway by which de-excitation occurs (*e.g.* to what extent is there non-radiative energy loss). To this end, work by a colleague on the AuNP-CdS system has indicated that there is no observable influence of gold nanoparticles on the CdS de-excitation pathway.[27]

1.4.2. Dynamic Light Scattering

Dynamic light scattering (DLS) is a method by which the hydrodynamic diameter (d_h), the effective diameter of a solute in solution, of a colloidal particle can be determined.

The basic process behind this characterization technique is that smaller particles will move more quickly through the solution than larger particles as dictated by Brownian motion. In order to obtain quantitative data from this, the DLS characterization method utilizes a series of fits to an autocorrelation function, a process which will be subsequently described. The normalized time autocorrelation function is generated by the computational correlation of the time-dependent (for a given delay time,τ) fluctuations in the scattering intensity of a given sample, Eq. 1.6.

$$g^{(2)}(\tau) = \frac{< I(t)I(\tau + t) >}{< I(t) >^2} \tag{1.6}$$

Where $I(t)$ is the intensity of scattered light at time t, the braces denote averaging over all t, and τ is the delay time. This delay time refers to the amount of time between the collection of a duplicate intensity trace and the original before the averaging of their intensities is performed. In most cases, the intensity-intensity time autocorrelation function $g^{(2)}(\tau)$ can be expressed in terms of the field-field time autocorrelation function $g^{(1)}(\tau)$, as follows:

$$g^{(2)}(\tau) = B + \beta[g^{(1)}(\tau)]^2 \tag{1.7}$$

where B is a constant typically called the "baseline" and represents the autocorrelation function at infinite delay times, β is a factor which relies on experimental geometry, $g^{(1)}(\tau)$ is given by:

$$g^{(1)}(\tau) = \frac{<E(t)E^*(\tau+t)>}{<E(t)E^*(t)>} \tag{1.8}$$

where $E(t)$ and $E(t + \tau)$ correspond the the scattered electric fields at times t and $t + \tau$ respectively.In the case of monodisperse, non-interacting particles in solution, their diffusion can be modeled by an exponential decay of the normalized electric field autocorrelation function, $g_1(\tau)$:

$$g^{(1)}(\tau) = \exp(-\Gamma\tau) \tag{1.9}$$

where Γ is the relaxation rate, and τ is the delay time. From this equation, relaxation rate is related to the particle translational diffusion coefficient (D_t) through the relationship:

$$\Gamma = D_t q^2 \tag{1.10}$$

q represents the scattering vector, defined as:

$$q = \left(\frac{4\pi n}{\lambda}\right) \sin\left(\frac{\theta}{2}\right) \tag{1.11}$$

where n is the refractive index of the solvent, λ is the wavelength of incident light and θ is the angle at which the scattered light is measured.

The two primary mathematical models used to fit the autocorrelation function for determination of a sample's hydrodynamic diameter are known as cumulant analysis and CONTIN analysis. Cumulant analysis is able to provide a single average value of d_h with the variance and asymmetry of the sample distribution, however it is unable to accurately represent samples with non-monomodal distributions. CONTIN analysis on the other hand is able to model these non-monomodal distributions through calculating a multiple exponential fit to the correlation function, providing the distribution of particles within the sample. These fits provide Γ which in turn can be used to calculate D_t (equation 1.10), this value is then related to the r_h through the Stokes-Einstein equation:

$$D_t = \frac{k_B T}{8\pi\eta r_h^3} \tag{1.12}$$

Where k_B is the Boltzmann constant, T is temperature, r_h is the hydrodynamic radius and η is the dynamic solvent viscosity. Note, for polydisperse samples, $g^{(1)}(\tau)$ can't be described by a single exponential decay, rather it must be represented as an integral over a distribution of decay rates, $G(\Gamma)$, described by the following equation:

$$g^{(1)}(\tau) = \int_0^\infty G(\Gamma)\exp(-\Gamma\tau)\,d\Gamma \tag{1.13}$$

where $G(\Gamma)$ is normalized such that its integral from 0 to ∞ with respect to Γ is equal to 1.

1.4.3. Static Light Scattering

Structural information can be elucidated through scattering measurements collected at multiple angles as different shapes will scatter incident light in different manners. Static light scattering (SLS) is a method by which scattering intensity of a given sample can be monitored across a range of angles.[35] This technique has multiple purposes, of primary importance for this work is the determination of M_w, the radius of gyration (R_g, the average distance from the center of gravity to the chain ends of a polymer in solution) and the second-virial coefficient (A_2, a thermodynamic parameter that describes the attractive and repulsive forces between polymers/particles in solution, it is sensitive to the solvent in question and the temperature) through the generation of Zimm plot. This is possible through fits to the Zimm equation (Eq. 1.14).

$$\frac{Kc}{R_\theta} = \frac{1}{M_w P(\theta)} + 2A_2 c \tag{1.14}$$

Where

$$K = \frac{4\pi^2 n_0^2 (\frac{dn}{dc})^2}{N_A \lambda^4} \tag{1.15}$$

and c corresponds to solution concentration, q to the scattering vector (see eq. 1.11), R_θ is the Rayleigh ratio which itself is derived from $R_\theta = i_\theta r^2/I_0$ (I_0 is the intensity of incident light, i_θ is the scattered light per unit volume at angle θ, r is the distance from the sample to the detector), dn/dc is the differential refractive index, N_A is Avogadaro's Number, M_w is the

weight average molecular weight. $P(\theta)$ is an angle dependent term known as the form factor and describes the attenuation of scattered light intensity due to interparticle interference, it is inherently dependent on particle size and shape and at small scattering angles (the Guinier regime) takes the form:

$$P(\theta) = \left[1 + \frac{16\pi^2 r_g^2}{3\lambda^2} sin^2(\frac{\theta}{2})\right] \quad (1.17)$$

By extrapolation to zero concentration (infinite dilution) and zero angle on a plot of K/R_θ vs. $\sin^2(\theta/2) + kc$ where k is a plotting constant, the various terms mentioned above can be determined.

When paired with the r_h data from DLS, further information on the nature of the particles in solution can be elucidated. For example, the combination of empirical and theoretical values indicate that ratios of R_g/r_h can indicate hard spheres (~0.775), star-like structure (~1.1) and rod-like polymer chains under strong segregation (~1.5).[62,63]

1.4.4. Transmission Electron Microscopy (TEM)

Transmission electron microscopy is similar in concept to traditional optical microscopy, the advantage lies in the use of an electron beam for illumination. The advantage imparted by the use of electrons lies in their considerably smaller de Broglie wavelength relative to that of visible light. As a result, considerably higher resolution and magnification can be achieved as made clear from equation 1.18:

$$d = \frac{\lambda}{2nsin(\alpha)} \quad (1.18)$$

Where d is the maximum resolution, λ is the wavelength of light/electron, n is the refractive index of the medium and α is the maximum half-angle of the cone of light capable of entering the lens assembly (this is related to numerical aperture NA).[64] The electron beam

is generated from a LaB_6 electron "gun" at the top of an evacuated column. This beam is then passed through a series of lenses and focused onto the sample stage. A camera (or phosphorescent screen) is placed below the sample stage. If a sufficiently dense material is along the electron beams' path, scattering will occur, otherwise the beam will pass unhindered into the camera/screen. Where the electron beam was scattered a dark spot will be observed on the screen/camera, effectively forming an image of the sample in question. The darker the resulting parts of the image are, the more dense or thick the area of the sample.

1.4.5. Absorbance spectroscopy

Absorbance measurements are a powerful, yet simple method of sample characterization. A sample is placed within the beam path of a white light source. This white light source is often composed of two bulbs, one which is able to explore from UV to visible light and one that can extend from visible light to the near IR. The exact set up for a given instrument can vary drastically. The general principle of this process is to have the light source scan across the desired range of wavelengths, e.g. 300-1000 nm for this research project. During this scan a detector is located on the opposite side of the sample from the light source and monitors the amount of light that passes through the sample. The instrument then compares the amount of incident light to the amount of transmitted light. The difference between these two values is referred to as the *transmittance* of the material. This relates to the absorbance through the equation 1.19:[65]

$$A = log_{10}\left(\frac{\Phi_e^i}{\Phi_e^t}\right) = -log_{10}T \qquad (1.19)$$

Where A is absorbance, T is transmittance, Φ_e^i and Φ_e^t correspond to the incident radiant flux and the transmitted radiant flux respectively. From absorbance measurements various

parameters can be determined (with careful experimental set-up) from the Beer-Lambert Law:

$$A = \varepsilon l c \tag{1.20}$$

Where ε is the molar absorptivity, l is the path length of the light through the material and c is the concentration of the sample. The use of absorbance spectroscopy for quantum dot size characterization is detailed future chapters. Note that what is measured in solutions which exhibit scattering is better reflected by the "extinction" of the sample, which is the sum of absorbance and scattering processes on the observed absorbance of the sample.

1.5. Content of the Thesis

This thesis seeks to detail the methodologies by which specialized RAFT block copolymers can direct the synthesis and self-assembly of inorganic nanoparticles. The formation of these materials seeks to show the general applicability of these systems as building blocks for self-assembly. Additionally the methodology by which these assemblies can be carefully characterized, the pitfalls that are associated with their synthesis, as well as commentary into their possible applications are to be established.

Chapter two will seek to demonstrate the broad applicability of the RAFT PS-*b*-PAA tetrablock copolymers as a reactor for cadmium based quantum dots through the formation of CdSe QDs. Additionally this chapter will provide detailed analysis on the solvent compatibility of the RAFT copolymer in a series of solvents and the impact of these solvents on the assembly process of the CdSe QDs.

Chapter three will build upon past research into the assembly of CdS QDs with gold nanoparticles as a means to investigate emission amplification. Namely this will demonstrate that the technique functions with different RAFT copolymer block lengths.

Subsequently chapter 3 will describe preliminary investigations into secondary self-assembly of the QD-AuNP systems into large compound micelles.

Finally, the fourth chapter will bring together the two experimental chapters, detailing the conclusions that can be drawn from this research and propose where these projects may lead in the future.

(1) Whitesides, G. M. *Science (80-.).* **2002**, *295* (5564), 2418.

(2) Kirley, M. P.; Aloui, T.; Glass, J. T.; Kirley, M. P.; Aloui, T.; Glass, J. T. *Appl. Phys. Lett.* **2017**, *233109*.

(3) Hakonen, A.; Svedendahl, M.; Ogier, R.; Yang, Z.-J.; Lodewijks, K.; Verre, R.; Shegai, T.; Andersson, P. O.; Käll, M. *Nanoscale* **2015**, No. April, 9405.

(4) Peksa, V.; Lebrušková, P.; Šípová, H.; Štěpánek, J.; Bok, J.; Homola, J.; Procházka, M. *Phys. Chem. Chem. Phys.* **2016**, No. 29, 19613.

(5) Du, G. X.; Mori, T.; Suzuki, M.; Saito, S.; Fukuda, H.; Takahashi, M. *Appl. Phys. Lett.* **2010**, *96* (8).

(6) Wu, L. Y.; Di Carlo, D.; Lee, L. P. *Biomed. Microdevices* **2008**, *10* (2), 197.

(7) Bains, A.; Cao, Y.; Kly, S.; Wulff, J. E.; Moffitt, M. G. *Mol. Pharm.* **2017**, acs. molpharmaceut.7b00177.

(8) Wang, C.-W.; Sinton, D.; Moffitt, M. G. *J. Am. Chem. Soc.* **2011**, *133* (46), 18853.

(9) Zeng, H.; Li, J.; Liu, J. P.; Wang, Z. L.; Sun, S. *Nature* **2002**, *420* (6914), 395.

(10) Lan, X.; Wang, Q. *Adv. Mater.* **2016**, 10499.

(11) Zheng, J.; Dai, B.; Liu, J.; Liu, J.; Ji, muwei; Liu, J.; Zhou, Y.; Xu, M.; Zhang, J.

ACS Appl. Mater. Interfaces **2016**, *8* (51), 35426.

(12) Abécassis, B. *ChemPhysChem* **2016**, *17* (5), 618.

(13) Moffitt, M. G. *J. Phys. Chem. Lett.* **2013**, *4*, 3654.

(14) Corbierre, M. K.; Cameron, N. S.; Lennox, R. B. *Langmuir* **2004**, *20* (7), 2867.

(15) Balazs, A. C.; Emrick, T.; Russell, T. P. *Science (80-.).* **2006**, *314* (5802), 1107.

(16) Kim, J. U.; Matsen, M. W. *Phys. Rev. Lett.* **2009**, *102* (7).

(17) Du, J.; O'Reilly, R. K. *Chem. Soc. Rev.* **2011**, *40* (5), 2402.

(18) Staff, R. H.; Gallei, M.; Mazurowski, M.; Rehahn, M.; Berger, R.; Landfester, K.; Crespy, D. *ACS Nano* **2012**, *6* (10), 9042.

(19) Oh, E.; Hong, M. Y.; Lee, D.; Nam, S. H.; Yoon, H. C.; Kim, H. S. *J. Am. Chem. Soc.* **2005**, *127* (10), 3270.

(20) Li, M.; Cushing, S. K.; Wang, Q.; Shi, X.; Hornak, L. A.; Hong, Z.; Wu, N. *J. Phys. Chem. Lett.* **2011**, *2* (17), 2125.

(21) Susumu, K.; Oh, E.; Delehanty, J. B.; Blanco-Canosa, J. B.; Johnson, B. J.; Jain, V.; Hervey, W. J.; Algar, W. R.; Boeneman, K.; Dawson, P. E.; Medintz, I. L. *J. Am. Chem. Soc.* **2011**, *133* (24), 9480.

(22) Shi, Y.; Pan, Y.; Zhang, H.; Zhang, Z.; Li, M. J.; Yi, C.; Yang, M. *Biosens. Bioelectron.* **2014**, *56*, 39.

(23) Huang, D.; Niu, C.; Wang, X.; Lv, X.; Zeng, G. *Anal. Chem.* **2013**, *85* (2), 1164.

(24) Wang, X.; Guo, X. *Analyst* **2009**, *134* (7), 1348.

(25) Yusuf, H.; Kim, W.; Lee, D. H.; Aloshyna, M.; Brolo, A. G.; Moffitt, M. G. *Langmuir* **2007**, *23* (10), 5251.

(26) Yusuf, H.; Kim, W.-G.; Lee, D. H.; Guo, Y.; Moffitt, M. G. *Langmuir* **2007**, *23* (2), 868.

(27) Ribeiro, T.; Prazeres, T. J. V; Moffitt, M.; Farinha, J. P. S. *J. Phys. Chem. C* **2013**, *117*, 3122.

(28) Kulakovich, O.; Strekal, N.; Yaroshevich, A.; Maskevich, S.; Gaponenko, S.; Nabiev, I.; Woggon, U.; Artemyev, M. *Nano Lett.* **2002**, *2* (12), 1449.

(29) Nie, Z.; Petukhova, A.; Kumacheva, E. *Nat. Nanotechnol.* **2010**, *5* (1), 15.

(30) Li, M.; Cushing, S. K.; Wang, Q.; Shi, X.; Hornak, L. A.; Hong, Z.; Wu, N. *J. Phys. Chem. Lett.* **2011**, *2* (17), 2125.

(31) Gueroui, Z.; Libchaber, A. *Phys. Rev. Lett.* **2004**, *93* (16), 1.

(32) Pons, T.; Medintz, I. L.; Sapsford, K. E.; Higashiya, S.; Grimes, A. F.; English, D. S.; Mattoussi, H. *Nano Lett.* **2007**, *7* (10), 3157.

(33) Sperling, L. H. *Introduction to Physical Polymer Science*; John Wiley & Sons, Inc.: New York, 2005.

(34) Keddie, D. J. *Chem. Soc. Rev.* **2014**, *43* (2), 496.

(35) Cowie, J. M. G.; Arrighi, V. *Polymers: Chemistry & Physics of Modern Materials*, 3rd ed.; CRC Press: New York, 2007.

(36) Moad, G.; Rizzardo, E.; Thang, S. H. *Modern Polymerization Techniques*; Sigma-

Aldrich Corporation, 2010; Vol. 5.

(37) Mai, Y.; Eisenberg, A. *Chem. Soc. Rev.* **2012**, *41* (18), 5969.

(38) Hamley, I. W. *The Physics of Block Copolymers*; Oxford University Press: New York, 1998.

(39) Hadjichristidis, N.; Pispas, S.; Floudas, G. *Block Copolymers: Synthetic Strategies, Physical Properties, and Applications*; John Wiley & Sons, Inc.: Hoboken, New Jersey, 2003.

(40) Alemán, J. V.; Chadwick, A. V.; He, J.; Hess, M.; Horie, K.; Jones, R. G.; Kratochvíl, P.; Meisel, I.; Mita, I.; Moad, G.; Penczek, S.; Stepto, R. F. T. *Pure Appl. Chem.* **2007**, *79* (10), 1801.

(41) Roduner, E. *Chem. Soc. Rev.* **2006**, *35* (7), 583.

(42) Watkins, S. E.; Jasieniak, J.; Califano, M. *ACS Nano* **2011**, *5* (7), 5888.

(43) Veamatahau, A.; Jiang, B.; Seifert, T.; Makuta, S.; Latham, K.; Kanehara, M.; Teranishi, T.; Tachibana, Y. *Phys. Chem. Chem. Phys.* **2015**, *17* (4), 2850.

(44) Clark, P. C. J.; Radtke, H.; Pengpad, A.; Williamson, A. I.; Spencer, B. F.; Hardman, J. O.; Leontiadou, M. A.; Neo, D. C. J.; Fairclough, S. M.; Watt, A. A. R.; Pis, I.; Nappini, S.; Bondino, F.; Magnano, E.; Schulte, K.; Silly, M.; Sirotti, F.; Flavell, W. R. *Nanoscale* **2017**, *9*, 6056.

(45) Brus, L. *J. Phys. Chem.* **1986**, *90* (12), 2555.

(46) Lakowicz, J. R. *Principles of Fluorescence Spectroscopy Principles of Fluorescence Spectroscopy*; 2006.

(47) Arora, V.; Soni, U.; Mittal, M.; Yadav, S.; Sapra, S. *J. Colloid Interface Sci.* **2017**, *491*, 329.

(48) Ye, Y.; Wang, X.; Ye, S.; Xu, Y.; Feng, Z.; Li, C. *J. Phys. Chem. C* **2017**, *121* (32), 17112.

(49) Mattoussi, H.; Radzilowski, L. H.; Dabbousi, B. O.; Fogg, D. E.; Schrock, R. R.; Thomas, E. L.; Rubner, M. F.; Bawendi, M. G. *J. Appl. Phys.* **1999**, *86* (2001), 4390.

(50) Wang, C.-W.; Moffitt, M. G. *Langmuir* **2004**, *20* (26), 11784.

(51) Luther, J. M.; Jain, P. K.; Ewers, T.; Alivisatos, A. P. *Nat Mater* **2011**, *10* (5), 361.

(52) Noguez, C. *J Phys Chem C* **2007**, 3806.

(53) Jin, Y.; Gao, X. *Nat. Nanotechnol.* **2009**, *4* (9), 571.

(54) Quach, A. D.; Crivat, G.; Tarr, M. A.; Rosenzweig, Z. *J. Am. Chem. Soc.* **2011**, *133* (7), 2028.

(55) Lee, J.; Govorov, A. O.; Kotov, N. A. *Angew. Chemie - Int. Ed.* **2005**, *44* (45), 7439.

(56) Zeng, Q.; Zhang, Y.; Liu, X.; Tu, L.; Kong, X.; Zhang, H. *Chem. Commun.* **2012**, *48* (12), 1781.

(57) Zhang, N.; Liu, S.; Xu, Y.-J. *Nanoscale* **2012**, *4*, 2227.

(58) Fedutik, Y.; Temnov, V.; Woggon, U.; Ustinovich, E.; Artemyev, M. *J. Am. Chem. Soc.* **2007**, *129* (48), 14939.

(59) Liu, N.; Prall, B. S.; Klimov, V. I. *J. Am. Chem. Soc.* **2006**, *128* (48), 15362.

(60) Chen, C. W.; Wang, C. H.; Wei, C. M.; Chen, Y. F. *Appl. Phys. Lett.* **2009**, *94* (7), 10.

(61) Lee, J.; Govorov, A. O.; Kotov, N. a. *Angew. Chemie - Int. Ed.* **2005**, *44* (45), 7439.

(62) Moffitt, M.; Eisenberg, A. *Macromolecules* **1997**, *30* (15), 4363.

(63) Foerster, S.; Zisenis, M.; Wenz, E.; Antonietti, M. *J. Chem. Phys.* **1996**, *104* (24), 9956.

(64) Murphy, D. B.; Davidson, M. W. *Fundamentals of Light Microscopy and Electronic Imaging*, 2nd ed.; Wiley-Blackwell, 2012.

(65) IUPAC. *Compendium of Chemical Terminology*, 2nd ed.; IUPAC, 1996.

(66) Gazit, O.; Khalfin, R.; Cohen, Y.; Tannenbaum, R.; Gazit, O.; Khalfin, R.; Cohen, Y.; Tannenbaum, R. *J. phys chem C* **2009**, 576.

(67) Cerdán, L.; Costela, A.; Enciso, E.; García-Moreno, I. *Adv. Funct. Mater.* **2013**, *23*, 3916.

(68) Toor, A.; Feng, T.; Russell, T. P. *Eur. Phys. J. E* **2016**, *39* (5).

(69) Thiermann, R.; Bleul, R.; Maskos, M. *Macromol. Chem. Phys.* **2017**, *218* (2), 1600347.

(70) Klok, H. A.; Lecommandoux, S. *Adv. Mater.* **2001**, *13* (16), 1217.

(71) Armao, J. J.; Nyrkova, I.; Fuks, G.; Osypenko, A.; Maaloum, M.; Moulin, E.;

Arenal, R.; Gavat, O.; Semenov, A. N.; Giuseppone, N. *J. Am. Chem. Soc.* **2017**, jacs. 6b11179.

(72) Liang, R.; Xu, J.; Li, W.; Liao, Y.; Wang, K.; You, J.; Zhu, J.; Jiang, W. *Macromolecules* **2015**, *48* (1), 256.

(73) Kim, S. H.; Misner, M. J.; Xu, T.; Kimura, M.; Russell, T. P. *Adv. Mater. (Weinheim, Ger.* **2004**, *16* (3), 226.

(74) Xu, Z.; Xue, P.; Gao, Y. E.; Liu, S.; Shi, X.; Hou, M.; Kang, Y. *J. Colloid Interface Sci.* **2017**, *490*, 511.

(75) Yu, H. *Prog. Polym. Sci.* **2014**, *39* (4), 781.

(76) Nepal, D.; Drummy, L. F.; Biswas, S.; Park, K.; Vaia, R. a. *ACS Nano* **2013**, *7* (10), 9064.

(77) Cui, Q.; He, F.; Li, L.; Möhwald, H. *Adv. Colloid Interface Sci.* **2014**, *207* (1), 164.

(78) Zhang, C.; Ding, C.; Zhou, G.; Xue, Q.; Xian, Y. *Anal. Chim. Acta* **2017**, *957*, 63.

(79) Sasidharan, A.; Monteiro-Riviere, N. A. *Wiley Interdiscip. Rev. Nanomedicine Nanobiotechnology* **2015**, *7* (6), 779.

(80) Pelaz, B.; Charron, G.; Pfeiffer, C.; Zhao, Y.; de la Fuente, J. M.; Liang, X.-J.; Parak, W. J.; Del Pino, P. *Small* **2013**, *9* (9–10), 1573.

(81) Khullar, P.; Singh, V.; Mahal, A.; Kumar, H.; Kaur, G.; Bakshi, M. S. *J. Phys. Chem. B* **2013**, *117* (10), 3028.

(82) Krishnan, D.; Johnson, H. T. *J. Mech. Phys. Solids* **2014**, *62*, 48.

(83) Knaapila, M.; Monkman, A. P. *Adv. Mater.* **2013**, *25* (8), 1090.

(84) Brust, M.; Walker, M.; Bethell, D.; Schiffrin, D. J.; Whyman, R. *J. Chem. Soc., Chem. Commun.* **1994**, 801.

(85) Moffitt, M.; McMahon, L.; Pessel, V.; Eisenberg, a. *Chem. Mater.* **1995**, *7* (6), 1185.

(86) Ringler, M.; Schwemer, A.; Wunderlich, M.; Nichtl, A.; Kürzinger, K.; Klar, T. A.; Feldmann, J. *Phys. Rev. Lett.* **2008**, *100*, 203002.

(87) Hrelescu, C.; Sau, T. K.; Rogach, A. L.; Frank, J.; Laurent, G.; Douillard, L. *Nano Lett.* **2011**, *11*, 402.

Chapter 2 - A Versatile Tetrablock Copolymer Scaffold for Hierarchical Colloidal Nanoparticle Assemblies: Synthesis, Characterization, and Molecular Dynamics Simulations

Gema Marcelo[a #], Fraser Burns[b #], Tânia Ribeiro[a], J. M. G. Martinho[a], M. Pilar Tarazona[c], Enrique Saiz[c*], Matthew G. Moffitt[b*] and José Paulo S. Farinha[a*]

[a] Centro de Química-Física Molecular and IN-Institute for Nanoscience and Nanotechnology, Instituto Superior Técnico, University of Lisbon, 1049-001 Lisboa, Portugal. [b] Department of Chemistry, University of Victoria, P.O. Box 1700, Stn CSC, Victoria, BC, Canada V8W 3V6. [c] Departamento de Química Física, Universidad de Alcalá, 28871 Alcalá de Henares, Madrid, Spain

2.1. Keywords: block copolymers, polyelectrolytes, self-assembly, polymer micelles, cadmium selenide, quantum dots, thiol-functionalized, reversible addition fragmentation chain transfer (RAFT), size-exclusion chromatography-multi-angle light scattering (SEC-MALS), molecular dynamics.

Contributions: RAFT-CdAc and RAFT-CdSe synthesis and characterization was performed by Fraser Burns under the supervision of Matthew G. Moffitt. RAFT polymer synthesis and characterization and computational modelling was performed by Gema Marcelo, Tânia Ribeiro, J. M. G. Martinho, M. Pilar Tarazona, Enrique Saiz and José Paulo S. Farinha.

2.2. Abstract

A unique combination of molecular dynamics simulations and detailed multi-angle light scattering size exclusion chromatography (SEC-MALS) analysis is used to provide important *a priori* insights into the solution self-assembly of a well-defined and symmetric tetrablock copolymer with two acrylic acid outer blocks, two polystyrene inner blocks and a trithiocarbonate (TTC) central group, prepared by reversible addition-fragmentation chain transfer (RAFT) polymerization. SEC-MALS experiments show that the copolymer forms aggregates in both tetrahydrofuran (THF) and *N*-dimethylformamide (DMF), even in the presence of different salts, but not in 1,4-dioxane (dioxane). Combined with molecular dynamic simulations, these results indicate that the acrylic acid units are the main cause of aggregation through intermolecular hydrogen bonding, with additional stabilization by the central TTC. The block copolymer chains self-assemble in dioxane by adding cadmium acetate, originating flower-like inverse micelles with a cadmium acrylate core and the TTC groups in the outer surface of the PS corona. The micelles were used as nanoreactors in the templated synthesis of a single cadmium selenide quantum dot in the core of each micelle, while the shell TTC groups can be converted into thiol functions for further use of these units in hierarchical nanostructures. Only in dioxane where simulations and SEC-MALS suggest an absence of copolymer aggregates prior to cadmium acetate addition do well-dispersed and highly luminescent CdSe QDs form by templated synthesis. These results provide valuable insights into the self-assembly of RAFT copolymers in different solvent systems as it relates to the preparation of emissive QDs with polymer-spaced thiol functionality for binding to gold nanostructures.

2.3. Introduction

Block copolymers of precise architecture and chain length self-assemble into micelles of low size dispersity, which can be used as templates for the growth of metal or semiconductor nanostructures.[1-6] The resulting nanostructures can be used as building blocks in the preparation of hierarchical hybrid nanostructures through subsequent self-assembly mechanisms mediated by the surrounding polymer brushes[7-11] In particular, nanostructures consisting of a quantum dot (QD) core surrounded by a polymer brush layer terminated with thiol groups are potential building blocks for controlled assemblies of photoluminescent QDs and gold nanostructures with controlled distances mediated by the polymer chains.[12] Such composite nanostructures exhibiting controlled interactions

between QD emission and gold nanoparticle surface plasmons offer numerous applications as functional elements for sensing and photonics.[7,11-23]

To achieve fine control over nanoparticle size and spacing in hierarchical hybrid nanostructures, block copolymers with well-defined architectures, predetermined molecular weights, narrow molecular weight distributions, and predictable micellization behaviors in selective solvents, are required. Controlled radical polymerization (CRP) techniques[23,24] have become increasingly popular for the production of polymers with these properties, from a much larger variety of monomers and under simpler polymerization conditions than other controlled polymerization techniques, such as anionic polymerization. All the main CRP techniques, NMP (nitroxide mediated polymerization),[22] ATRP (atom transfer radical polymerization),[23,24] and RAFT (reversible addition-fragmentation chain transfer),[25] can be used to prepare amphiphilic copolymers. These have attracted much attention because of their versatile self-assembly behavior, which can be controlled by different factors, such as the absolute and relative block lengths, the presence of additives, temperature, and the nature and composition of the solvent. Asymmetric poly(styrene-*b*-acrylic acid) copolymers with different compositions have been used to prepare several supramolecular structures, such as rods, micelles, tubules, onions, spindles and vesicles.[33,34]

Our group has previously applied symmetric amphiphilic tetrablock copolymers of poly(acrylic acid-*b*-styrene-*b*-styrene-*b*-acrylic acid), with a central group of trithiocarbonate (TTC) between the two styrene blocks (PAA-PS-TTC-PS-PAA, Scheme

2.1) to prepare hierarchical quantum dot (QD)-gold nanoparticle assemblies with surface plasmon-enhanced fluorescence.[12] The tetrablock copolymers with central TTC groups were shown to be suitable building blocks for the self-assembly of complex supramolecular assemblies with ensemble properties governed by structural hierarchy. In that work, we induced self-assembly of the copolymer in Scheme 1 into flower-like reverse micelles by adding cadmium acetate. These structures, with a cadmium acrylate core and a polystyrene (PS) shell decorated with the TTC groups, were then used in the templated conversion of the entrapped Cd^{2+} ions to a single CdS QD in each micelle core. The TTC were converted to thiol groups and used to bind gold nanoparticles, leading to polymer-mediated spacing between nanoparticles and gold-enhanced photoluminescence (PL) of the CdS QDs.

In this paper, we show that a combination of synthesis by sequential RAFT polymerization, characterization by size exclusion chromatography-multi-angle laser light scattering detection (SEC-MALS) and modeling by molecular dynamics (MD) simulations, allows symmetric PAA-PS-TTC-PS-PAA copolymers to be prepared with both precise control and detailed understanding of the various interactions involving the copolymer blocks and the surrounding medium. These features are critical to establishing a versatile polymeric template on which to prepare a myriad of nanoparticle assemblies with finely-tuned distant-dependent interactions. In an effort to develop generalized approaches for templated functional nanostructures, we extend our previous demonstration of templated CdS QD synthesis [12] to the preparation of cadmium selenide (CdSe) QDs surrounded by solvated PS chains terminated by thiol functional groups. Compared to CdS QDs, CdSe QDs are much more common QD emitters in biophysical and photonic applications, due to their broader range of color tuneability in the visible spectral region.[35-

[37] We find significant solvent dependencies in the size, colloidal stability, and photoluminescence of the QD-containing RAFT block copolymer colloids, which lead us to a detailed study combining SEC-MALS experiments and MD simulations on analogous oligomers. The results provide valuable insights into the self-assembly of RAFT copolymers in different solvent systems as it relates to the preparation of emissive QDs with polymer-spaced thiol functionality. Thus, the combination of synthetic control, thermodynamic/structural understanding, and chemical versatility presented here, provides a powerful framework for color-tuned PL emission of QDs[35] with enhancements governed by polymer-mediated distances from chemically-bonded gold nanostructures. The CdSe QD micelles described herein and RAFT-based copolymers in general represent promising building blocks for future applications in functional optoelectronic devices, imaging probes, biomarkers, and sensors.

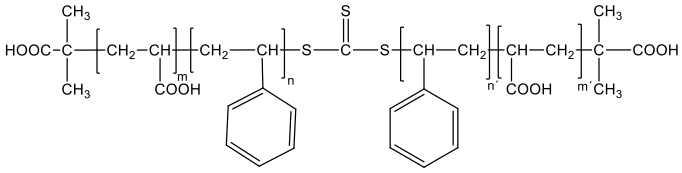

Scheme 2.1. Block copolymer PAA-*b*-PS-TTC-PS-*b*-PAA obtained by RAFT polymerization.

2.4. Experimental

2.4.1. Materials for Polymer Synthesis.

Carbon disulphide, chloroform, and acetone from Riedel-de-Haen, tetrabutylammonium hydrogen sulphate and diethyl ether from Fluka, *N*,*N*-dimethylformamide (DMF, PA) and tetrahydrofuran (THF, 99%) from Sigma-Aldrich, trioxane (99%) and 4,4'-azobis(4-

cyanovaleric acid) (ACVA, >98%) from Acros, and other chemicals obtained from several sources were used without further purification. Acrylic acid and styrene (Sigma-Aldrich) were distilled under vacuum before use.

2.4.2. Materials for SEC-MALS Characterization.

THF (99.9 %,), DMF (99.9 %), dioxane (99.9 %), LiBr and LiCl (reagent plus grade), and (trimethylsilyl)-diazomethane were purchased from Sigma-Aldrich.

2.4.3. Materials for Quantum Dot Micelle Synthesis.

Dioxane (99.9%), methanol (99.9%) and cadmium acetate dihydrate ($CdAc_2$, 98%) from Sigma-Aldrich and sodium selenide (Na_2Se, 99.8%) from Alfa Aesar, were used without further purification. Deionized water from a Millipore system Milli-Q ≥18 MΩcm was used for the preparation of solutions.

2.4.4. Synthesis of the Poly(acrylic acid)-*block*-polystyrene-TTC-polystyrene-*block*-poly(acrylic acid) Block Copolymer (PAA-*b*-PS-TTC-PS-*b*-PAA).

The 4-block copolymer was prepared as previously described.[11] We first prepared the RAFT chain transfer agent *S,S'*-bis(α,α'-dimethyl-α''-acetic acid) trithiocarbonate (TTC) following the procedure reported by Lai *et al.*[38] PAA and TTC were used in the RAFT polymerization of a symmetric copolymer with two poly(acrylic acid) blocks (PAA-TTC-PAA, Scheme 2.1), with number averaged molecular weight M_n = 3000 g mol^{-1} (M_w/M_n = 1.02), corresponding to a degree of polymerization <2 *n*> = 37.

The PAA-TTC-PAA copolymer was used as macro-CTA to prepare a PAA-*b*-PS-TTC-PS-*b*-PAA tetra-block copolymer. The RAFT polymerization of styrene resulted in a degree of polymerization <2 *m*> = 115 (Scheme 1), corresponding to a total copolymer molecular weight of M_n= 14900 g/mol. This was calculated from the 46% monomer conversion obtained by NMR of the polymerization mixture diluted 1:5 in acetone-d6, by

comparing the ratios of the integrated peaks of the vinyl protons of styrene and the methyl protons of DMF (used as an internal reference) before and after the polymerization.

Some of the tetra-block copolymer was silylated by adding 2.0 M (trimethylsilyl)-diazomethane in hexane solution, dropwise, into a solution of the PAA-*b*-PS-TTC-PS-*b*-PAA copolymer in THF (100 mg/13 mL THF) at room temperature.[39] Addition of the silylation agent was continued until the solution became yellow, after which an excess of methylation agent was further added. The reaction mixture was stirred at room temperature for 3 h more before the recovered polymer was injected in the SEC (without purification). To prove the symmetry of the copolymer (see below), we performed the aminolysis of 100 mg of the copolymer by dissolving the sample in 13 mL of THF and adding a 50-fold excess of hexylamine. The reaction was left shaking overnight at room temperature.

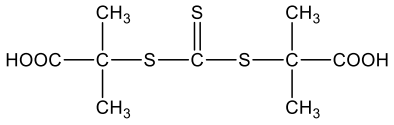

CTA

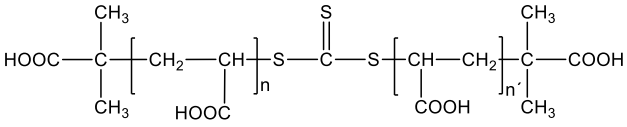

PAA-TTC-PAA macro CTA

Scheme 2.2. *S,S'*-bis(α,α'-dimethyl-α''-acetic acid) trithiocarbonate chain transfer agent (CTA) and PAA-TTC-PAA macroCTA.

2.4.5. Preparation and Characterization of Cadmium Selenide Quantum Dot Micelles (QDMs).

A sample of the PAA-*b*-PS-TTC-PS-*b*-PAA copolymer was diluted to 0.5 wt% with 1,4-dioxane (dioxane) and allowed to stir overnight at 25ºC in the dark to homogenize. A 0.25 M methanolic cadmium acetate dehydrate solution was added to the polymeric solution in

a 1:1 molar ratio of Cd^{2+} to COOH groups (from the PAA), and allowed to stir overnight at 25ºC in the dark. An aliquot (0.5 mL) of this sample was removed and diluted with 4 mL of a 1:1 mixture of toluene to dioxane (v/v) and stirred for 5 hours to homogenize. A 0.052 M solution of sodium selenide (Na_2Se) was prepared through the dilution of 0.013 g of Na_2Se with 2 mL of a 1:1 deionized water to methanol solution. The Na_2Se solution was added to the polymer solution such that the final mixture contained 0.3 moles of Se^{2-} per COOH group (160 µL). This solution was allowed to stir overnight in the dark.

2.4.6. Size Exclusion Chromatography (SEC).

SEC measurements were carried out using a Waters Associates equipment with a 510 pump, a 7725 Rheodyne injector and a differential refractive index detector (model 410). The multi-angle light scattering detector (MALS) was a miniDAWN TREOS laser photometer from Wyatt Technology Corp. The working temperature was 30 ºC. Three columns with a non-polar stationary phase (styrene-divinyl benzene copolymers) were generally used: one Styragel HR5 column (5 µm, 7.8 x 300 mm from Waters) and two linear Phenogel columns (5 µm, 7.8 × 300 mm from Phenomenex).[40] For the characterization of the copolymer in DMF and Dioxane and the methylated copolymer in THF only the two linear phenogel columns were used. The flow rate was 1 ml/min for THF, and 0.3 ml/min for DMF and Dioxane and the injector loop was 100 µl.

The refractive index (RI) detector measures the concentration of the polymer and the MALS detector (calibrated with spectrometric grade toluene) measures the excess Rayleigh ratio at different angles for each elution volume fraction of the chromatogram, allowing the calculation of the absolute molecular weight of the polymers. The normalization of the detectors in the different organic solutions was performed with low

molecular weight poly(styrene) standards. The shape of the chromatograms obtained with the MALS and the RI detectors are not coincident because the light scattering signal is proportional to the product of the polymer molecular weight and concentration, while the RI signal is proportional to the polymer concentration only.

To make sure there is no effect of the concentration on the SEC separation, for each solvent different concentrations were injected, decreasing from 8 mg/ml. In Appendix 2.1 we show that the juxtaposed traces of two injections at different concentration of the copolymer in dioxane have almost perfect matches of the MALS signal and the molecular weight calculated for each elution volume, with the refractive index signal reflecting the concentrations of the injected solutions.

SEC-MALS was used to study the aggregation behavior of the copolymer in different solvents: Dioxane; THF; THF with 0.1 M LiBr; THF with 0.2 M LiCl; DMF; and DMF with 0.15 M LiBr. To evaluate the influence of acrylic acid, the polymer was methylated and further analyzed in THF. The values used for the differential refractive index increment d*n*/d*c* at 632.8 nm were those of polystyrene (the major constituent of the polymer), 0.19 in THF, [41] 0.165 in DMF, [41] and 0.166 in dioxane.[42]

2.4.7. Photophysical Characterization.

Absorbance and reflectance measurements were performed on a Perkin Elmer Lambda 1050 UV/Vis/NIR spectrophotometer with a wideband 3 detector module. Fluorescence spectroscopy was performed on an Edinburgh Instruments FLS920 spectrometer with a 450W xenon arc lamp and a Hamatsu R5509 photomultiplier tube (PMT) detector. Slit widths were adjusted to achieve a 5 nm resolution, with a dwell time of 0.5 s.

2.4.8. Light Scattering.

The static and dynamic light-scattering measurements were conducted on a Brookhaven Instruments Co. BI-200SM research goniometer, with a Brookhaven Instruments Co. Mini-L30 30 mW red (636 nm) compact diode laser. The measurements were carried out in glass cylindrical cells in order to simplify the corrections needed for refractive index variations. The circular vat cell contains decalin to minimize light refraction. The dynamic light scattering (DLS) measurements were analyzed using the analysis package CONTIN (Brookhaven) to determine the translational diffusion coefficient, from which the hydrodynamic diameter (D_h) of the copolymer is calculated. To effectively remove dust from the solvent, this was filtered with Millipore 0.22 μm pore size filters.

2.4.9. Transmission Electron Microscopy (TEM).

Transmission electron micrographs were obtained on a JEOL JEM-1400 transmission electron microscope with a LaB_6 filament, equipped with a GatanOrius SC100 camera, with an accelerator voltage of 80 kV. TEM grids were prepared first by cooling an aluminum (Al) block in liquid nitrogen, a 300-mesh carbon-coated Cu TEM grid was placed on the Al block and 10 μL of CdSe QDM solution was dropped onto the grid and quickly immersed in liquid ethane. Solution was then placed under vacuum until dry. This likely resulted not in sublimation, due to insufficient vacuum, rather evaporation probably occurred.

2.4.10. Molecular Dynamics Computational Methods.

The Amber molecular modeling package, including the Amber force field, was employed for all the Molecular Dynamics (MD) simulations. Coulombic potentials were computed by the Ewald sum procedure. [45] Partial charges were assigned to every atom by means of the MOPAC package and the AM1 procedure. A time step $\delta = 1$ fs was employed for the

integration algorithm. The MD simulations were performed on Periodic Boundary Conditions (PBC) under NVT conditions (i.e. Canonical Ensemble), with the temperature being kept constant by means of the Berensen thermostat with a coupling factor of 1000 fs. Several exploratory calculations were performed at different temperatures ranging from 300 to 500 K. Finally, it was decided to perform all the calculations at 500 K in order to increase the atomic velocities, thus facilitating the passage over energetic barriers and consequently improving the statistical sampling of all the configurational space. Thus, the system is supposed to be in a hypothetical state in which the atomic velocities correspond to a rather high temperature while the density, interatomic distances, and in general all the equilibrium properties that are governed by the NVT conditions, are those of a much lower temperature. Even if this situation does not correspond to a real state of the system, the results of equilibrium properties obtained by this kind of simulations are much better than those obtained at the lower temperature at which the system will remain in the same energy well practically during the whole simulation. As it is evident, this approximation fails when applied to compute time dependent properties, but this kind of properties are not the goal of the present work.

Scheme 2.3 shows the structure of the model oligomers used in the MD simulations. The oligomers of type S (SA and SE) are formed by a central trithiocarbonate (TTC) unit, -S-(CS)-S-, flanked on each side by a block of 10 repeat units of styrene followed by a block of 11 repeat units of either acrylic acid (R = H, SA oligomer) or methyl acrylate ester (R = CH_3, SE oligomer). The oligomers of type C does not contain the central TTC unit, being formed by a central block of 22 units of styrene, flanked by on each side by 11 units of either acrylic acid (R=H, CA oligomer) or methyl acrylate ester (R = CH_3, CE oligomer).

Meso and racemic configurations of consecutive units were randomly assigned to each chain producing an overall fraction of meso diads $w_m \approx 0.4$. Ten oligomer chains were packed into a cubic box with Periodic Boundary Conditions (PBC), together with 2,000 molecules of the appropriate solvent and, in some cases, 200 molecules of salt (LiCl), to approach the experimental conditions (Figure A2.1).

The length of the PBC box (L) shown in the last column of Figure A2.1, was adjusted as to reproduce a macroscopic density of *ca.* 0.9 g cm^{-3}, similar to that of the organic solvents. However, each system was initially built within a box having approximately twice the final side length. The size of these initial boxes was progressively decreased, in 0.1 nm steps, by a combination of MD and energy minimization steps performed as follows: after each decrease of the box length, a 60 ps MD simulation was performed, during which the system was slowly warmed up from 0 to 500 K, equilibrated at this temperature during approximately 20 ps, then slowly cooled down to 0 K. Then, the energy of the system was minimized with respect to all internal coordinates with a combination of steepest descendent all conjugated gradient algorithms.[45] Once the system has reached the desired volume, it was slowly warmed up during 100 ps from 0 K to 500 K. Finally, the production stage was started for 3×10^6 integration cycles (*i.e.* a time span of 3000 ps), during which the coordinates of the system were recorded at intervals of 1 ps, thus producing a total of 3000 configurations that were further employed in the analysis. The warming step was not considered in the analysis.

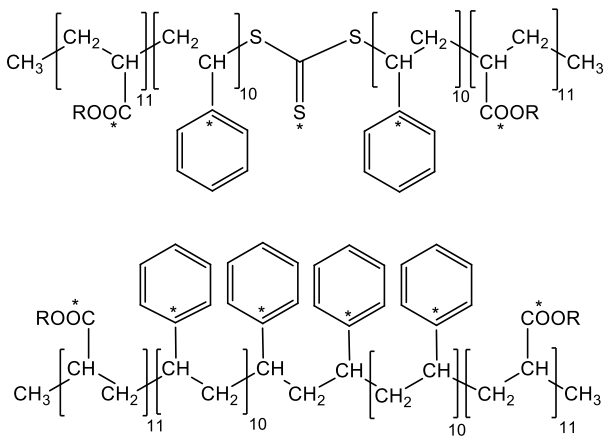

Scheme 2.3. Schematic representation of oligomer frameworks S (central TTC group, *top*) and C (no central TTC group, *bottom*) used for MD simulations. Based on these two frameworks, four different oligomers were investigated: SA and CA contain acrylic acid repeat units (*i.e.* R = H), while oligomers SE and CE contain methyl acrylate repeat units (*i.e.* R = CH_3).

2.5. Results and Discussion

2.5.1. Preparation and Characterization of Cadmium Selenide Quantum Dot Micelles.

Three different solvents were tested for the controlled self-assembly of the PAA-*b*-PS-TTC-PS-*b*-PAA copolymer: THF, DMF and 1,4-dioxane. Addition of cadmium acetate to the copolymer in each of the solvents was expected to lead to the formation of inverted micelles with a poly(cadmium acrylate) core and a corona of hydrophobic PS blocks. The hydrodynamic diameter D_h of the micelles prepared by addition of cadmium acetate was measured by dynamic light scattering and analyzed by CONTIN. The intensity distribution of D_h values (which highlight the larger species in dispersion), presented in Figure 1 A-C, show that the intensity-averaged effective hydrodynamic diameters are larger in THF (D_h = 55 nm) than in dioxane (D_h = 39 nm), indicating that, although well-defined micelles are formed in both solvents, these are probably more agglomerated in THF (Figure 2-1, A and

C). For the sample prepared in DMF (Figure 2-1 B) the intensity-averaged distribution reflects the possible presence of isolated chains and a broad distribution of aggregates.

The presence of isolated chains in the dispersions can be better observed in the number distributions of D_h. The breadth of these distributions (Figure A2.1) indicate that in the sample prepared in DMF, most of the species in dispersion correspond in fact to unassociated copolymer chains (D_h < 5 nm) and small aggregates with a broad size distribution (*RSD* = 200%). On the other hand, the predominant species in unfiltered samples prepared in dioxane and in THF are block copolymer micellar aggregates of similar and homogeneous size, with the relative standard deviations (*RSD*) of the number distributions showing that the sample prepared in dioxane (*RSD* = 50%) is slightly less heterogeneous than the one in THF (*RSD* = 60%).

We thus conclude that micelles prepared in dioxane are both homogeneous in size (unlike in DMF) and colloidally stable (unlike in THF).

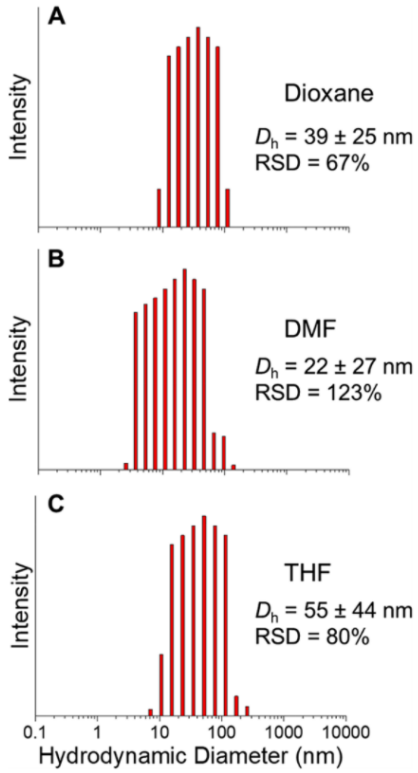

Figure 2-1 Hydrodynamic diameter intensity distributions obtained by CONTIN analysis of the DLS measurements of cadmium acrylate-core micelles in 1,4-dioxane (A), DMF (B) and THF (C). The average values of D_h were calculated directly from the histograms (presented with the width of the distribution and the corresponding relative standard deviations, *RSD*).

To better understand the relative thermodynamic stability of the cadmium acrylate micelles formed in THF and dioxane, we performed static light scattering (SLS) measurements in tandem with the DLS measurements. The samples were filtered with 0.45 μm Teflon filters to remove any larger aggregates (SLS is especially sensitive to dust and other large scatterers). It was observed that under identical conditions, only the sample in dioxane was capable of generating a stable dispersion of micelles (Figure A2.3). In both DMF and THF samples it was not possible to obtain meaningful Zimm plots, probably due

to aggregates evolving over time, during the measurements: the small aggregates and the micelle agglomerates previously detected by DLS for DMF and THF samples, respectively.

The SLS measurements of the cadmium acrylate reverse micelles in dioxane indicate a micellar molecular weight $M_w = (1.4 \pm 1) \times 10^6$ g·mol^{-1}, a radius of gyration $R_g = (24 \pm 4)$ nm and a second-virial coefficient $A_2 = (3.4 \pm 1.7) \times 10^{-5}$ cm^3·mol·g^{-2}. Although these data were obtained for samples filtered with 0.45 μm Teflon membranes while the intensity-averaged DLS measurements in Figure 2-1 Hydrodynamic diameter intensity distributions obtained by CONTIN analysis of the DLS measurements of cadmium acrylate-core micelles in 1,4-dioxane (A), DMF (B) and THF (C). The average values of *Dh* were calculated directly from the histograms (presented with the width of the distribution and the corresponding relative standard deviations, *RSD*). were performed with unfiltered samples, there is a good correspondence between the these results, with the ratio $R_g / (D_h / 2) = 1.2 \pm 0.1$ indicating a star-like micelle structure with a corona of random coil chains. The second virial coefficient value is small but positive, indicating that the intermicellar interaction is repulsive (i.e. the micelles are stable in dioxane). The meaning of this value can be better understood by expressing the second virial coefficient as a hard-sphere virial diameter, D_{A2}, which corresponds to a sphere where only the excluded volume effect has been taken into account: [44]

$$D_{A2} = 2\left(\frac{3M_W^2 A_2}{16\,\pi\, N_A}\right)^{\frac{1}{3}} \quad (1)$$

where M_w is the molecular weight of the micelles and N_A the Avogadro number. While for noninteracting spherical particles, D_{A2} should be very close to the hydrodynamic dimeter, our micelles in dioxane have D_{A2} = 37.5 nm, [44] a smaller mean value than the intensity-

averaged D_h = 39 nm obtained by DLS (Figure 2-1), as expected for star-like block copolymer micelles with a "soft" outer shell leading to steric stabilization.

The poly(cadmium acrylate) core of the micelles were then used as nanoreactors to prepare CdSe QDs by adding Na_2Se in an approximately 50/50 (v/v) mixture with toluene. Formation of a CdSe QD at the micelle core originates a quantum dot micelle (QDM, cartoon in Scheme 2.4) where the QD is encapsulated by a PS shell. These experiments produced clear yellow colloidal dispersions when 1,4-dioxane was used in the preparation of the micelles (Figure 2-2A, top). With both DMF and THF we obtained slightly turbid dispersions (Figure 2-2, B and C, top), which precipitated overnight (Figure A2.4). Furthermore, the typical emission of CdSe quantum dots (observed under 365 nm illumination in Figure 2-2, bottom) was only clearly observed for the sample prepared with 1,4-dioxane.

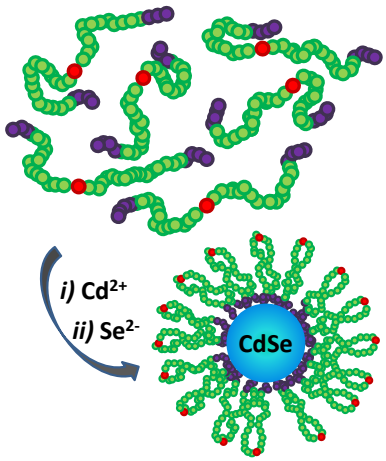

Scheme 2.4. Cartoon representation of the CdSe quantum-dot micelle (QDM) structure. The PAA-*b*-PS-TTC-PS-*b*-PAA block copolymers self-assemble in dioxane upon addition of $CdAc_2$, forming micelle nanoreactors with a core of cadmium-crosslinked PAA blocks (*purple*) and a flower-like corona of PS blocks (*green*) with a TTC group (*red*) at each "petal". The CdSe QD is formed at the micelle core by addition of Na_2Se.

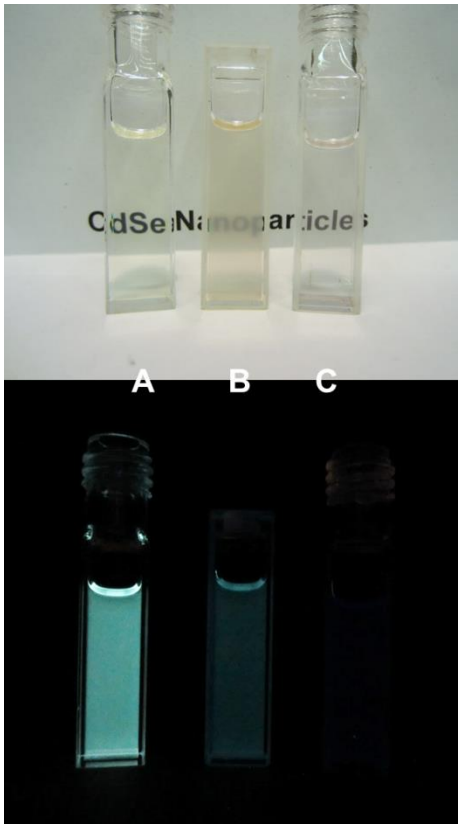

Figure 2-2 Photographs of CdSe QDMs in the three solvent composition under ambient (Top) and 365 nm (Bottom) light. Samples A-C correspond to Dioxane/Toluene, DMF/Toluene and THF/Toluene 50/50 (v/v) mixtures respectively. Figure A2.4 shows that samples B and C produce significant precipitate at the bottom of the vials after overnight settling.

In the case of the sample prepared in 1,4-dioxane, the obtained CdSe QDMs are clearly visible by TEM (Figure 2-3A). Due to electron densities, only the CdSe QDs in the micelle cores are observed. From the TEM images, and by measuring *ca.* 170 QDs, we determined a size distribution corresponding to a mean QD diameter of 3 nm with a population standard deviation of 2 nm. The CdSe QDMs dispersed in a 50/50 mixture of dioxane and toluene (v/v) measured by DLS following filtration through 0.45 μm Teflon

filters, have a number-averaged effective hydrodynamic diameter of 20 nm with a population standard deviation of 5 nm (Figure 2-3B), which compares to D_h = 14 nm obtained for the cadmium acrylate-core micelles prepared in 1,4-dioxane (Figure A2.2). The UV-vis. absorption of the QDM prepared in 1,4-dioxane (Appendix 2.4) is typical of CdSe QDs, with both the excitation and photoluminescence spectra featuring bands that do not change with the excitation wavelength, and are characteristic of quantum confinement effects (Figure 2-4).

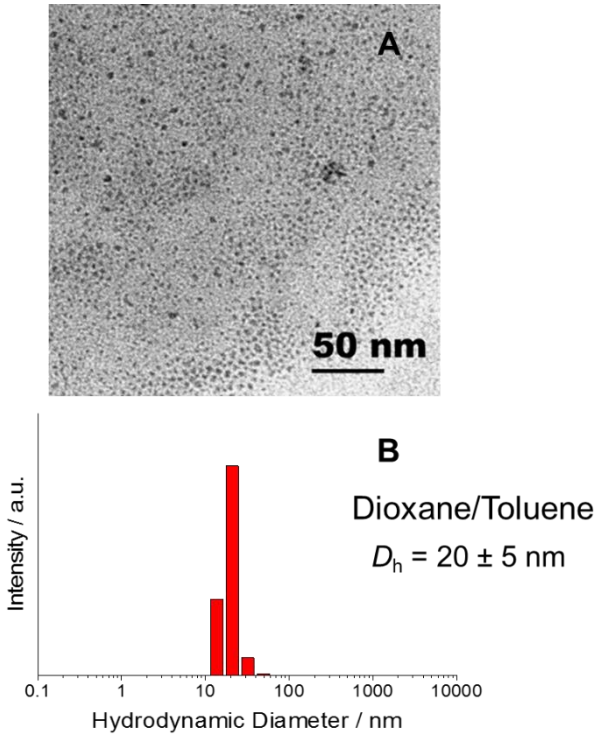

Figure 2-3. (A) Transmission electron micrograph of CdSe QDMs deposited from dioxane with a mean QD diameter of 3 nm with a population standard deviation of 2 nm, shown with a 50 nm scale bar. (B) Hydrodynamic diameter D_h number distribution generated by CONTIN fit of dynamic light scattering measurements of CdSe QDMs in a 50/50 mixture of dioxane and toluene (v/v), following filtration through 0.45 μm Teflon filters. The average value of D_h was calculated

directly from the histogram. The number-averaged effective hydrodynamic diameter is D_h = 20 nm, with a population standard deviation of 5 nm.

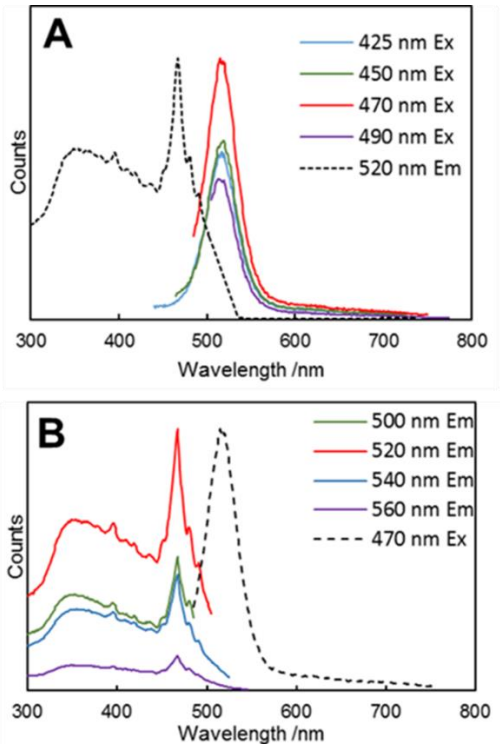

Figure 2-4. Photoluminescence spectra of CdSe QDMs in a 50/50 mixture of dioxane and toluene (v/v). (A) Emission spectra at four different excitation wavelengths (collected with a 10x neutral density filter, normalized by their relative intensity to the most emissive run, i.e. 470 nm), taken around the exciton peak. Excitation spectrum collected at 520 nm (normalized at λ_{max} = 470 nm) included for reference. (B) Excitation spectra at four different emission wavelengths (normalized by their relative intensity to the most emissive run, i.e. 520 nm). Emission spectrum with excitation at 470 nm (normalized at λ_{max} = 520 nm) included for reference.

The formation of small aggregates in DMF upon addition of cadmium acetate, instead of the homogenous micellar aggregates observed in THF and dioxane, appears to lead to core fusion/aggregation when the CdSe nanocrystals grow in this solvent, leading to the formation of large, colloidally unstable and non-emissive CdSe crystals that precipitate overnight. In the case of THF, although cadmium acetate micelles are initially

formed as in dioxane, the micelles are less stable than in dioxane and lead to CdSe nanocrystals with very low emission that precipitate overnight.

Static light scattering of the final CdSe QDMs obtained in dioxane (Figure A2.3 B) yielded a micelle molecular weight of $M_w = (1.2 \pm 0.4) \times 10^6$ g mol^{-1}. Using the molar mass of the copolymer chain (Table 2.1), we calculate a micellar aggregation number of 80 ± 27.

Considering the copolymer structure and the colloidal stability of the micelles, these probably have a flower-like structure, with the TTC groups at the apex of each PS "petal", consisting of the central PS block that folds during self-assembly to allow the outermost PAA blocks in each chain to be incorporated into the core, as represented in the cartoon in Scheme 2.4.

A deeper understanding of the self-assembly behavior of the RAFT copolymer in various solvents is germane to its application as a template for CdSe QDs and gold nanoparticle-QD composite nanostructures. Therefore, in order to gain insight into why stable and emissive CdSe dispersions were obtained in 1,4-dioxane, but not in THF or DMF, we conducted a thorough characterization of the PAA-*b*-PS-TTC-PS-*b*-PAA block copolymer in the different solvents. To probe the different interactions at play, we used a combination of size exclusion chromatography with multi-angle laser light scattering detection (SEC-MALS) and Molecular Dynamics (MD) simulations, note that this work was completed by our collaborators in Portugal and Spain.

2.5.2. Characterization of the PAA-*b*-PS-TTC-PS-*b*-PAA Block Copolymer.

Size exclusion chromatography (SEC) coupled to a mass-sensitive detector, such as viscosity or light scattering, is the most common experimental technique to verify the

level of control over copolymer architecture and molecular weight. The combination of a refractive index (RI) detector (sensitive to concentration) with a multi-angle laser light scattering (MALS) detector is particularly advantageous since it offers the possibility of obtaining both absolute molecular weights and chain dimensions along the chromatogram, as well as information of the solvent-polymer interactions. In the case of block copolymers, the characterization by SEC-MALS is complicated by differences in solvent quality for the blocks, which can lead to the formation of micellar aggregates in the eluting solvent. Although the self-assembly behavior is critical to the application of the copolymers as templates for nanostructured materials, it provides a serious challenge to the definitive SEC-MALS characterization of their molecular weights, since aggregation in the eluting solvent can lead to erroneous assignment of molecular weights and strong deviations in measured molecular weights and chain dimensions in different solvents. This is aggravated for copolymers carrying charged monomers since salts are sometimes added to the solvent in order to screen electrostatic interactions, potentially leading to further changes in aggregation behavior.

The SEC-MALS characterization of asymmetric poly(styrene-*b*-acrylic acid) copolymers is described in the literature, but often yields different values of apparent molecular weight and size dispersity in tetrahydrofuran (THF), *N*,*N*-dimethylformamide (DMF) and 1,4-dioxane (dioxane).[32] These discrepancies are probably related to the different results we obtained in the self-assembly of our block copolymer and subsequent preparation of the QDMs. In order to clarify this relation, we measured the molecular weight and dimensions of our copolymers by SEC-MALS in the three solvents, 1,4-dioxane, THF and DMF, varying the dielectric properties of the last two by adding lithium

salts. Both THF and dioxane are good solvents for polystyrene (PS), while DMF is a marginally good solvent for PS (Mark-Houwink-Sakurada exponents of 0.749, 0.694 and 0.603, respectively). No data on the quality of either THF or DMF to PAA could be found in the literature, while dioxane has been reported to be a θ solvent for PAA at 30 °C (the working temperature of the SEC-MALS in these experiments).

The chromatograms obtained in THF (Figure 2-5A) show that the peaks are broader and displaced towards lower elution volumes (*i.e.* higher hydrodynamic volumes) compared to those obtained when we used THF with 0.2 M LiCl (Figure 2-5B) or with 0.15 M LiBr (Figure A2.6). The same trend was observed when using DMF as eluent and we added 0.15 M LiBr (Figure A2.6). This behavior suggests the presence of electrostatically-mediated aggregation of copolymer chains that change with the addition of salt, which is supported by the shift between MALS and RI signals in Figure 2-5. These are large polymer aggregates with a broad size distribution, as indicated by the radius of gyration curve obtained from the light scattering (SEC-MALS) experiments (Figure 2-5 and Figure A2.6). The aggregates are formed by the collapse of the polymer chains in poor solvents (THF and DMF) to form globules that aggregate into unstable colloidal structures. On the other hand, if we use dioxane, the MALS and RI curves are similar, with maxima appearing at the same elution volume (Figure 2-6), as expected for non-aggregated (isolated) chains with low size dispersity.

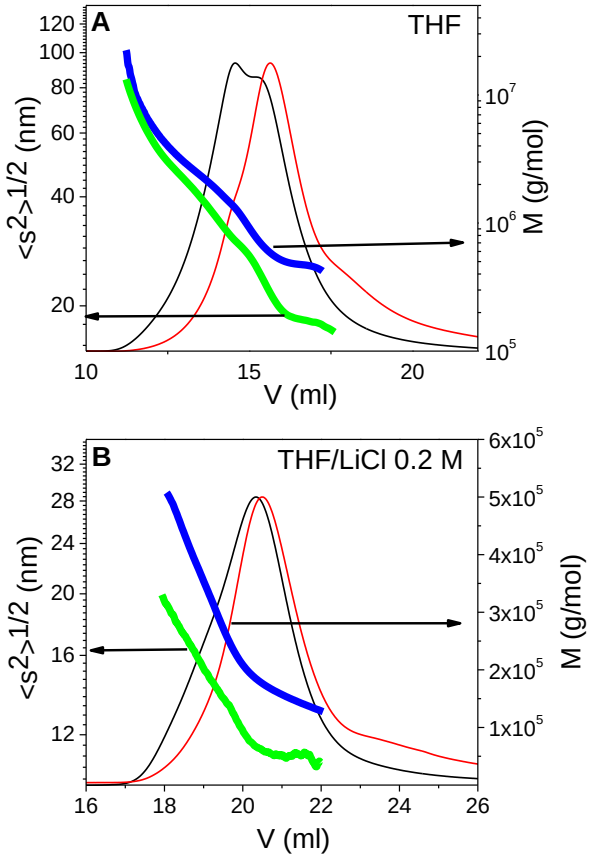

Figure 2-5. Refractive index signal (*red*) and the MALS signal at 90º (*black*) versus elution volume. Molecular weight (*blue*) and radius of gyration (*green*) calculated for each elution volume for the copolymer in THF (A) and THF with 0.2 M LiCl (B).

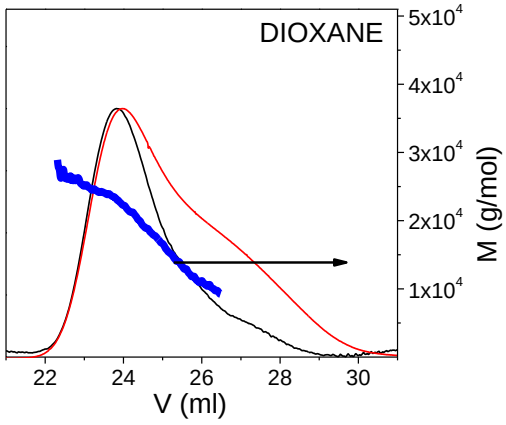

Figure 2-6. Refractive index signal (*red*) and the MALS signal at 90º (*black*) versus elution volume. Molecular weight (*blue*) calculated for each elution volume for the copolymer in dioxane.

In order to understand the effect of the acrylic acid (AA) units in the aggregation of the block copolymer in THF and DMF, the PAA-*b*-PS-TTC-PS-*b*-PAA copolymer was silylated by converting the AA of the PAA blocks using (trimethylsilyl)-diazomethane.[40] When the modified polymer was analyzed in THF (Figure 2-7) we observed that the chromatograms are similar to those obtained for the non-modified copolymer in dioxane, with the maxima of the MALS and RI curves appearing at the same elution volume. This shows that the polar nature of the PAA groups are germane to the aggregation behavior of the copolymer in THF, and further suggests that dioxane is a nonselective solvent for the copolymer, since silylation is not required to suppress aggregation in that solvent.

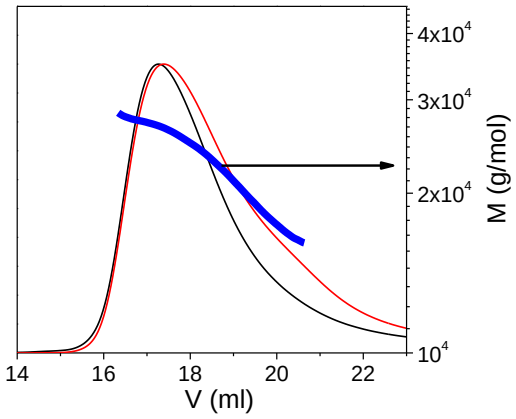

Figure 2-7. Refractive index signal (*red*) and the MALS signal at 90º (*black*) versus elution volume. Molecular weight (*blue*) calculated for each elution volume for the silylated copolymer in THF.

The molecular weight and radius of gyration *versus* elution volume obtained for the copolymer in THF (Figure 2-5 A) and DMF (Figure A2.6 A) indicate poor chromatographic separation since they do not cover the full range of the MALS and refraction index peaks. The addition of salt displaces the curves to lower values of

molecular weight and radius of gyration, due to the disruption of the aggregates: in THF, the lowest values of molecular weight are obtained with 0.2 M LiCl (Figure 2-5B); in DMF, the addition of 0.15 M LiBr (Figure A2.6 B) produces a significantly larger effect on the decrease of molecular weight and radius of gyration than the addition of the same salt to THF. Table 2.1 summarizes the average values of the molecular weight and the radius of gyration of the copolymer and its size dispersity in different solvents.

Although polymer aggregates can be partially disrupted by salt addition in THF and DMF, even for the more effective salts (0.2 M LiCl in THF and 0.15 M LiBr in DMF), the determined molecular weights are considerably larger than the value determined in dioxane (Figure 6, $M_w = 1.6 \times 10^4$ g mol^{-1}; $M_w/M_n = 1.13$), which is very close to the values obtained for the methylated polymer in THF after correction for the additional methyl groups (Figure 7, $M_w = 1.5 \times 10^4$ g mol^{-1}; $M_w/M_n = 1.10$). The later values are also in good agreement with the molecular weight estimated from the conversion obtained by ^{1}H NMR (1.5×10^4 g mol^{-1}). For the copolymer in dioxane, the size dispersity measured by SEC-MALS is typical of RAFT polymerization.

Table 2-1. Average molecular weight (M_w), dispersity (M_w/M_n) and root mean square radii of gyration $\langle s_z^2 \rangle^{1/2}$ calculated by SEC-MALS for the PAA-*b*-PS-TTC-PS-*b*-PAA copolymer in different solvents.

Solvent	M_w/ 10^5 (g/mol)	$\langle s_z^2 \rangle^{1/2}$ (nm)	M_w /M_n
THF	7.6	22	1.5
THF/0.15 M LiBr	6.1	22	1.6
THF/0.20 M LiCl	1.9	12	1.3
DMF	2.7	75	1.7
DMF/0.15M LiBr	0.34	13	1.2
Dioxane[b]	**0.16**	**5.3** [a]	**1.1**
Silylated copolymer in THF	0.23	-	1.1

[a] Estimated from the hydrodynamic radius measured by DLS (see text).

[b] Values in this solvent correspond to single copolymer chains whereas values in other solvents represent various states of copolymer chain aggregation (see discussion in text).

It is not possible to determine the radius of gyration curve for the non-aggregated copolymer in dioxane, nor the methylated copolymer in THF, because its small value is beyond the detection limit of MALS detector. However, this value can be estimated using dynamic light scattering (DLS) measurements. The hydrodynamic radius of the copolymer chains at low concentration in dioxane, determined by DLS, is $R_h = (3 \pm 1)$ nm. Burchard has shown that for random coils in good solvents, the ratio R_g / R_h can be estimated to be 1.78. Thus the measured value of R_h corresponds to a radius of gyration of $R_g = R_h \times 1.78 = 5.3$ nm, which is significantly smaller than the R_g measured by SEC-

MALS for the copolymer aggregates in both THF and DMF (Table 2.1). The hydrodynamic radius of the copolymer in dioxane is practically constant up to polymer concentrations of ca. 1.5 g/L (Figure A2.7 A), with higher concentrations showing aggregate formation (Figure A2.7) that prevents the determination of the radius of gyration and second virial coefficient by static light scattering (SLS, Figure A2.7 B). We thus conclude that, in order to have free copolymer chains in solution, characterization of this and similar copolymers by SEC-MALS, DLS, and SLS should be carried out below 1.5 g/L in dioxane.

Finally, to evaluate the relative size of the two PS-*b*-PAA sections on either side of the central TTC group, the TTC group was cleaved with hexylamine. The molecular weight of the resulting PS-PAA chains was half the initial value, indicating that the tetra-block copolymer has a symmetrical architecture, as expected from the structure of the trithiocarbonate chain transfer agent.

2.5.3. Molecular Dynamics (MD) Simulations.

To better understand the interactions between the different blocks in the copolymer and the various solvents used in block copolymer characterization and self-assembly experiments, we performed molecular dynamics (MD) simulations in four model tetrablock oligomers containing blocks of 10 repeat units each (Scheme 2.3): two type S oligomers composed of a central trithiocarbonate (TTC) unit flanked by two inner styrene blocks and two outer blocks of either acrylic acid (SA) or methyl acrylate ester (SE); and two type C oligomers without a central TTC unit and two outer blocks of either acrylic acid (CA) or methyl acrylate ester (CE).

The simulations allow the calculation of distances between different atoms in the oligomers, and between various atoms in the oligomers and the solvent molecules. We have selected the following three types of atoms to follow within each oligomer chain, marked with an asterisk in Scheme 2.3:

1.) the central sulfur atom of the TTC group of type S oligomers (one atom per oligomer, labeled S*);

2) the oxygen atom of the carboxyl groups of type S and type C oligomers (22 atoms per oligomer chain, labeled O*); and

3) the aromatic C atom of each phenyl group that is linked to the chain of the type S (20 atoms per oligomer chain, labeled C*) and type C oligomers (22 atoms per oligomer chain, labeled C*).

The oligomer-solvent distances correspond to the average separation relative to the center of mass of each of the 2,000 solvent molecules in each system. Distances of interest were computed for all the configurations recorded during the MD trajectories. The radial correlation function $g(r)$ was calculated from the ratio between the probability of finding two atoms at a distance $r \pm \delta r$ to the same probability for a random distribution of atoms, using $\delta r = 0.01$ nm.

2.5.4. MD Simulations of Type S Methyl Acrylate Oligomers in THF (SE-THF).

The simulation results obtained for the methylated oligomer with a central TTC group in THF (SE-THF) were used as reference to which the other systems were compared. Appendix 2.8 shows the radial correlation function $g(r)$ for the intramolecular (Figure 2.8 A), intermolecular (Figure A2.8 B) and oligomer-solvent distances (Figure A2.8 C). The broad, approximately Gaussian, profile in Figure A2.8 A shows that the oligomer chain is

in a coiled conformation, without observable correlation among different parts of the chain. THF is a good solvent for PS and consequently the central part of the oligomer is quite extended producing a rather large separation (at least by 2.5 nm) among the O* atoms of the acrylic units at both ends of the oligomer, without noticeable correlation. On the other hand, Figure A2.8 B shows a noticeable displacement of the intermolecular O*…O* peaks of the correlation function towards shorter distances, but the value of $g(r)$ is close to 1 from 1 to 4 nm, which indicates absence of correlation (and interaction) between the methylated groups in different chains. Moreover, the S*…S* interchain correlation shows a sharp peak at ca. 0.5 nm which is attributed to the hydrophobicity of the trithiocarbonate group contributing to the approximation of different oligomers in a polar solvent such as THF.

The oligomer-solvent correlation curves shown in Figure A2.8 C indicate that the coiled chains are uniformly solvated, with no evidence of preferential solvation of any part of the methylated chains in THF. The distribution of solvent molecules is similar around the S* atoms (central part of the oligomer chains), the C* atoms and the O* atoms (chain ends). The first solvation shell is placed at a slightly larger distance in the case of C* atoms, but this is due to the larger size of the phenyl groups to which the C* atoms belong.

2.5.5. MD Simulations of Type S Acrylic Acid Oligomers in THF (SA-THF).

Figure A2.9 shows that the distribution function of intramolecular distances for both S*…O* and O*…O* are similar in SE-THF and SA-THF (Figure A2.8 and A2.9). This is a consequence of THF being a good solvent for PS, which favors the extended conformations of the central part of the chain, keeping the acrylic acids units away from each other. On the other hand, the correlation of S*…S* intermolecular distances observed at $r \approx 0.5$ nm for SE-THF (Figure A2.8 B) is not present in SA-THF (Figure A2.9 B).

Instead, a much stronger correlation of the O* … O* intermolecular distances is observed at approximately the same value of *r*. The intensity and sharpness of this peak suggest that several oligomers could aggregate through the acrylic units. Appendix 2.9 C shows that the correlation of the solvent molecules with the S*, C* and O* atoms is similar to SE-THF (Figure A2.8 C), indicating that the chains are uniformly solvated. The same result is observed for the systems SA-THF/Li (Figure A2.10 C) and SA-Dioxane (Figure A2.11 C).

2.5.6. MD Simulations of Type S Acrylic Acid Oligomers in THF with LiCl Salt (SA-THF/Li).

Figure A2.10 shows that the addition of salt to THF does not change the intramolecular O*…O* and S*…O* distance correlations, and that the correlation for the intermolecular S*…S* distance is also very similar to that of SA-THF shown above. However, addition of the salt modifies the intermolecular interactions among acrylic groups which fall in between those of SE-THF and SA-THF (compare the broken lines in Figure A2.6 B, A2.7 B and A2.8 B). These results indicate that, although aggregation persists, salt addition helps disrupt the interactions among the acrylic acid units of different chains.

2.5.7. MD Simulations of Type S Acrylic Acid Oligomers in Dioxane (SA-Dioxane).

Figure A2.11 shows that the correlations for intramolecular S*…S* and O*…O* distances are very similar to those obtained for both SA and SE in THF, although the peaks are shifted towards lower values of *r* due to the fact that dioxane is a worse solvent for PS than THF. Although the S*…S* intermolecular distance distribution is shifted to higher values, indicating a lower tendency to aggregation driven by the trithiocarbonate group, the O*…O* intermolecular distances are similar to those in THF. This result suggests that, at least for the simulated oligomers, the tendency for aggregation (experimentally observed

in THF, but not in dioxane), is mainly driven by the TTC groups rather than by the PAA blocks.

2.5.8. MD Simulations of Oligomers without the TTC Group.

Finally, in order to understand the role of the central trithiocarbonate (TTC) group we considered oligomers without this group. The CE and CA oligomers used in these calculations are formed by a block of 22 repeat units of styrene flanked on each side by a block of 11 repeat units of either acrylic acid (CA oligomer) or methyl acrylic ester (CE oligomer) as shown in Scheme 2.3. The carbon atom of the central CH_2 group of both CE and CA oligomers is used as the origin to measure the distances for the evaluation of the correlation functions (similarly to the central S atom of the SE and SA oligomers), and is represented as CC in Figure A2.12. The most important conclusion of the calculations is that when the TTC group is not present (CE-THF; solid line in Figure A2.12 B), the sharp peak appearing at *ca.* 0.4 - 0.5 in the SE-THF case (Figure A2.8 B) disappears, suggesting that the TTC hydrophobic interactions play an important role in the aggregation of TTC-containing chains in THF.

Comparing the results computed for CA-THF (Figure A2.12) with those of SA-THF (Figure A2.9), the O*…O* distances (both intra and inter) are very similar for both systems, the distribution for intermolecular CC…CC distance (solid line in Figure A2.12 B) is also similar to the S*…S* intermolecular distance distribution in SA-THF (solid line in Figure A2.9 B). The main difference is that for S*...S* we observe values of $g(r) > 1$ for very short distances ($r < 1$ nm), whereas the CC…CC intermolecular distance distribution is shifted to higher values of r. This displacement indicates a lower tendency to aggregation in the absence of the TTC group. Thus we conclude that the TTC group is responsible,

together with the acrylic groups, for the strong aggregations among the oligomers in THF solutions.

2.5.9. Discussion of SEC-MALS and MD Results and Importance for Characterization and Self-Assembly of PAA-*b*-PS-TTC-PS-*b*-PAA.

The TTC group located precisely at the center of our unique copolymers gives us a chemical handle on binding gold nanostructures at a controlled distance from the CdSe QDs prepared by using the self-assembled copolymer template. However, the TTC group also presents special challenges, not only for copolymer characterization, but also for selecting appropriate conditions for its self-assembly. This adds to the problems already reported in the literature for characterizing PS-b-PAA chains without the TTC. Our detailed SEC-MALS and MD results helped us identified the main causes for the uncontrolled aggregation of the copolymer in various solvents, pointing the way to its successful characterization and controlled self-assembly conditions. While MD calculations suggest that the TTC groups play a pivotal role in the aggregation of the simulated oligomers, absent only when dioxane is used as solvent, the interaction between PAA blocks is expected to become more important for larger chains. In fact, this interaction was proved a key factor in the SEC-MALS experiments, in which aggregation could be eliminated by reducing the interaction between PAA blocks, both in THF by methylation of the copolymer, and by dissolving the copolymer in dioxane. These results allowed us to understand the appropriate conditions for the characterization of the block copolymer chains, and to select the best strategy to achieve their controlled self-assembly for application as nanoparticle scaffolds.

The fact that we could only measure isolated PAA-*b*-PS-TTC-PS-*b*-PAA copolymer chains in dioxane, explains why only in this solvent it was possible to obtain

the desired templates to prepare CdSe QDs by adding cadmium acetate to selectively associate the PAA blocks. The lower stability of cadmium acetate micelles prepared in THF and the heterogeneous aggregation in DMF ultimately resulted in extensive aggregation and precipitation of non-emissive CdSe crystals.

2.6. Conclusions

We used RAFT to prepare a symmetric tetrablock copolymer of precisely controlled architecture composed of a trithiocarbonate (TTC) central group, two polystyrene inner blocks, and two acrylic acid outer blocks. The TTC functional group offers the capability of using this copolymer as a unique scaffold for quantum dot-gold nanoparticle composites, but also introduces challenges to controlled self-assembly, due to its contributions to the aggregation behavior of the chains in various solvents. This was evidenced by our unsuccessful attempts to produce well-dispersed and luminescent CdSe QDs in RAFT copolymer templates using DMF and THF as dispersing solvents.

We carried out a thorough SEC-MALS study of the copolymer in different solvents to better understand its aggregation behavior. In THF and DMF, the copolymer has a strong tendency to aggregate, as evidenced by the measured high molecular weights, with addition of salts lowering molecular weights but not to the level of single chains. In dioxane, the results agreed with those obtained for the modified copolymer in THF after methylation of acrylic acid groups to suppress aggregation, suggesting that dioxane is a nonselective solvent for the copolymer, capable of dispersing single chains. Further, MD simulations showed that hydrogen bonding between the acrylic acid units is the probable main cause of interchain interactions leading to aggregation in THF and DMF, but not in dioxane. MD simulations also confirmed that salt addition to THF and DMF only partially disrupt ion

pairs formed by incomplete dissociation of the acid units, and that the hydrophobic central TTC group contributes to the stabilization of the aggregates in THF and DMF.

Controlled self-assembly *en route* to nanostructure synthesis was achieved by using dioxane to fully dissolve the copolymer and then adding cadmium acetate to induced segregation of the PAA blocks that self-assemble into spherical inverted micelles of homogeneous size. These micelles were then used as nanoreactors in the templated synthesis of a single CdSe quantum dot within each core, expanding our earlier demonstration of CdS synthesis in the same copolymer to a more common and useful color-tunable emitter. This combination of controlled RAFT polymerization, SEC-MALS measurement and MD modeling in a variety of solvents, and the demonstrated versatility of nanoparticle templating, provides the framework for a general and powerful strategy for surface plasmon-enhanced PL emission in nanoparticle-based devices.

2.7. Appendix

Additional SEC-MALS experimental results for the characterization of the PAA-*b*-PS-TTC-PS-*b*-PAA copolymer (and its aggregates) in different solvents, average hydrodynamic diameter calculated from the number-weighted distribution obtained by dynamic light scattering of the copolymer in 1,4-dioxane, SLS Zimm plots of the coplymer and the QDMs in 1,4-dioxane, and plots of the radial correlation functions obtained from the MD trajectories for the simulated oligomers in different solvents. This material is available free of charge via the Internet at http://pubs.acs.org

2.8. Acknowledgements

This work was partially supported by Fundação para a Ciência e a Tecnologia (FCT-Portugal) and COMPETE (FEDER), within projects UID/NAN/50024/2013 and PTDC/CTM-POL/3698/2014. T.R. also thank FCT for Post-Doc grant SFRH/BPD/96707/2013.

2.9. References

(1) Whitesides, G. M.; Grzybowski, B. Self-Assembly at All Scales. *Science* **2002,** *295*, 2418-2421.

(2) Cummins, C. C.; Schrock, R. R.; Cohen, R. E. Synthesis of zinc sulfide and cadmium sulfide within ROMP block copolymer microdomains. *Chem. Mater.* **1992,** *4*, 27-30.

(3) Möller, M.; Spatz, J. P.; Roescher, A. Gold nanoparticles in micellar poly(styrene)-b-poly(ethylene oxide) films—size and interparticle distance control in monoparticulate films. *Adv. Mater.* **1996,** *8*, 337-340.

(4) Moffitt, M.; Eisenberg, A. Size Control of Nanoparticles in Semiconductor-Polymer Composites. 1. Control via Multiplet Aggregation Numbers in Styrene-Based Random Ionomers. *Chem. Mat.* **1995,** *7*, 1178-1184.

(5) Wang, C. W.; Moffitt, M. G. Use of Block Copolymer-Stabilized Cadmium Sulfide Quantum Dots as Novel Tracers for Laser Scanning Confocal Fluorescence Imaging of Blend Morphology in Polystyrene/Poly(methyl methacrylate) Films. *Langmuir* **2005,** *21*, 2465-2473.

(6) Shang, L.; Dong, S.; Nienhaus, G. U. Ultra-small fluorescent metal nanoclusters: Synthesis and biological applications. *Nano Today* **2011,** *6*, 401-418.

(7) Mai, Y.; Eisenberg, A. Self-assembly of block copolymers. *Chem. Soc. Rev.* **2012,** *41*, 5969-5985.

(8) Lee, J.; Govorov, A. O.; Kotov, N. A. Nanoparticle Assemblies with Molecular Springs: A Nanoscale Thermometer. *Angew. Chem.* **2005,** *117*, 7605-7608.

(9) Wang, M.; Kumar, S.; Lee, A.; Felorzabihi, N.; Shen, L.; Zhao, F.; Froimowicz, P.; Scholes, G. D.; Winnik, M. A. Nanoscale Co-organization of Quantum Dots and Conjugated Polymers Using Polymeric Micelles As Templates. *J. Am. Chem. Soc.* **2008,** *130*, 9481-9491.

(10) Nie, Z.; Petukhova, A.; Kumacheva, E. Properties and emerging applications of self-assembled structures made from inorganic nanoparticles. *Nat Nano* **2010,** *5*, 15-25.

(11) Moffitt, M. G. Self-Assembly of Polymer Brush-Functionalized Inorganic Nanoparticles: From Hairy Balls to Smart Molecular Mimics. *The Journal of Physical Chemistry Letters* **2013,** *4*, 3654-3666.

(12) Ribeiro, T.; Prazeres, T. J. V.; Moffitt, M.; Farinha, J. P. S. Enhanced Photoluminescence from Micellar Assemblies of Cadmium Sulfide Quantum Dots and Gold Nanoparticles. *J. Phys. Chem. C* **2013,** *117*, 3122-3133.

(13) Ray, K.; Badugu, R.; Lakowicz, J. R. Metal-Enhanced Fluorescence from CdTe Nanocrystals: A Single-Molecule Fluorescence Study. *J. Am. Chem. Soc.* **2006,** *128*, 8998-8999.

(14) Liu, N.; Prall, B. S.; Klimov, V. I. Hybrid Gold/Silica/Nanocrystal-Quantum-Dot Superstructures: Synthesis and Analysis of Semiconductor−Metal Interactions. *J. Am. Chem. Soc.* **2006,** *128*, 15362-15363.

(15) Fedutik, Y.; Temnov, V.; Woggon, U.; Ustinovich, E.; Artemyev, M. Exciton−Plasmon Interaction in a Composite Metal−Insulator−Semiconductor Nanowire System. *J. Am. Chem. Soc.* **2007,** *129*, 14939-14945.

(16) Kim, B.-S.; Taton, T. A. Multicomponent Nanoparticles via Self-Assembly with Cross-Linked Block Copolymer Surfactants. *Langmuir* **2007,** *23*, 2198-2202.

(17) Chen, C. W.; Wang, C. H.; Wei, C. M.; Chen, Y. F. Tunable emission based on the composite of Au nanoparticles and CdSe quantum dots deposited on elastomeric film. *Applied Physics Letters* **2009,** *94*, 071906.

(18) Quach, A. D.; Crivat, G.; Tarr, M. A.; Rosenzweig, Z. Gold Nanoparticle−Quantum Dot−Polystyrene Microspheres as Fluorescence Resonance Energy Transfer Probes for Bioassays. *J. Am. Chem. Soc.* **2011,** *133*, 2028-2030.

(19) Jung, D.-R.; Kim, J.; Nam, S.; Nahm, C.; Choi, H.; Kim, J. I.; Lee, J.; Kim, C.; Park, B. Photoluminescence enhancement in CdS nanoparticles by surface-plasmon resonance. *Applied Physics Letters* **2011,** *99*, 041906.

(20) Zeng, Q.; Zhang, Y.; Liu, X.; Tu, L.; Kong, X.; Zhang, H. Multiple homogeneous immunoassays based on a quantum dots-gold nanorods FRET nanoplatform. *Chem. Comm.* **2012,** *48*, 1781-1783.

(21) Zhang, J.; Ma, N.; Tang, F.; Cui, Q.; He, F.; Li, L. pH- and Glucose-Responsive Core–Shell Hybrid Nanoparticles with Controllable Metal-Enhanced Fluorescence Effects. *ACS Applied Materials & Interfaces* 2012, *4*, 1747-1751.

(22) Tang, F.; Ma, N.; Tong, L.; He, F.; Li, L. Control of Metal-Enhanced Fluorescence with pH- and Thermoresponsive Hybrid Microgels. *Langmuir* **2012,** *28*, 883-888.

(23) Hawker, C. J.; Bosman, A. W.; Harth, E. New Polymer Synthesis by Nitroxide Mediated Living Radical Polymerizations. *Chem. Rev.* **2001,** *101*, 3661-3688.

(24) Matyjaszewski, K.; Xia, J. Atom Transfer Radical Polymerization. *Chem. Rev.* **2001,** *101*, 2921-2990.

(25) Matyjaszewski, K.; Tsarevsky, N. V. Nanostructured functional materials prepared by atom transfer radical polymerization. *Nat Chem* **2009,** *1*, 276-288.

(26) Moad, G.; Rizzardo, E.; Thang, S. H. Living Radical Polymerization by the RAFT Process – A Third Update. *Australian Journal of Chemistry* **2012,** *65*, 985-1076.

(27) Perrier, S.; Takolpuckdee, P. Macromolecular design via reversible addition–fragmentation chain transfer (RAFT)/xanthates (MADIX) polymerization. *Journal of Polymer Science Part A: Polymer Chemistry* **2005,** *43*, 5347-5393.

(28) Favier, A.; Charreyre, M.-T. Experimental Requirements for an Efficient Control of Free-Radical Polymerizations via the Reversible Addition-Fragmentation Chain Transfer (RAFT) Process. *Macromolecular Rapid Communications* **2006,** *27*, 653-692.

(29) Moad, G.; Rizzardo, E.; Thang, S. H. Radical addition–fragmentation chemistry in polymer synthesis. *Polymer* **2008,** *49*, 1079-1131.

(30) Riess, G. Micellization of block copolymers. *Progress in Polymer Science* **2003,** *28*, 1107-1170.

(31) Zhang, L.; Eisenberg, A. Multiple Morphologies of "Crew-Cut" Aggregates of Polystyrene-b-poly(acrylic acid) Block Copolymers. *Science* **1995,** *268*, 1728-1731.

(32) Choucair, A.; Lim Soo, P.; Eisenberg, A. Active Loading and Tunable Release of Doxorubicin from Block Copolymer Vesicles. *Langmuir* **2005,** *21*, 9308-9313.

(33) Wu, J.; Eisenberg, A. Proton Diffusion across Membranes of Vesicles of Poly(styrene-b-acrylic Acid) Diblock Copolymers. *J. Am. Chem. Soc.* **2006,** *128*, 2880-2884.

(34) Wang, X.; Luo, Y.; Li, B.; Zhu, S. Ab Initio Batch Emulsion RAFT Polymerization of Styrene Mediated by Poly(acrylic acid-b-styrene) Trithiocarbonate. *Macromolecules*

2009, *42*, 6414-6421.

(35) He, W.-D.; Sun, X.-L.; Wan, W.-M.; Pan, C.-Y. Multiple Morphologies of PAA-b-PSt Assemblies throughout RAFT Dispersion Polymerization of Styrene with PAA Macro-CTA. *Macromolecules* **2011,** *44*, 3358-3365.

(36) Henglein, A. Small-particle research: physicochemical properties of extremely small colloidal metal and semiconductor particles. *Chem. Rev.* **1989,** *89*, 1861-1873.

(37) Kim, S.; Bawendi, M. G. Oligomeric Ligands for Luminescent and Stable Nanocrystal Quantum Dots. *J. Am. Chem. Soc.* **2003,** *125*, 14652-14653.

(38) Resch-Genger, U.; Grabolle, M.; Cavaliere-Jaricot, S.; Nitschke, R.; Nann, T. Quantum dots versus organic dyes as fluorescent labels. *Nat Meth* **2008,** *5*, 763-775.

(39) Lai, J. T.; Filla, D.; Shea, R. Functional Polymers from Novel Carboxyl-Terminated Trithiocarbonates as Highly Efficient RAFT Agents. *Macromolecules* **2002,** *35*, 6754-6756.

(40) Lessard, B.; Marić, M. Effect of an Acid Protecting Group on the "Livingness" of Poly(acrylic acid-ran-styrene) Random Copolymer Macroinitiators for Nitroxide-Mediated Polymerization of Styrene. *Macromolecules* **2008,** *41*, 7881-7891.

(41) Jackson, C.; Chen, Y.-J.; Mays, J. W. Size exclusion chromatography with multiple detectors: Solution properties of linear chains of varying flexibility in tetrahydrofuran. *Journal of Applied Polymer Science* **1996,** *61*, 865-874.

(42) Dietrich, V. W.; Basch, A. Nachweis von mikrogelen in polyamiden durch lichtstreuung. *Die Angewandte Makromolekulare Chemie* **1974,** *40*, 159-172.

(43) Huglin, M. B.; O'Donohue, S. J.; Radwan, M. A. Refractometric and light scattering parameters at 633 nm for polystyrene solutions. *European Polymer Journal* **1989,** *25*,

543-547.

(44) Marcelo, G.; J. V. Prazeres, T.; Charreyre, M.-T.; Martinho, J. M. G.; Farinha, J. P. S. Thermoresponsive Micelles of Phenanthrene-α-end-labeled Poly(N-decylacrylamide-b-N,N-diethylacrylamide) in Water. *Macromolecules* **2010,** *43*, 501-510.

(45) http://www.amber.ucsf.edu/amber/amber.html; http://www.amber.ucsf.edu/amber/dbase.html; http://pharmacy.man.ac.uk/amber/

(46) MOPAC, Quantum Chemistry Program Exchange (Department of Chemistry, Indiana University, Bloomington, IN).

(47) Allen, M. P.; Tildesley, D. J. *Computer Simulation of Liquids*, Clarendon: Oxford, **1987**.

(48) Wang, C. W.; Moffitt, M. G. Surface-Tunable Photoluminescence from Block Copolymer-Stabilized Cadmium Sulfide Quantum Dots. *Langmuir* **2004,** *20,* 11784-11796.

(49) Marcelo, G.; Tarazona, M. P.; Saiz, E. Solution properties of poly(diallyldimethylammonium chloride) (PDDA). *Polymer* **2005,** *46*, 2584-2594.

(50) Marcelo, G.; Mendicuti, F.; Saiz, E.; Tarazona, M. P. Combination of SEC-MALS and Fluorescence with Molecular Dynamics Simulations for the Analysis of Ionomer Dimensions in Solution. Application to Poly(2-acrylamido-2-methyl-1-propanesulfonic acid-co-styrene). *Macromolecules* **2007,** *40*, 1311-1320.

(51) Burguière, C.; Pascual, S.; Bui, C.; Vairon, J.-P.; Charleux, B.; Davis, K. A.; Matyjaszewski, K.; Bétremieux, I. Block Copolymers of Poly(styrene) and Poly(acrylic acid) of Various Molar Masses, Topologies, and Compositions Prepared via Controlled/Living Radical Polymerization. Application as Stabilizers in Emulsion

Polymerization. *Macromolecules* **2001,** *34*, 4439-4450.

(52) Rowe, M. D.; Hammer, B. A. G.; Boyes, S. G. Synthesis of Surface-Initiated Stimuli-Responsive Diblock Copolymer Brushes Utilizing a Combination of ATRP and RAFT Polymerization Techniques. *Macromolecules* **2008,** *41*, 4147-4157.

(53) Spatorico, A. L.; Coulter, B. Molecular weight determinations by gel-permeation chromatography and viscometry. *Journal of Polymer Science: Polymer Physics Edition* **1973,** *11*, 1139-1150.

(54) Wagner, H. L. The Mark–Houwink–Sakurada Equation for the Viscosity of Atactic Polystyrene. *Journal of Physical and Chemical Reference Data* **1985,** *14*, 1101-1106.

(55) Tsimpris, C. W.; Suryanarayanan, B.; Mayhan, K. G. Intrinsic viscosity—molecular weight relationship for polystyrene in N,N-dimethylformamide. *Journal of Polymer Science Part A-2: Polymer Physics* **1972,** *10*, 1837-1839.

(56) Mabire, F.; Audebert, R.; Quivoron, C. Flocculation properties of some water-soluble cationic copolymers toward silica suspensions: A semiquantitative interpretation of the role of molecular weight and cationicity through a “patchwork” model. *Journal of Colloid and Interface Science* **1984,** *97*, 120-136.

(57) Burchard, W. *Static and dynamic light scattering approaches to structure determination of biopolymers. In Laser Light Scattering in Biochemistry*. (Harding, S. E.; Sattelle, D. B.; Bloomfield, V. A. editors). Royal Society of Chemistry: Cambridge, **1992**.

Chapter 3 - Self-Assembly of Polymer Encapsulated Quantum Dots and Gold Nanoparticles

3.1 Introduction

Self-assembly is the autonomous organization of individual components into patterns/structures without external intervention.[1] Control over the self-assembly of a given system is a desirable process in chemical systems across all disciplines of research as a means of creating reversible, higher order structures with minimal experimental input.[8,10,12,13,66–71] Block copolymers have been designed to self-assemble into a variety of morphologies, dictated by their composition and that of the surrounding solvent environment.[37,72–75] In tandem with self-assembly processes, a core research goal in nanomaterial research lies the incorporation of multiple functionalities within a single structure. These two fields of research are nicely bridged with through the use of block copolymer micelles as templates for the growth and stabilization of metal or semiconductor nanoparticles. These nanostructures are suitable as building blocks for subsequent self-assembly steps, mediated by their polymer brushes.

Of particular interest as building blocks is the case in which a photoluminescent quantum dot (QD) is encapsulated within a polymeric micelle functionalized with thiol terminal groups on coronal chains. Such building blocks have been demonstrated to exhibit controlled assemblies with gold nanoparticles, employing the polymer brush to mediate interparticle spacing.[27] Various assemblies comprised of a semi-conducting or metallic nanoparticle paired with surface plasmon resonance (SPR) exhibiting nanoparticles have been investigated in the literature. As a result of strong distance dependence on metal-semiconductor interactions, control over their spatial positioning is critical to their function.[5,76,77] These composite structures have been shown to exhibit numerous

applications across fields ranging from sensing[78–81] and photonics[26,82,83]. In the pursuit of adding functionality through self-assembly, the subsequent self-assembly of block copolymer encapsulated nanoparticle building blocks have been shown to exhibit interesting photonic properties, such as stop-band.[25,26]

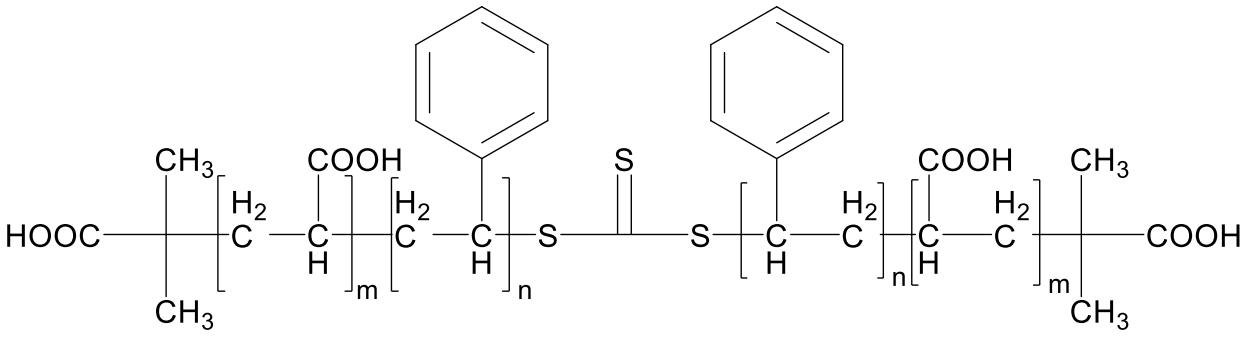

Figure 3-1. General chemical schematic of the RAFT copolymer in use for this chapter. The subscripts 'm' and 'n' correspond to the number of repeat units.

Our groups has previously investigated the use of symmetric amphiphilic tetrablock copolymers of poly(acrylic acid–*b*-styrene-*b*-styrene-*b*-acrylic acid), with a central trithiocarbonate (TTC) group (see Figure 3-1) to prepare hierarchical QD-gold nanoparticle assemblies which demonstrated surface-plasmon enhanced fluorescence[27]. In this work, the tetrablock copolmyer was determined to generate suitable building blocks for the formation of cadmium sulfide quantum dots within the micellar core. Subsequently, upon aminolysis of the central TTC group and introduction of gold nanoparticles, superstructures with polymer-mediated interparticle spacing and exhibiting gold-enhanced photoluminescence (PL) were created.

This chapter will seek to expand on previous work explored in our group,[27] through the study of a new polymer with an increased PS brush length. This will serve to demonstrate that the methodology employed to measure emission amplification is valid

with a different polymer; and how altered interparticle spacing brought about by increased brush length will influence the emission amplification. Understanding these features are key to establishing these systems as a general building block template from which a wide array nanoparticle assemblies may be prepared. This work will be followed by an initial investigation of QDCM assembly with the RAFT copolymer in the presence of AuNPs. Characterization will entail investigation of photoluminescence measurements (PL), absorbance, transmission electron microscopy (TEM), and dynamic light scattering (DLS) in order to obtain a detailed understanding of the particles at the various stages of assembly. QDCM assembly utilizing the RAFT-QDMs "building blocks" seeks to add to the tool kit of methodologies for self-assembly of polymer mediated self-assembly of nanoparticles.

3.2 Experimental

3.2.1. Preparation of Block Copolymer Micelle Encapsulated CdS Quantum Dots.

Polymer encapsulated cadmium sulfide quantum dots begin by the dissolution of RAFT copolymer to 0.5 wt % in 1,4-dioxane followed by overnight stirring to ensure homogenous dispersal. To this solution a methanolic 0.25M $CdAc_2 \cdot 2H_2O$ solution was added in a 1:1 molar ratio of Cd^{2+} ions to COOH groups of the polymer and allowed to stir for five hours. Sample quickly exhibits Tyndall scattering following addition of $CdAc_2 \cdot 2H_2O$ solution, indicative of the formation of aggregates. A 1.9M solution of Na_2S was created in a 50/50 (v/v) mixture of methanol and slightly acidic deionized water (pH = 5.46) and added to the micellar solution in either 1:1, 1:0.8 or 1:0.4 molar ratio of COOH groups to S^{2-} ions and allowed to stir overnight in the dark. From this point onward, the samples were kept in the dark as the CdS quantum dots are prone to photo-oxidation.

3.2.2. Synthesis of Gold Nanoparticles.

Gold nanoparticles are created through a slightly modified Brust synthesis.[84] Chloroauric acid ($HAuCl_4 \cdot 3H_2O$, 30 mM, 30 mL) was dissolved in deionized water and allowed to stir for 30 minutes until fully dissolved. To this solution an 80 mL, 50 mM solution of tetraoctylammonium bromide (TOABr) in toluene was added to the gold solution with vigorous stirring. Phase separation occurs between the aqueous and organic layers. The sample was vigorously stirred until all gold was transferred to the organic layer (~30 minutes), visible as the aqueous layer becomes clear and colourless while organic layer becomes a deep orange/red. To this solution the surfactant 1-dodecanethiol is added in a ~1 molar ratio to gold (170 mg) and allowed to stir for 30 minutes until fully dispersed. Finally, to this solution a freshly prepared, chilled 0.4 M (25 mL) solution of $NaBH_4$ in deionized water is added to gold in a fast, dropwise manner. The sample is then allowed to stir overnight in order to ensure the reduction of the gold salt progresses to completion. The sample is then decanted to remove the aqueous layer followed by reducing the volume of solvent present using rotary evaporation. It is key that the sample is not allowed to go to dryness at this stage, as bulk gold will plate out on the vessel walls. Under the above sample conditions the volume is usually reduced to a volume of ~15-20 mL. Following this, several wash steps are performed twice with anhydrous ethanol followed by another wash with acetone. The samples are then allowed to dry under vacuum at room temperature overnight whereupon they are characterized by TEM and absorption measurements.

3.2.3. Preparation of Gold Nanoparticle-Conjugated Quantum-Dot Micelles (QDM-AuNPs).

Creation of dispersions comprised of QDMs with variable amounts of AuNPs were prepared in a 1:1 mixture of dioxane:toluene (v:v). Dilute solutions of stock QDM solution were prepared in a ~10x dilution, e.g. 1.5 mL of stock in 15 mL of dioxane. A designated quantity of AuNPs were added to 2 mL of this dilute solution of QDMs to which pure toluene was added to bring the final solution volume to 4 mL. This dilution process ensured that all samples were of identical composition with the exception of the variable amounts AuNPs. Following this preparation, a 10x molar excess of 1-hexylamine per TTC group was added, transforming the TTC group into thiol groups thereby promoting binding to the AuNPs. Samples were stirred vigorously overnight at 25 °C in the dark to ensure completion of the reaction. The samples are created with different molar ratios of thiol groups to gold atoms, termed R_{Au}, which corresponds to different ratios of CdS QDs to AuNPs, termed R_{GNP}. Samples were prepared with values of R_{Au} = 0.1, 0.2, 0.3, 0.4, 0.5, 1.5 and 3.0, which correspond to R_{GNP} = 0.002, 0.004, 0.006, 0.008, 0.01, 0.03 and 0.06.

Below is a sample calculation for converting R_{Au} to R_{GNP}:

$$R_{GNP} = \frac{N_{SH} \times R_{Au}}{N_{Au}} \tag{3.1}$$

Where N_{SH} is the number of thiol groups per micelle, N_{Au} is the number of gold atoms per nanoparticle. Calculation of N_{SH} and N_{Au} can be found in Ref. 73, as well as in section 3.4.2. Standard deviations were calculated from the measurement of triplicate QDM-AuNP solutions prepared from the same stock solutions.

3.2.4. Preparation of QDM-AuNP Compound Micelles (QD-AuCMs).

Two primary methodologies were tested for the formation of QD-AuCMs; Method 1: QD-AuCM assembly beginning at the concentrations resulting from the above synthesis of QD-AuNPs and Method 2: beginning QD-AuCM formation without dilution of samples in dioxane and toluene. In method 1, QD-AuCM assembly begins at a concentration of solid material of ~0.002 wt%, the concentration resulting from QDM-AuNP formation, note for these studies $R_{GNP} = 0.056$ was used. To the stock QDM-AuNP solution a solution of 0.002 wt% $PS_{403.3}$-*b*-$PAA_{62.4}$ (subscripts denote repeat units, from M_n) was added at three different blending ratios. Specifically, these blends correspond to $f_{QDM\text{-}AuNP} = 0.15, 0.25, 0.35$ where $f_{QDM\text{-}AuNP}$ represents the weight of QDM-AuNP solution over the total mass of the two solutions. To these mixtures, deionized water was added under vigorous stirring at a rate of ~5 wt%·min^{-1} up to a final concentration of 25 wt%. Samples were then dialyzed against deionized water in 1 MDa nominal pore size, regenerated cellulose dialysis tubing for 24 hours, replacing the deionized water after 2, 4, 8, 12 hours. Samples were then weighed in order to determine the new sample concentration. In method 2, the QD-AuCM assembly begins at three different initial concentrations: 0.1, 0.25 and 0.5 wt%. In contrast to method 1, these samples are not diluted with dioxane and toluene, rather the AuNPs are added in the proper ratio to the stock QDM solutions ($R_{GNP} = 0.056$). Subsequent steps in method 2 are the same as those listed in method 1. The blending ratios for method 2 were as follows: $f_{QDM\text{-}AuNP}$ =0, 0.05, 0.1 and 0.15 were explored. Water addition remained at ~ 5 wt%·min^{-1} up to ~25 wt%. The dialysis process remained unchanged. Samples were subsequently characterized by DLS, PL and absorbance measurements.

3.3. Instrumentation

3.3.1. Dynamic Light Scattering.

Dynamic light scattering measurements were performed on a Brookhaven Instruments Co. BI-200SM research goniometer system, with a Brookhaven Instruments Co. Mini-L30 30 mW red (636 nm) compact diode laser. Measurements were carried out in cylindrical glass cells in order to simplify the corrections needed for refractive index variations. The circular vat cell contains decalin to minimize light refraction. The measurements were analyzed using the analysis package CONTIN (Brookhaven) in tandem with a cumulant fit to determine hydrodynamic diameter (D_h) and particle size distribution. In order to minimize dust from the solvent, this was filtered with 2 x 0.22 μm pore size syringe filters.

3.3.2. Photophysical Characterization.

Absorbance measurements were performed on a Perkin Elmer Lambda 1050 UV/Vis/NIR spectrophotometer with a wideband 3 detector module. Fluorescence spectroscopy was performed on an Edinburgh Instruments FLS920 spectrometer with a 450W xenon arc lamp and a Hamatsu R5509 photomultiplier tub (PMT) detector. Slit widths were adjusted to achieve a 5 nm resolution with a dwell time of 0.5 s.

3.3.3. Transmission Electron Microscopy (TEM).

Transmission electron micrographs were obtained on a JEOL JEM-1400 transmission electron microscope with a LaB_6 filament, equipped with a GatanOrius SC100 camera, with an accelerator voltage of 80 kV. TEM grids for QDM and QD-AuCM assemblies were prepared first by cooling an (Al) block in liquid nitrogen, a 300-mesh carbon coated Cu TEM grid was placed on the Al block and 10 μL of QDM or QD-AuCM solution was dropped onto the grid and quickly immersed in liquid ethane. Solutions were then placed under vacuum until dry. Sublimation is unlikely in the case of the QDM assemblies due to

insufficient vacuum, rather evaporation probably occurred. For AuNP samples, a 10 µL sample of AuNP solution was deposited on 300-mesh carbon coated Cu TEM grids and allowed to rest for 30 s before excess solvent was wicked away.

3.4. Calculations

3.4.1. Determination of CdS Core Diameter from Band-Edge Analysis.

In order to determine the size of the CdS core, an absorbance measurement was collected. From this measurement, the wavelength for the band edge threshold λ_{thresh} was determined from extrapolation to the baseline (see Figure 3-2). λ_{thresh} will correspond to the onset of the band edge absorption.

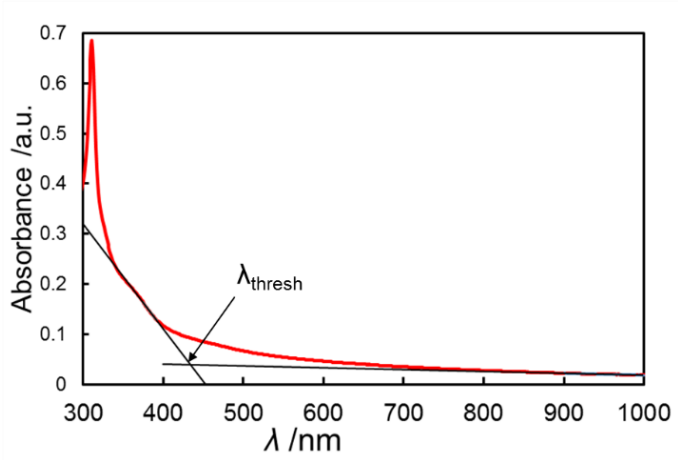

Figure 3-2. Absorbance spectrum of RAFT-CdS QDM with arrow indicating the extrapolated threshold wavelength for input in equation 3.2.

From λ_{thresh} the median core diameter (D_{thresh}) can be determined from the following equation:

$$D_{thresh} = \frac{1}{(0.1338 - 0.0002345 * \lambda_{thresh})} \quad (3.2)$$

This provides an average core diameter in Angstroms, which can then be converted to nanometers.[27,85]

3.4.2. Determination of the Number of Thiol Groups per Micelle.

In order to calculate an R_{GNP} value, the number of polymer chains, and therefore the resultant number of thiol groups, must be calculated. Beginning with D_{thresh} from above, the volume of the CdS core (V_{CdS}) can be calculated as follows:

$$V_{CdS} = \frac{4\pi r_{thresh}^3}{3} \tag{3.3}$$

where r_{thresh} is half of D_{thresh}, typically volume is calculated in centimeters (1 cm = $1x10^7$ nm) in order to determine the mass of the CdS core:

$$M_{CdS} = V_{CdS} \times \rho_{CdS} \tag{3.4}$$

where M_{CdS} is the mass of the CdS core, and ρ_{CdS} is the density of CdS (4.82 $g \cdot cm^{-3}$). From the M_{CdS}, we can determine the number of cadmium ions per micelle by:

$$N_{Cd^{2+}} = \frac{M_{CdS}}{MW_{CdS}} \times N_A \tag{3.5}$$

Where N_{Cd2+} is the number of Cd^{2+} ions in the micelle, MW_{CdS} is the molecular weight of CdS (144.48 $g \cdot mol^{-1}$) and N_A is Avogadaro's number. Operating under the assumption that there are 2 PAA (COO^-) ions for each cadmium ion, each micelle is comprise of N_{Cd2+} x 2 PAA groups. Each polymer chain is comprised of 34 PAA units, and each chain will be split into 2 thiol groups, this results in the number of thiol chains per micelle, N_{SH} given by:

$$N_{SH} = \left(\frac{N_{Cd^{2+}} \times 2}{34}\right) \times 2 \tag{3.6}$$

3.4.3. Determination of the Number of Gold Atoms per Nanoparticle. The calculation for determination of the number of gold atoms per nanoparticle, N_{Au}, the average mass of individual NPs can be determined based on the diameter of the NP determined from TEM measurements. Following the process laid out in section 3.4.2, M_{Au}

can be determined using the volume of a sphere, the density of Au (ρ_{Au}= 19.7 g·mol^{-1}). The number of gold atoms per nanoparticle, N_{Au}, is given by:

$$N_{Au} = \frac{M_{Au}}{MW_{Au}} \times N_A \tag{3.7}$$

Where MW_{Au} is the molecular weight of gold (196.97 g·mol^{-1}).

3.4.4. Determination of Emission Amplification. In order to determine emission amplification results for a given QDM-AuNP assembly, absorbance measurements of the QDM and AuNP were collected alongside the emission results. To correct for auto-absorption effects for the assemblies, equation 3.9 was applied:

$$FI_{corr} = FI \times \left(\frac{Abs_{CdS\ \lambda ex} + Abs_{AuNP\ \lambda ex} + Abs_{AuNP\ \lambda em}}{Abs_{CdS\ \lambda ex}}\right) \tag{3.9}$$

where FI is the fluorescence intensity at a given wavelength, FI_{corr} is the corrected fluorescence intensity, $Abs_{\lambda ex}$ and $Abs_{\lambda em}$ correspond to the absorbance of the samples (CdS or AuNPs) at the excitation and emission wavelengths respectively. This correction factor is applied at each emission wavelength. Subsequently, FI_{corr} is compared to the QDM stock solution to determine the emission amplification (EA):

$$EA = \left.\sum_{\lambda_{em,i}}^{\lambda_{em,f}} \left(\frac{FI_{corr}}{FI_{QDM}}\right)\right/ N_{\lambda_{em}} \tag{3.10}$$

where the summation refers to the range from the initial emission wavelength to the final emission wavelength (e.g. for a 350 nm excitation $\lambda_{em,i}$ = 370 nm, $\lambda_{em,f}$ = 680 nm), FI_{corr} is the same as that determined in eq. 3.9, FI_{QDM} corresponds to the fluorescence intensity of the QDM stock solution, $N_{\lambda em}$ is the number of emission wavelengths in the specific range.

3.4. Results and Discussion

3.4.1. Formation of QDM-AuNP Assemblies and Emission Amplification

Initial investigations into the assembly process by another student in the Moffitt group began with a RAFT copolymer with a PS block length of ~39 repeat units and a PAA block length of ~18 repeat units.[27] Follow up replicate experiments were attempted using the experimental conditions established previously in our group,[27] and detailed in sections 3.2 and 3.3. During these follow up experiments, the sample was observed to have no EA despite virtually identical synthetic conditions to those previously investigated. It was during the course of these experiments that problems with polymer solubility was noted, specifically a marked increase in sample turbidity following addition of cadmium acetate. At this stage of the assembly process a clear, colourless solution exhibiting Tyndall scattering (indicative of the formation of micelles) is expected, instead a highly turbid, milky solution was observed. As a result of these solubility problems, a determination was made to obtain a new sample of RAFT copolymer. This new polymer was synthesized by our collaborator (see Ch. 2 for details) under similar conditions, which resulted in a polymer with approximately twice the length of PS and ~17 repeat units of PAA. The additional length of PS will result in an increased brush length upon micellar assembly, thereby increasing the spacing between the CdS core and the AuNP. As such, a series of experiments were performed to replicate the data previously obtained with the shorter PS block and determine whether emission amplification was still observed with the new polymer.[27]

Figure 3-3A demonstrates a typical series of emission spectra for RAFT-CdS cores as a function of increasing excitation wavelength excitation. Upon assembly of the QDMs with AuNPs it was observed that some of the samples exhibited a blue shift of the emission peak, as well as the presence of 2-3 additional peaks (Figure 3-3B). Additionally, the

abnormal features were not observed in samples absent of AuNPs, indicating the AuNPs are likely playing a role in the generation of these peaks. In order to confirm these peaks were not simply a result of experimental error, a repeat series of 10 sample preparations at R_{GNP} = 0.056 were analyzed. From these experiments it was determined that 4/10 samples exhibited the blue shift and additional peaks. A rate of occurrence this high indicates that this is a real feature of the sample and not simply a result of instrumental or experimental error. Paired with emission data, excitation scans collected at 520 nm (see Figure 3-4) exhibit an additional shoulder feature along the absorption edge (~400 nm) only for the samples exhibiting the abnormal peak structures. The cause of the shoulder is however uncertain as subsequent preparations with a new preparation of gold nanoparticles has not exhibited this phenomenon (see Figure 3-5, Figure 3-6). A possible explanation may include the formation of "hot-spots", multiple AuNPs coupling to a single QDM core altering the absorption and de-excitation pathways, and the peak shape of the QDM cores.[86,87]

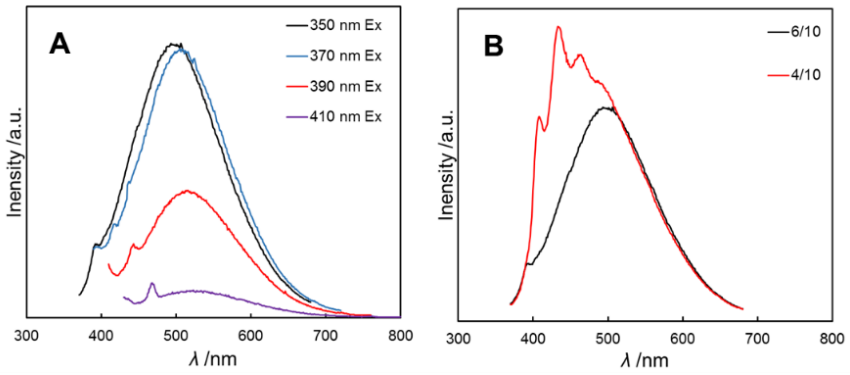

Figure 3-3. A) Example of CdS core emission at four different excitation wavelengths. B) Example of deviation between emission spectra from 350 nm excitation, listed based on their frequency over ten replicate samples.

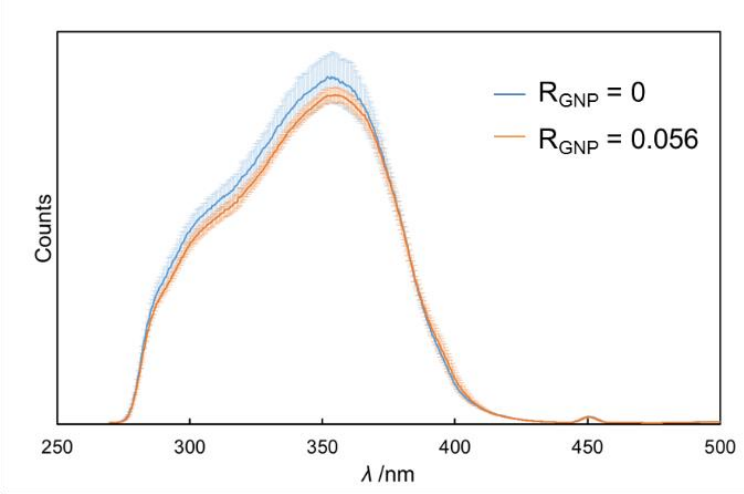

Figure 3-4. Average excitation scans collected at 520 nm emission shown with error bars of samples in the absence (R_{GNP} = 0) of and presence (R_{GNP} = 0.056) of gold nanoparticles.

Successive studies of the emission amplification process resulted in several successful preparations, with no indication of blue shifting or additional emission peaks (see Figure 3-5 and Figure 3-6). Two of these samples are included for discussion in addition to a background scan in which the TTC group of the RAFT copolymer (scheme 3.1) was not cleaved to form thiol terminal groups. These two emission amplification experiments were performed using different pairs of CdS and AuNPs. The first of these experiments, referred to as the purple series, has the relevant optical properties and size information detailed in Figure 3-5; while the second series, referred to as the black series, is detailed in figure Figure 3-6. Note that the very small features along the main emission peaks are simply noise.

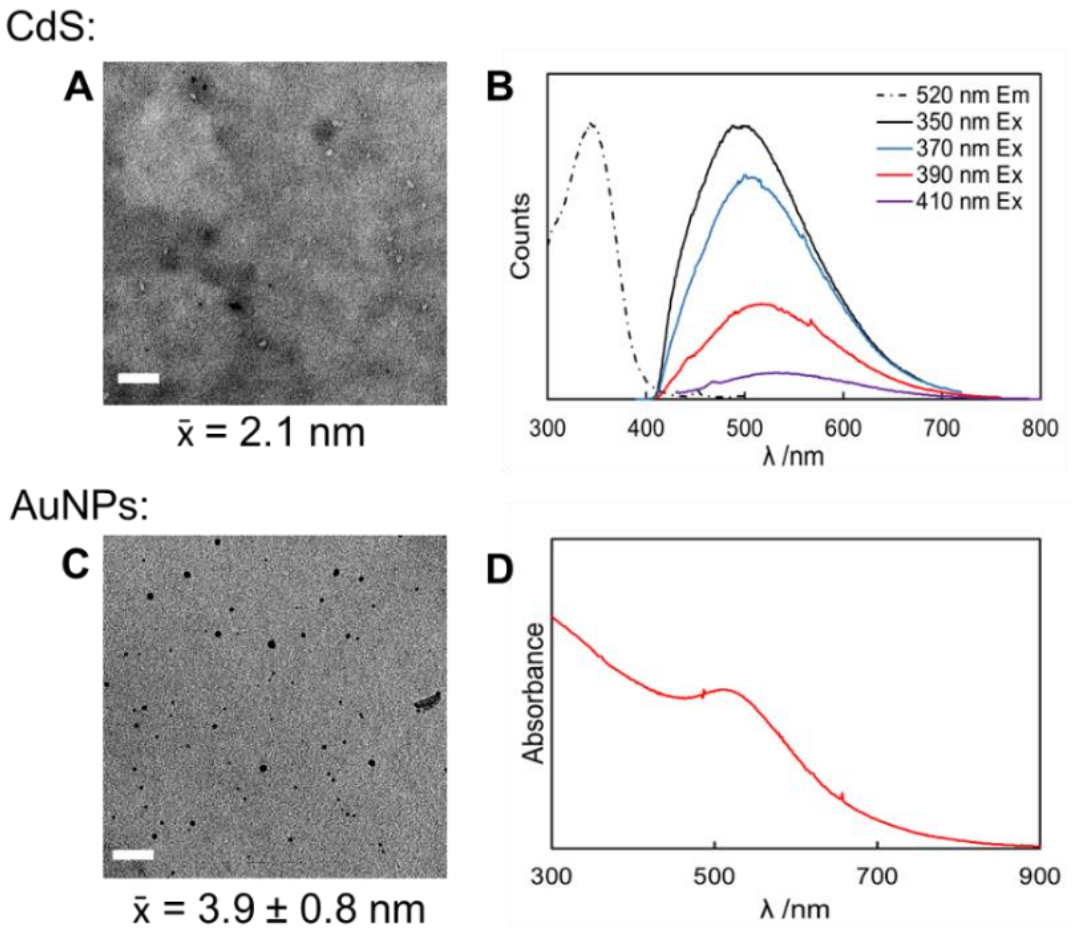

Figure 3-5. Representative TEM image for CdS cores of the purple run of Figure 3-7(A), representative emission and excitation spectra for Figure 3-7 purple run (B). Figures C and D correspond to TEM images and absorption spectra of the AuNPs used for the black run. Scale bars correspond to 20 nm.

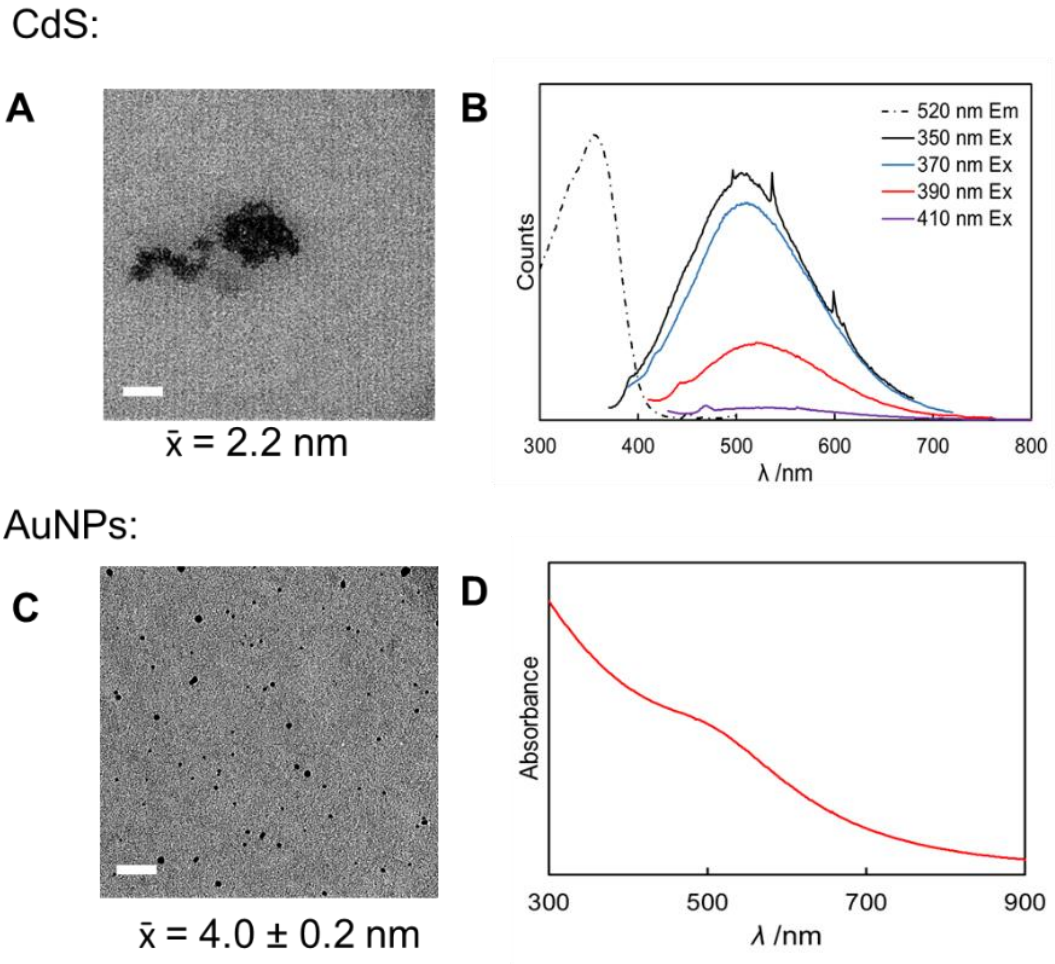

Figure 3-6. Representative TEM image for CdS cores of the black run of Figure 3-7(A), representative emission and excitation spectra for Figure 3-7 black run (B). Figures C and D correspond to TEM images and absorption spectra of the AuNPs used for the black run. Scale bars correspond to 20 nm.

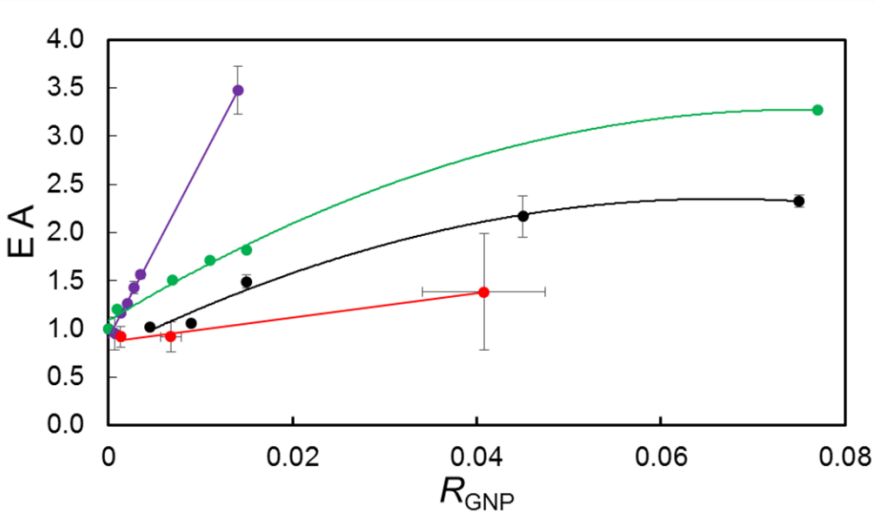

Figure 3-7. Emission amplification as a function of RGNP at a 350 nm excitation wavelength. The four spectra correspond to the original data for the project with the original polymer sample (green), two separate sample runs with the new polymer sample (purple, black) and a background of the sample with no addition of hexylamine (red). Error bars correspond to standard deviations.

Figure 3-7 demonstrates the emission amplification plot as a function of R_{GNP} for samples excited at 350 nm. The method of EA determination is detail in section 3.3. The background measurements (red series) demonstrate that if the TTC group of the RAFT copolymer is not cleaved, there is virtually no indication of emission amplification. The exception to this is one of the triplicate measurements for the R_{GNP} = 0.04 sample, which did indicate the presence of emission amplification. As this is a single data point, it may very well be experimental error, further replicates will be required to confirm. The tentative conclusion that can be drawn from this result is that the cleavage of the TTC group and the subsequent binding of the AuNP to the QDM corona are required for EA to occur. The green series represents the initial work on EA characterization for these samples investigated in our group.[27] It is the EA of the green series that the current samples, the purple and black series, are attempting to replicate. It is clear from their traces that EA is

certainly visible in both of these samples; however, they have drastically different EA responses. At first glance, the differences between the two sample sets (Figure 3-5 vs. Figure 3-6) is not immediately obvious from their physical characteristics; both share primary emission peak centers at ~520 nm, band edge analysis of the cores (see section 3.3 for details on this calculation) indicate CdS core sizes of ~2 nm, TEM data indicates both AuNP samples have mean core diameters, $\bar{x}$, of ~4 nm. The only major difference associated between the two samples is during the formation of the CdS core, specifically for the purple run (Figure 3-5A, B) the CdS core was created through the addition of Na_2S in a 1:1 molar ratio to COO^{2-} groups; whereas the black run (Figure 3-6 A,B) had a 1:0.4 S^{2+}:COO^{2-} molar ratio. This difference, apart from altering the final EA outcome (Figure 3-7) appears to have limited effect on the emission profile of the CdS cores. If a size differential was observed, this would be reflected in the excitation and absorption scans (larger particles would be red shifted), if surface passivation was observed there would be a decrease in trap state emission intensity and a growth in band edge emission. One might also expect to observe an alteration of the micellar structure as the sample with a higher Na_2S ratio will be replacing Cd^{2+} ions, which act as cross-linkers of the PAA core forming blocks, with Na^{+} ions which are unable to cross-link the PAA blocks. This effect is not observed though as it would result in micellar break up followed by precipitation of the insoluble CdS cores within the organic solvent environment. If experimental errors were the cause of the sample variation, one would expect larger standard deviations for the data sets. This is expected as the error would be propagated through all the calculations detailed in section 3.3, resulting in a significant deviation. Despite their different trends, both the purple and black series of Figure 3-7 clearly indicate that despite the increased PS block

length relative to initial investigations performed previously within our lab (green run, Figure 3-7), EA is observed with this system.

3.4.2. Self-Assembly of QD-AuCMs

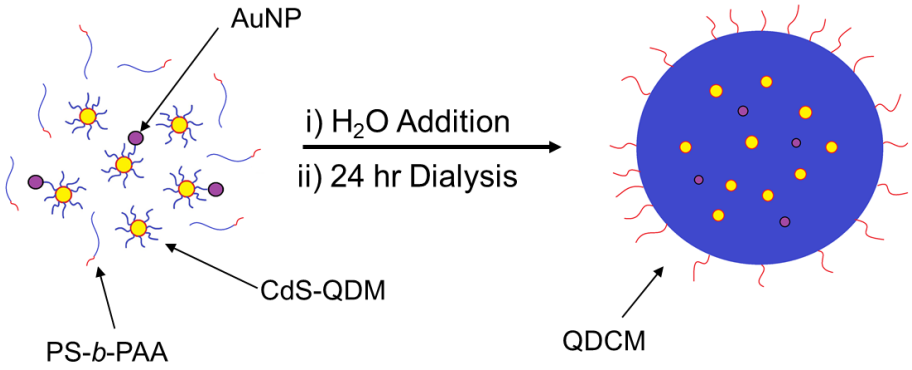

Figure 3-8. A diagram showing the process of QDCM formation through the addition of single chains, water and dialysis.

Following determination that emission amplification is viable with an increased PS block length, it becomes desirable to determine if further self-assembly into quantum dot compound micelels (QDCMs) is viable for the QDM-AuNP assemblies. To this end, two methods of sample preparation were investigated: the first method involved the use of previously prepared QDM-AuNPs followed by assembly into QDCMs following the process outlined by Figure 3-8. Adaptation of the method previously explored in our group[25] to this technique proves unfeasible however for two primary reasons. First, the concentration of materials is significantly lower than those previously explored, ~0.5 wt% in the original against ~0.002 wt% in the QDM-AuNP prep. This does not inherently cause problems for the formation of QDCMs however it results in samples of such low concentration that they are too dilute for detection via fluorescence and light scattering measurements following dialysis. The second problem associated with the use of QDM-AuNP samples is a result of the 50/50 composition of dioxane and toluene. At low blending

ratios ($f_{QDM\text{-}AuNP}$), the solvent composition of the QDM-AuNP system is negligible relative to the significantly higher volume of dioxane solubilized single chains; however, above ~$f_{QDM\text{-}AuNP}$ = 0.15 the increased percentage of toluene in the final solution results in phase separation upon dropwise addition of water. As such it is impossible to form the QDCM assemblies in a meaningful quantity under typical EA assembly parameters (see section 3.2.3.) without either: concentrating the sample which potentially resulting in aggregation of the particles, or dialysis first in dioxane to remove the toluene component followed by water addition and dialysis.

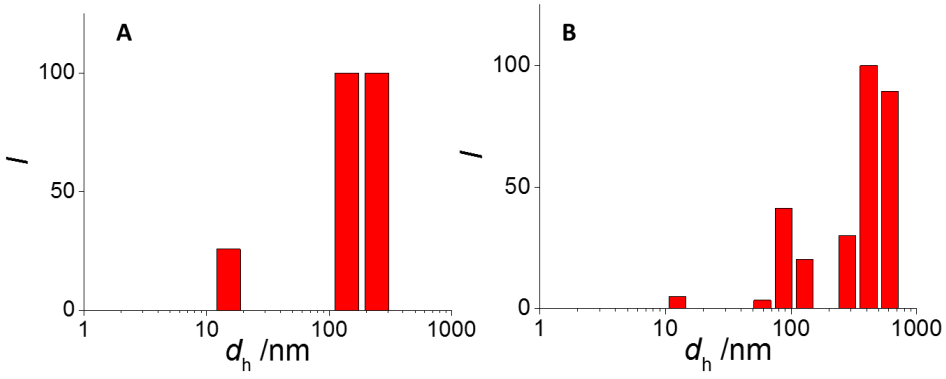

Figure 3-9. Representative CONTIN distribution of QDM stock solution (A) and QDM solution following addition of AuNPs (B), *I* corresponds to intensity averaged frequency.

Neither of these processes are ideal and as such an alternative preparation method must be investigated. To this end, the second preparation method involves an identical prep of the CdS cores and AuNPs, however in lieu of performing a dilution step for the assembly process and EA calculations, the gold nanoparticles are added to the concentrated QDM solution (0.1, 0.25, or 0.5 wt%) with hexylamine and allowed to stir at this stage. To these solutions a matching concentration solution of single chains (*i.e.* 0.1, 0.25, 0.5 wt%) was added to create 4 separate blending ratios: $f_{QDM\text{-}AuNP}$ = 0, 0.05, 0.1 and 0.15. The $f_{QDM\text{-}AuNP}$ = 0 sample serves as a baseline for comparison to samples prepared in the presence of

QDMs. As these samples are almost entirely in dioxane, dropwise water addition does not invoke phase separation.

Dynamic light scattering measurements were performed on the concentrated QDM-AuNP solutions (Figure 3-9A and B) in order to determine the particle size and distribution in solution at the each stage of assembly. In Figure 3-9 A, the DLS results for the QDM stock solution is presented. The single peak at ~20 nm is representative of individual CdS-QDMs, the two larger peaks may indicate dust or some aggregation of QDMs. Note that due to the nature of intensity averaged DLS measurements, larger particulates in the solution will be highlighted. The DLS results of Figure 3-9 B correspond to the QDM-AuNP solutions. It is visible in Figure 3-9 B that there are large aggregates present in solution, this is likely a result of aggregation due to the poor solubility of the dodecanethiol stabilized gold nanoparticles in dioxane in addition to the assembly of AuNPs to the QDM corona. Following assembly of the QDM-AuNPs with the single chains and the subsequent dialysis, CONTIN analysis of DLS measurements as a function of initial solids concentration (Figure 3-10) and blending ration (Figure 3-11) were obtained. Both parameter show a large increase in average particle diameter, as expected from the assembly process.

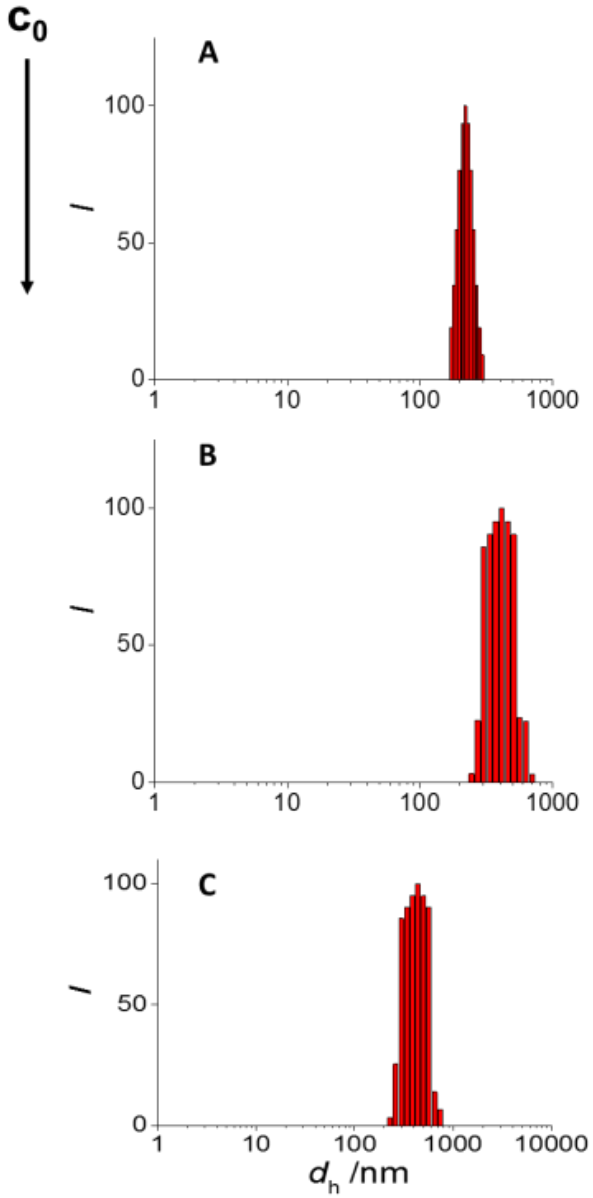

Figure 3-10. Representative intensity averaged CONTIN distribution of particles at a blending ratio of 0.15, with increasing concentration from 0.1 – 0.5 wt% from A-C.

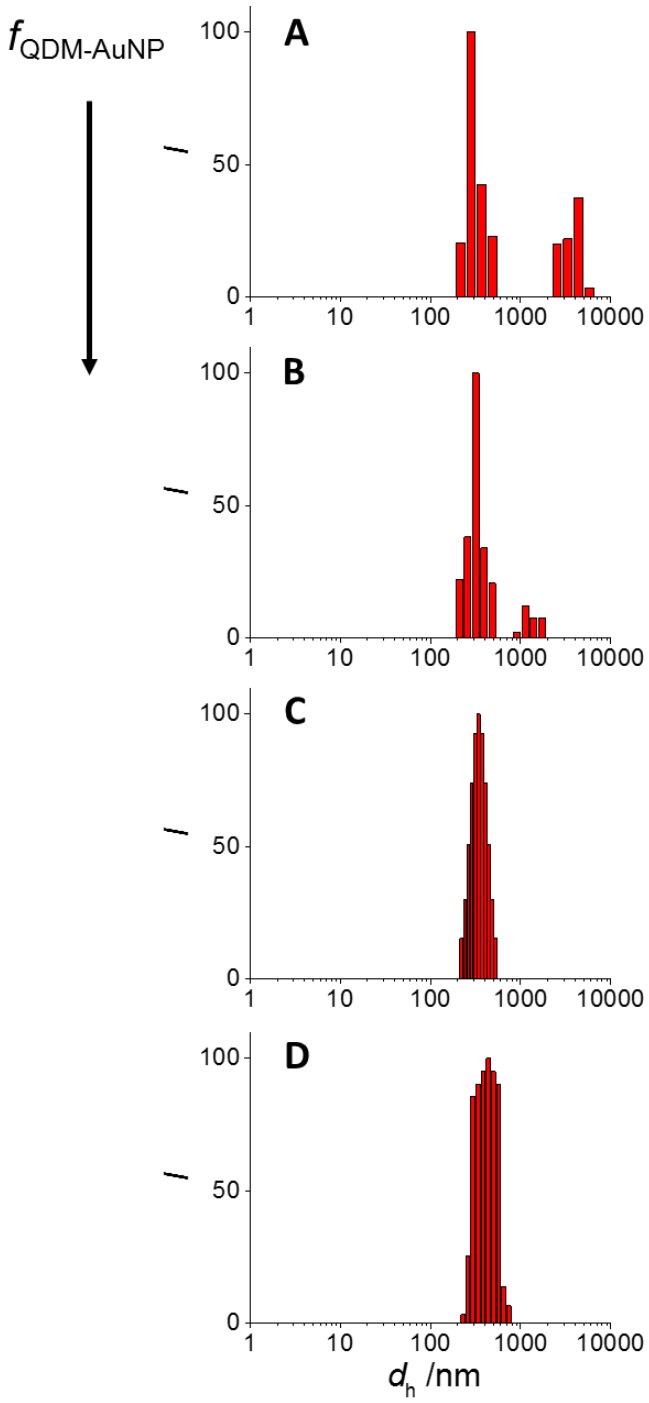

Figure 3-11. Representative intensity averaged CONTIN distribution of particles from an initial po1ymer concentration of 0.5 wt%. A-D correspond to increasing blending ratios, corresponding to $f_{QDM-AuNP}$ = 0, 0.05, 0.1, and 0.15 respectively.

Table 3-1. Hydrodynamic diameter from DLS measurements as a function of initial concentration and blending ratio.

C_0	Blending Ratios			
	$f = 0$ D_h / nm	$f = 0.05$ D_h / nm	$f = 0.1$ D_h / nm	$f = 0.15$ D_h / nm
0.1 wt%	269 ± 1	314 ± 8	265.5 ± 1	226 ± 9
0.25 wt%	413 ± 16	295 ± 6	363 ± 13	376 ± 20
0.5 wt%	534 ± 19	356 ± 5	376 ± 12	397 ± 30

Light scattering result show a clear trend of increasing QDCM size with increasing initial solid concentration, moving from 269 to 534 nm mean diameter for $f_{\text{QDM-AuNP}} = 0$ based on Cumulant analysis (Table 3.1). This trend is supported by CONTIN results at constant concentrations (Figure B3.1) and at constant blending ratios (Figures B3.2, B3.3, B3.4). In tandem with an increase in mean diameter there is an observed increase in polydispersity, reflective of the non-equilibrium nature of phase coarsening during spinodal decomposition of the mixed solvent system.[25,26] This effect highlights the fact that the assembly process is kinetic in nature. The implications of this process is that as concentration of polymer increases, and the subsequent lowering and broadening of CWC, longer particle growth times are promoted.[26] As a means of size control however the use of concentration is flawed as polydisperse samples will result in poor sample quality for subsequent applications.

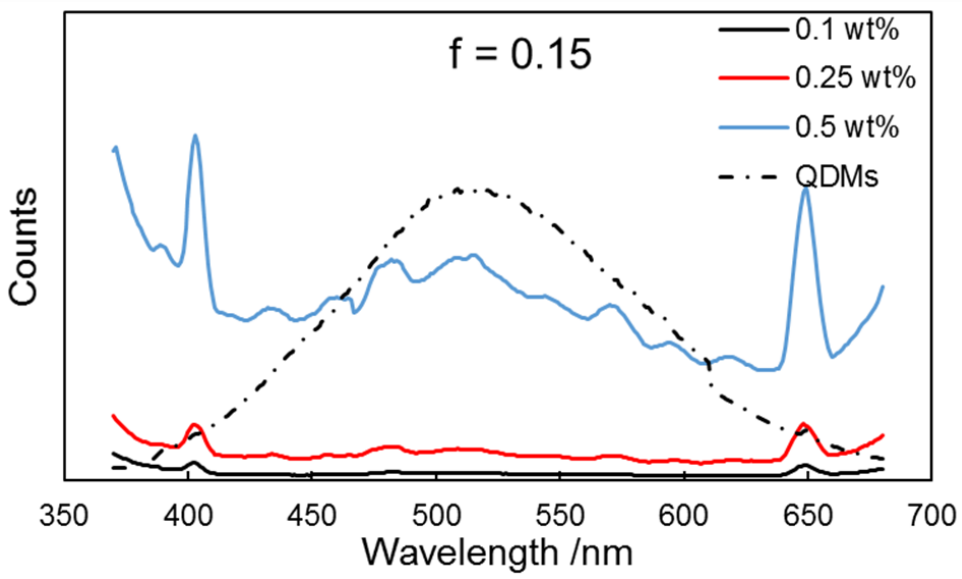

Figure 3-12. Example fluorescence scans at 350 nm excitation for a 0.15 blending ratio. Initial solid concentrations are compared against base QDM mixture (dashed black line).

Fluorescence measurements (Figure 3-12, Figure B3.5) show an increased emission response as a function of increasing blending fraction and increasing concentration. This trend stands to reason as both trends correspond directly to increased quantities of CdS quantum dots. It should be noted the drastic increase in scattering relative to the QDM reference (Figure 3-12, black line). The photoluminescent properties of these assemblies even at $f_{\text{QDM-AuNP}} = 0.15$ is difficult to distinguish from the baseline. As such, these samples lend strong support for future investigation into higher blending fractions.

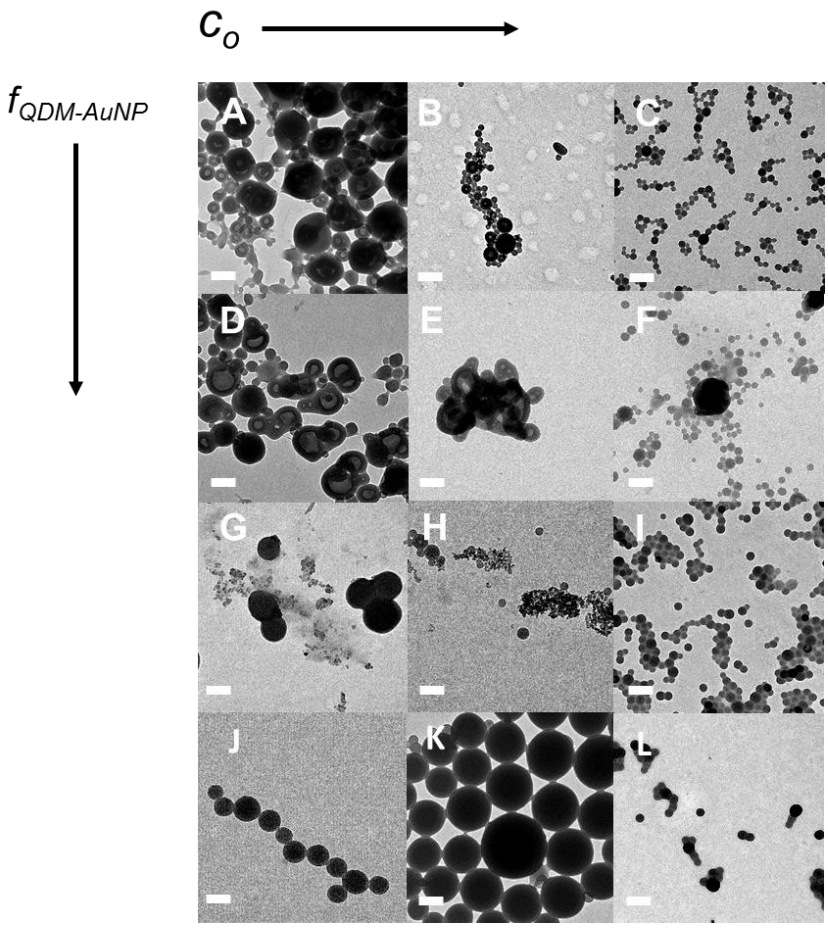

Figure 3-13. Representative TEM micrographs of the various QDCM assemblies, increasing from 0.1 - 0.5 wt% (L-R) and blending ratios of 0 - 0.15 (top to bottom). Scale bar corresponds to 200 nm

TEM imaging (Figure 3-13) shows an interesting trend both as a function of initial solid concentration (c_o) and blending ratio, $f_{QDM\text{-}AuNP}$. In general, an increase in average size as well as polydispersity of QDCMs is observed, matching DLS data. A secondary phenomenon is however visible from TEM that DLS measurements do not reflect. As the concentration and blending ratios increase, there is a morphological transition from primarily vesicles (c_0 = 0 wt%, $f_{QDM\text{-}AuNP}$ = 0) to primarily spheres (c_0 = 0.5 wt%, $f_{QDM\text{-}AuNP}$ = 0.15). This trend is observed for the samples along both c_0 and $f_{QDM\text{-}AuNP}$ independent of one another. At higher magnifications it becomes more apparent that the nanoparticles

locate along the interface of the vesicle wall and the core (Figure 3-14B) followed by a more even distribution throughout the core upon morphological transition to micelles (Figure 3-14 C,D). Note that for the given samples there is limited contrast between the CdSe cores and the PS matrix which surrounds them due to the small size of the CdS cores (~2 nm) and the similar densities of the two materials. As such, the observed particles in the QD-AuCM TEM images are believed to be the AuNPs as they are sufficiently large and dense to provide adequate contrast to the PS background. Similar images collected previously in our group[26] made use of dark field microscopy in order to obtain images of the CdS cores within the QDCMs and should be investigated in the future of this project.

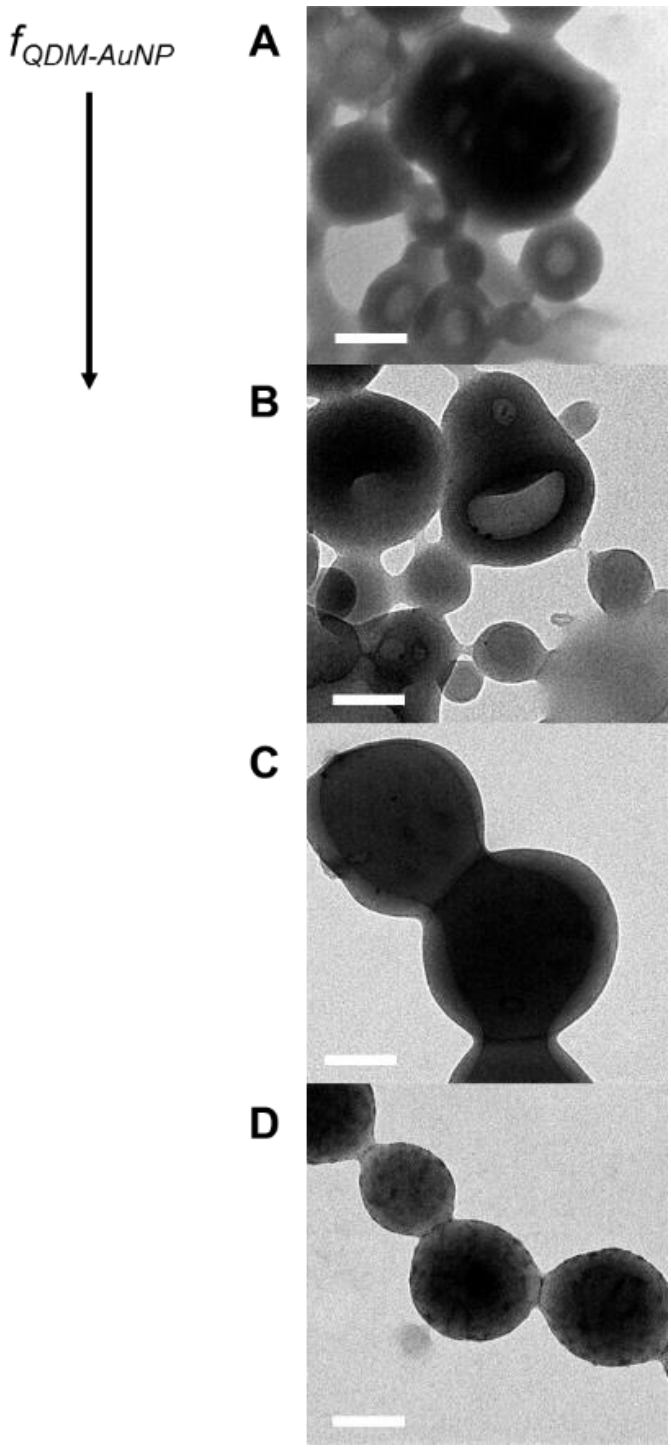

Figure 3-14. High magnification TEM micrographs of the 0.1 wt% QDCM assemblies, with increasing blending ratio from A-D

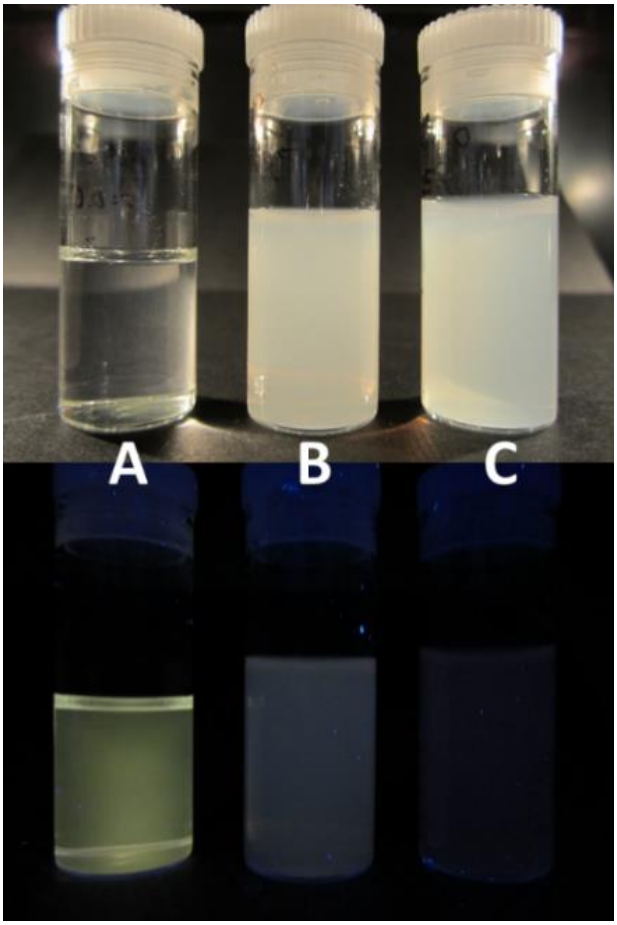

Figure 3-15. Photographs under fluorescent lighting (top) and 365 nm light (bottom) of 0.1 wt%, f = 0.05 QDCM assemblies at the three different QDCM assembly steps, A) addition of single chains, B) addition of 25 wt% water and C) following 24 hours of dialysis.

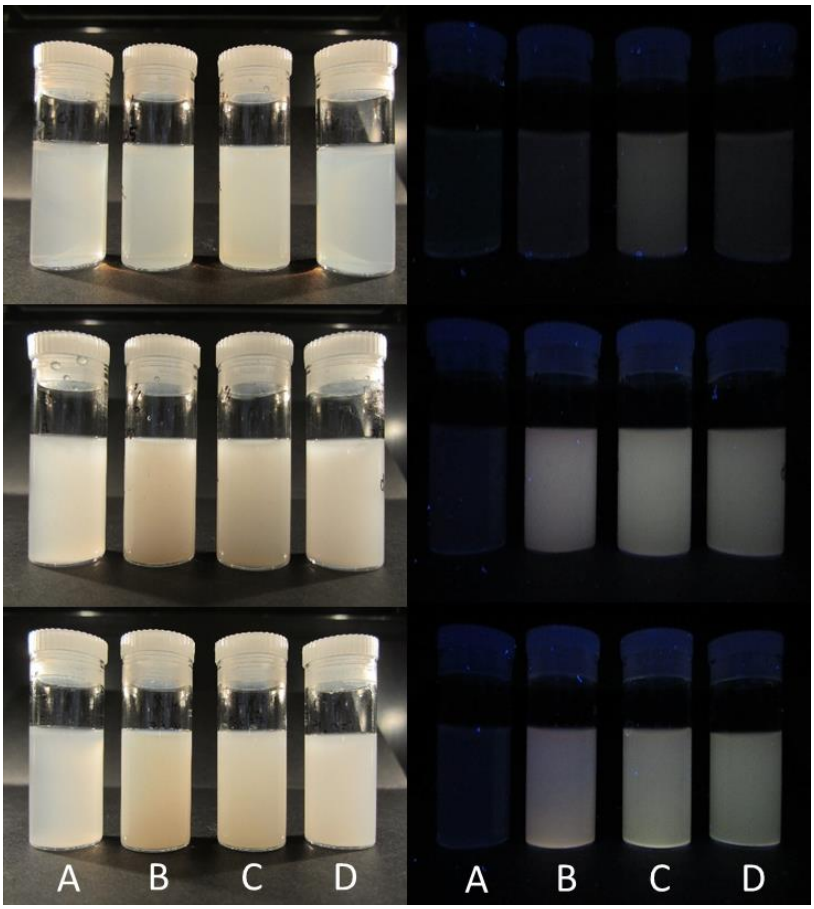

Figure 3-16. Photographs of QDCM assemblies under fluorescent light (left) and 365 nm light (right). Concentrations correspond to 0.1, 0.25 and 0.5 wt% from top to bottom and f= 0, 0.05, 0.1, 0.15 from A-D respectively.

Photographs of the assemblies are provided under ambient and 365 nm illumination (Figure 3-15, Figure 3-16) to demonstrate the dispersal of the QDMs within solution. The drastic increase in sample turbidity, as seen between Figure 3-15A and B, is explained by the formation of QDCMs whose large size scatters substantially more light. These photos are paired with light scattering measurements, and TEM data to verify that the QDM-AuNP assemblies are in fact being partitioned into the QDCM cores. This is easily observed in photographs as any non-encapsulated QDMs would precipitate out of solution very quickly

in the aqueous environment. Any precipitation would be clearly observed following either the dropwise water addition stage or following dialysis.

3.5. Conclusions

The creation and hierarchical self-assembly of RAFT copolymer encapsulated cadmium sulfide quantum dots in the presence of gold nanoparticles was investigated. The use of a RAFT copolymer with a PS block approximately twice as long as that used in the earlier study by a different student from our group was applied to provide emission amplification of the CdS core quantum dots. The emission amplification process with the longer coronal block appears to be sensitive to the molar ratio of sodium sulfide to COO- groups. Despite their deviations in EA response, the follow up experiments clearly demonstrate that the EA methodology can function under different experimental conditions and serves as a promising basis for future study.

In addition to the confirmation of emission amplification, the formation of QDCM assemblies with QDM-AuNP assemblies was investigated for the first time, resulting in the formation of stable compound micelles. Size control, polydispersity and morphologies were investigated as a function of both initial solids concentration and as blending ratios of QDM-AuNPs with QDCM forming single chains. Formation of these particles was confirmed through the use of TEM, DLS and PL measurements. It was observed that as blending ratio and concentration increase, a change in morphology - from vesicles to spheres - was observed in tandem with increases in average particle diameter and polydispersity.

3.6. References

(1) Whitesides, G. M. *Science (80-.).* **2002**, *295* (5564), 2418.

(2) Kirley, M. P.; Aloui, T.; Glass, J. T.; Kirley, M. P.; Aloui, T.; Glass, J. T. *Appl.*

Phys. Lett. **2017**, *233109*.

(3) Hakonen, A.; Svedendahl, M.; Ogier, R.; Yang, Z.-J.; Lodewijks, K.; Verre, R.; Shegai, T.; Andersson, P. O.; Käll, M. *Nanoscale* **2015**, No. April, 9405.

(4) Peksa, V.; Lebrušková, P.; Šípová, H.; Štěpánek, J.; Bok, J.; Homola, J.; Procházka, M. *Phys. Chem. Chem. Phys.* **2016**, No. 29, 19613.

(5) Du, G. X.; Mori, T.; Suzuki, M.; Saito, S.; Fukuda, H.; Takahashi, M. *Appl. Phys. Lett.* **2010**, *96* (8).

(6) Wu, L. Y.; Di Carlo, D.; Lee, L. P. *Biomed. Microdevices* **2008**, *10* (2), 197.

(7) Bains, A.; Cao, Y.; Kly, S.; Wulff, J. E.; Moffitt, M. G. *Mol. Pharm.* **2017**, acs. molpharmaceut.7b00177.

(8) Wang, C.-W.; Sinton, D.; Moffitt, M. G. *J. Am. Chem. Soc.* **2011**, *133* (46), 18853.

(9) Zeng, H.; Li, J.; Liu, J. P.; Wang, Z. L.; Sun, S. *Nature* **2002**, *420* (6914), 395.

(10) Lan, X.; Wang, Q. *Adv. Mater.* **2016**, 10499.

(11) Zheng, J.; Dai, B.; Liu, J.; Liu, J.; Ji, muwei; Liu, J.; Zhou, Y.; Xu, M.; Zhang, J. *ACS Appl. Mater. Interfaces* **2016**, *8* (51), 35426.

(12) Abécassis, B. *ChemPhysChem* **2016**, *17* (5), 618.

(13) Moffitt, M. G. *J. Phys. Chem. Lett.* **2013**, *4*, 3654.

(14) Corbierre, M. K.; Cameron, N. S.; Lennox, R. B. *Langmuir* **2004**, *20* (7), 2867.

(15) Balazs, A. C.; Emrick, T.; Russell, T. P. *Science (80-.).* **2006**, *314* (5802), 1107.

(16) Kim, J. U.; Matsen, M. W. *Phys. Rev. Lett.* **2009**, *102* (7).

(17) Du, J.; O'Reilly, R. K. *Chem. Soc. Rev.* **2011**, *40* (5), 2402.

(18) Staff, R. H.; Gallei, M.; Mazurowski, M.; Rehahn, M.; Berger, R.; Landfester, K.; Crespy, D. *ACS Nano* **2012**, *6* (10), 9042.

(19) Oh, E.; Hong, M. Y.; Lee, D.; Nam, S. H.; Yoon, H. C.; Kim, H. S. *J. Am. Chem. Soc.* **2005**, *127* (10), 3270.

(20) Li, M.; Cushing, S. K.; Wang, Q.; Shi, X.; Hornak, L. A.; Hong, Z.; Wu, N. *J. Phys. Chem. Lett.* **2011**, *2* (17), 2125.

(21) Susumu, K.; Oh, E.; Delehanty, J. B.; Blanco-Canosa, J. B.; Johnson, B. J.; Jain, V.; Hervey, W. J.; Algar, W. R.; Boeneman, K.; Dawson, P. E.; Medintz, I. L. *J. Am. Chem. Soc.* **2011**, *133* (24), 9480.

(22) Shi, Y.; Pan, Y.; Zhang, H.; Zhang, Z.; Li, M. J.; Yi, C.; Yang, M. *Biosens. Bioelectron.* **2014**, *56*, 39.

(23) Huang, D.; Niu, C.; Wang, X.; Lv, X.; Zeng, G. *Anal. Chem.* **2013**, *85* (2), 1164.

(24) Wang, X.; Guo, X. *Analyst* **2009**, *134* (7), 1348.

(25) Yusuf, H.; Kim, W.; Lee, D. H.; Aloshyna, M.; Brolo, A. G.; Moffitt, M. G. *Langmuir* **2007**, *23* (10), 5251.

(26) Yusuf, H.; Kim, W.-G.; Lee, D. H.; Guo, Y.; Moffitt, M. G. *Langmuir* **2007**, *23* (2), 868.

(27) Ribeiro, T.; Prazeres, T. J. V; Moffitt, M.; Farinha, J. P. S. *J. Phys. Chem. C* **2013**, *117*, 3122.

(28) Kulakovich, O.; Strekal, N.; Yaroshevich, A.; Maskevich, S.; Gaponenko, S.; Nabiev, I.; Woggon, U.; Artemyev, M. *Nano Lett.* **2002**, *2* (12), 1449.

(29) Nie, Z.; Petukhova, A.; Kumacheva, E. *Nat. Nanotechnol.* **2010**, *5* (1), 15.

(30) Li, M.; Cushing, S. K.; Wang, Q.; Shi, X.; Hornak, L. A.; Hong, Z.; Wu, N. *J. Phys. Chem. Lett.* **2011**, *2* (17), 2125.

(31) Gueroui, Z.; Libchaber, A. *Phys. Rev. Lett.* **2004**, *93* (16), 1.

(32) Pons, T.; Medintz, I. L.; Sapsford, K. E.; Higashiya, S.; Grimes, A. F.; English, D. S.; Mattoussi, H. *Nano Lett.* **2007**, *7* (10), 3157.

(33) Sperling, L. H. *Introduction to Physical Polymer Science*; John Wiley & Sons, Inc.: New York, 2005.

(34) Keddie, D. J. *Chem. Soc. Rev.* **2014**, *43* (2), 496.

(35) Cowie, J. M. G.; Arrighi, V. *Polymers: Chemistry & Physics of Modern Materials*, 3rd ed.; CRC Press: New York, 2007.

(36) Moad, G.; Rizzardo, E.; Thang, S. H. *Modern Polymerization Techniques*; Sigma-Aldrich Corporation, 2010; Vol. 5.

(37) Mai, Y.; Eisenberg, A. *Chem. Soc. Rev.* **2012**, *41* (18), 5969.

(38) Hamley, I. W. *The Physics of Block Copolymers*; Oxford University Press: New York, 1998.

(39) Hadjichristidis, N.; Pispas, S.; Floudas, G. *Block Copolymers: Synthetic Strategies, Physical Properties, and Applications*; John Wiley & Sons, Inc.: Hoboken, New Jersey, 2003.

(40) Alemán, J. V.; Chadwick, A. V.; He, J.; Hess, M.; Horie, K.; Jones, R. G.; Kratochvíl, P.; Meisel, I.; Mita, I.; Moad, G.; Penczek, S.; Stepto, R. F. T. *Pure Appl. Chem.* **2007**, *79* (10), 1801.

(41) Roduner, E. *Chem. Soc. Rev.* **2006**, *35* (7), 583.

(42) Watkins, S. E.; Jasieniak, J.; Califano, M. *ACS Nano* **2011**, *5* (7), 5888.

(43) Veamatahau, A.; Jiang, B.; Seifert, T.; Makuta, S.; Latham, K.; Kanehara, M.; Teranishi, T.; Tachibana, Y. *Phys. Chem. Chem. Phys.* **2015**, *17* (4), 2850.

(44) Clark, P. C. J.; Radtke, H.; Pengpad, A.; Williamson, A. I.; Spencer, B. F.;

Hardman, J. O.; Leontiadou, M. A.; Neo, D. C. J.; Fairclough, S. M.; Watt, A. A. R.; Pis, I.; Nappini, S.; Bondino, F.; Magnano, E.; Schulte, K.; Silly, M.; Sirotti, F.; Flavell, W. R. *Nanoscale* **2017**, *9*, 6056.

(45) Brus, L. *J. Phys. Chem.* **1986**, *90* (12), 2555.

(46) Lakowicz, J. R. *Principles of Fluorescence Spectroscopy Principles of Fluorescence Spectroscopy*; 2006.

(47) Arora, V.; Soni, U.; Mittal, M.; Yadav, S.; Sapra, S. *J. Colloid Interface Sci.* **2017**, *491*, 329.

(48) Ye, Y.; Wang, X.; Ye, S.; Xu, Y.; Feng, Z.; Li, C. *J. Phys. Chem. C* **2017**, *121* (32), 17112.

(49) Mattoussi, H.; Radzilowski, L. H.; Dabbousi, B. O.; Fogg, D. E.; Schrock, R. R.; Thomas, E. L.; Rubner, M. F.; Bawendi, M. G. *J. Appl. Phys.* **1999**, *86* (2001), 4390.

(50) Wang, C.-W.; Moffitt, M. G. *Langmuir* **2004**, *20* (26), 11784.

(51) Luther, J. M.; Jain, P. K.; Ewers, T.; Alivisatos, A. P. *Nat Mater* **2011**, *10* (5), 361.

(52) Noguez, C. *J Phys Chem C* **2007**, 3806.

(53) Jin, Y.; Gao, X. *Nat. Nanotechnol.* **2009**, *4* (9), 571.

(54) Quach, A. D.; Crivat, G.; Tarr, M. A.; Rosenzweig, Z. *J. Am. Chem. Soc.* **2011**, *133* (7), 2028.

(55) Lee, J.; Govorov, A. O.; Kotov, N. A. *Angew. Chemie - Int. Ed.* **2005**, *44* (45), 7439.

(56) Zeng, Q.; Zhang, Y.; Liu, X.; Tu, L.; Kong, X.; Zhang, H. *Chem. Commun.* **2012**, *48* (12), 1781.

(57) Zhang, N.; Liu, S.; Xu, Y.-J. *Nanoscale* **2012**, *4*, 2227.

(58) Fedutik, Y.; Temnov, V.; Woggon, U.; Ustinovich, E.; Artemyev, M. *J. Am. Chem. Soc.* **2007**, *129* (48), 14939.

(59) Liu, N.; Prall, B. S.; Klimov, V. I. *J. Am. Chem. Soc.* **2006**, *128* (48), 15362.

(60) Chen, C. W.; Wang, C. H.; Wei, C. M.; Chen, Y. F. *Appl. Phys. Lett.* **2009**, *94* (7), 10.

(61) Lee, J.; Govorov, A. O.; Kotov, N. a. *Angew. Chemie - Int. Ed.* **2005**, *44* (45), 7439.

(62) Moffitt, M.; Eisenberg, A. *Macromolecules* **1997**, *30* (15), 4363.

(63) Foerster, S.; Zisenis, M.; Wenz, E.; Antonietti, M. *J. Chem. Phys.* **1996**, *104* (24), 9956.

(64) Murphy, D. B.; Davidson, M. W. *Fundamentals of Light Microscopy and Electronic Imaging*, 2nd ed.; Wiley-Blackwell, 2012.

(65) IUPAC. *Compendium of Chemical Terminology*, 2nd ed.; IUPAC, 1996.

(66) Gazit, O.; Khalfin, R.; Cohen, Y.; Tannenbaum, R.; Gazit, O.; Khalfin, R.; Cohen, Y.; Tannenbaum, R. *J. phys chem C* **2009**, 576.

(67) Cerdán, L.; Costela, A.; Enciso, E.; García-Moreno, I. *Adv. Funct. Mater.* **2013**, *23*, 3916.

(68) Toor, A.; Feng, T.; Russell, T. P. *Eur. Phys. J. E* **2016**, *39* (5).

(69) Thiermann, R.; Bleul, R.; Maskos, M. *Macromol. Chem. Phys.* **2017**, *218* (2), 1600347.

(70) Klok, H. A.; Lecommandoux, S. *Adv. Mater.* **2001**, *13* (16), 1217.

(71) Armao, J. J.; Nyrkova, I.; Fuks, G.; Osypenko, A.; Maaloum, M.; Moulin, E.;

Arenal, R.; Gavat, O.; Semenov, A. N.; Giuseppone, N. *J. Am. Chem. Soc.* **2017**, jacs. 6b11179.

(72) Liang, R.; Xu, J.; Li, W.; Liao, Y.; Wang, K.; You, J.; Zhu, J.; Jiang, W. *Macromolecules* **2015**, *48* (1), 256.

(73) Kim, S. H.; Misner, M. J.; Xu, T.; Kimura, M.; Russell, T. P. *Adv. Mater. (Weinheim, Ger.* **2004**, *16* (3), 226.

(74) Xu, Z.; Xue, P.; Gao, Y. E.; Liu, S.; Shi, X.; Hou, M.; Kang, Y. *J. Colloid Interface Sci.* **2017**, *490*, 511.

(75) Yu, H. *Prog. Polym. Sci.* **2014**, *39* (4), 781.

(76) Nepal, D.; Drummy, L. F.; Biswas, S.; Park, K.; Vaia, R. a. *ACS Nano* **2013**, *7* (10), 9064.

(77) Cui, Q.; He, F.; Li, L.; Möhwald, H. *Adv. Colloid Interface Sci.* **2014**, *207* (1), 164.

(78) Zhang, C.; Ding, C.; Zhou, G.; Xue, Q.; Xian, Y. *Anal. Chim. Acta* **2017**, *957*, 63.

(79) Sasidharan, A.; Monteiro-Riviere, N. A. *Wiley Interdiscip. Rev. Nanomedicine Nanobiotechnology* **2015**, *7* (6), 779.

(80) Pelaz, B.; Charron, G.; Pfeiffer, C.; Zhao, Y.; de la Fuente, J. M.; Liang, X.-J.; Parak, W. J.; Del Pino, P. *Small* **2013**, *9* (9–10), 1573.

(81) Khullar, P.; Singh, V.; Mahal, A.; Kumar, H.; Kaur, G.; Bakshi, M. S. *J. Phys. Chem. B* **2013**, *117* (10), 3028.

(82) Krishnan, D.; Johnson, H. T. *J. Mech. Phys. Solids* **2014**, *62*, 48.

(83) Knaapila, M.; Monkman, A. P. *Adv. Mater.* **2013**, *25* (8), 1090.

(84) Brust, M.; Walker, M.; Bethell, D.; Schiffrin, D. J.; Whyman, R. *J. Chem. Soc., Chem. Commun.* **1994**, 801.

(85) Moffitt, M.; McMahon, L.; Pessel, V.; Eisenberg, a. *Chem. Mater.* **1995**, *7* (6), 1185.

(86) Ringler, M.; Schwemer, A.; Wunderlich, M.; Nichtl, A.; Kürzinger, K.; Klar, T. A.; Feldmann, J. *Phys. Rev. Lett.* **2008**, *100*, 203002.

(87) Hrelescu, C.; Sau, T. K.; Rogach, A. L.; Frank, J.; Laurent, G.; Douillard, L. *Nano Lett.* **2011**, *11*, 402.

Chapter 4 - Conclusions and Future Work

4.1. Conclusions

In this work we have detailed the synthesis and characterization of amphiphilic tetrablock PS-*b*-PAA RAFT copolymer encapsulated cadmium selenide and cadmium sulfide based quantum dots. Additionally, initial investigations into the self-assembly of QD-AuCM was described. The techniques established for these systems provide a solid ground work for use of these materials as building blocks for subsequent self-assembly applications.

In Chapter 2 the methodology to synthesize cadmium selenide quantum dots within tetrablock RAFT copolymers was established. The CdSe quantum dots in a mixture of dioxane and toluene demonstrate a sharp, slightly Stokes shifted emission peak upon excitation by incident light around 470 nm. In order to determine optimal synthetic conditions, the careful analysis of the synthetic process across three common organic solvents (dioxane, THF, and DMF) was required for future works on the self-assembly of these materials. Through a combination of experimental design and computational analysis it was determined that in THF and DMF, the PAA block of the RAFT copolymer demonstrated aggregation. This aggregation prevents the formation and dispersal of quantum dot containing polymeric micelles in solution. It is visible from emission and absorption spectra that while there are CdSe quantum dots present in the THF and DMF based samples, the macroscopic turbidity and precipitation indicate large scale aggregation of these materials. This chapter strives to promote the expansion of work from the CdS analogues previously explored in our group.[27] Through the study of a range of different

quantum dot cores, a library can be developed for polymer encapsulated quantum dots as building blocks for future applications.

The contribution to original knowledge chapter 2 provides is two-fold: expansion on the fabrication of cadmium sulfide quantum dot micelles frequently examined within our group to include cadmium selenide based systems, and a detailed analysis of solvent composition on the self-assembly of tetrablock PAA-*b*-PS-TTC-PS-*b*-PAA RAFT block copolymers. The diversification of quantum dot production within these structures serves as a stepping stone toward the creation of a library of materials with different physical properties, *e.g.* fluorescence profiles, to be selected at an investigators discretion. Understanding the influence of solvent composition on the assembly process establishes experimental limitations/considerations for these materials in future applications.

Chapter 3 saw an investigation into the formation of RAFT-CdS/AuNP structures and the study of their physical properties. Specifically, this chapter builds upon research previously investigated in this group[27] through the analysis of the emission amplification process with a longer polystyrene block length on the RAFT copolymer. Due to the distance dependent nature of emission amplification in the QD-AuNP system the study of their response to variable brush lengths is germane to the determination of their applicability moving forward. It was determined that despite the increased length of the PS coronal chains, the current samples also exhibit emission amplification. As in the case of the initial investigation, these samples demonstrate increasing emission amplification with higher AuNP concentration and with increasing excitation wavelength.

In the second half of chapter 3, self-assembly of the QDM-AuNP system used in EA calculations was investigated. Based around initial investigations from our group,[25,26]

a methodology for the preparation of QD-AuCM was developed and explored across a range of blending ratios, $f_{QDM\text{-}AuNP}$ = 0, 0.05, 0.1, 0.15 and initial solid concentrations, c_0 = 0.1, 0.25 and 0.5 wt%. It was determined that with increasing blending ratio and initial solid concentration, average QD-AuCM diameters increased. In tandem with an increase in average particle size, it was determined that the systems demonstrate a morphology change from primarily vesicles at low blending ratios and initial concentration to primarily spheres at high blending ratios and initial concentrations. The careful analysis of how these particles behave within the parameter space allows for isolation of a desirable sample property, *e.g*. morphology or size, for further investigations into the emission amplification process or evaluation of structure-function relationship of these assemblies.

Chapter 3 contributes to the breadth of self-assembled QDMs previously investigated within our research group.[25–27] Specifically, in the first half of chapter 3 we demonstrate that the emission amplification process works at two different coronal block lengths, adding to the repertoire of available structures available for future self-assembly processes. The second half of chapter 3 expands on the formation of QDCMs from PS-*b*-PAA encapsulated QDs investigated in our group[25,26] through the use of a different polymer system, beginning with the tetrablock RAFT copolymer in lieu of the PS-*b*-PAA unimer, with the incorporation of AuNPs. As with each previous step of this assembly process, the introduction of functionality is desirable as it provides a foothold on new areas of exploration.

4.2. Future Work

The most important work required to continue the projects listed directly in this thesis lies in the investigation of the QD-AuCM assemblies. Initial investigations presented

in Chapter 3 are based around single measurements of these systems and as such a minimum of triplicates must be performed in order to determine whether these trends remain constant and if not, how do they vary? Aside from replicate measurements, investigations into different blend ratios above the $f_{QDM\text{-}AuNP} = 0.35$ should be investigated for these systems alongside investigations into total water content, rate of water addition and finally with increasing gold concentrations. Following determination of the parameter space for compound micelle formation, methodology must be developed for the characterization of emission amplification within these superstructures.

A clear beginning project based around the cadmium selenide system lies in the replication of the work completed in Chapter 3; specifically, characterize the interaction and influence of gold nanoparticles on the emissive properties of the CdSe QDs. It stands to reason that the methodology applied to this research will mirror that established from our original paper on the subject[27] as well as that completed in chapter 3. Following investigation into the emission amplification process with cadmium selenide analogues, subsequent exploration of quantum dot compound micelle formation can be investigated.

A related project to those investigated in chapters 2 and 3 would be analogues composed of commercially available PS-*b*-PAA block copolymers. The purpose of this project would be to establish methodology with commercially available polymers, negating the requirement for the use of highly specialized RAFT copolymer. This will provide the ability for investigators to rapidly explore a wide array of parameters such as variable block lengths, as there is a considerable variation in the commercial availability of these polymers. The emission amplification process under this polymer system, if it is present,

will not be visible until assembly into the QD-AuCMs as the AuNPs will have no reason to be associated to the QDM cores as a result of the loss of the thiol terminus.

Following the completion of these projects, the methodologies for the formation and characterization of these micellar building blocks will be established and as such new realms of investigation will be opened. These may entail the investigation into the formation of different quantum dot cores, *e.g.* CdTe, exploration of the formation of core/shell structures within the micellar cores, *e.g.* CdS/CdSe, or investigations into the effect of core size on the emission amplification process. Building upon the QD-AuCM work, investigations into assembly of these structures into highly ordered materials can be investigated. This would resemble the assembly work performed by our group[25,26] in order to determine the influence of the material's structure or particle composition on the functionality of the system.

The projects detailed in this thesis in addition to the proposed work above are various facets of the overarching project to generate a library of self-assembled materials (or the methodology for their assembly) which can be selected for a given property, *e.g.* optical, electronic, mechanical, solubility, *etc.* For example, if a researcher is interested in sensing capabilities the choice of QD core can be selected for compatibility with the matrix, *i.e.* targeted emission wavelengths, with an optimized AuNP concentration for desired emission amplification response. To this end, future investigations should be oriented around understanding the interplay of structure and functionality for these assemblies.

Appendix A:

Relating to the Supporting Information for Chapter 2

System	Oligomer	Solvent	Salt	L (nm)
SE-THF	SE	THF	No	7.05
SA-THF	SA	THF	No	7.01
SA-THF/Li	SA	THF	Yes	7.12
SA-dioxane	SA	Dioxane	No	7.39
CE-THF	CE	THF	No	7.03
CA-THF	CA	THF	No	6.99
CA-THF/Li	CA	THF	Yes	7.10

Figure A2.1. Composition of the systems by MD simulations. The length of the square PBC box (L) was adjusted to reproduce a macroscopic density of ca. 0.9 g cm^{3-}. The simulations used 10 oligomer chains and 2000 solvent molecules (plus 200 Cl^- anions and 200 Li^+ cations with added salt).

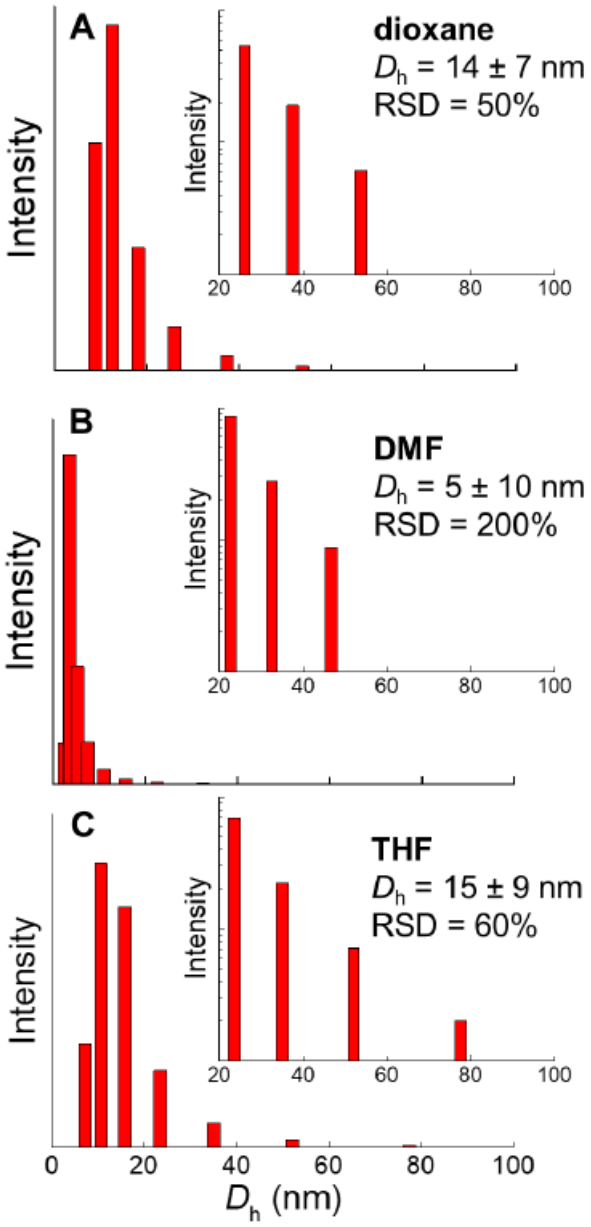

Figure A2.2. Hydrodynamic diameter (D_h) number distributions obtained by CONTIN analysis of the DLS measurements of cadmium acrylate-core micelles in 1,4-dioxane (A), DMF (B) and THF (C). The average values of D_h were calculated directly from the histograms (presented with the width of the distribution and the corresponding relative standard deviations, *RSD*). The insets show one the larger aggregates in number fraction logarithmic scale.

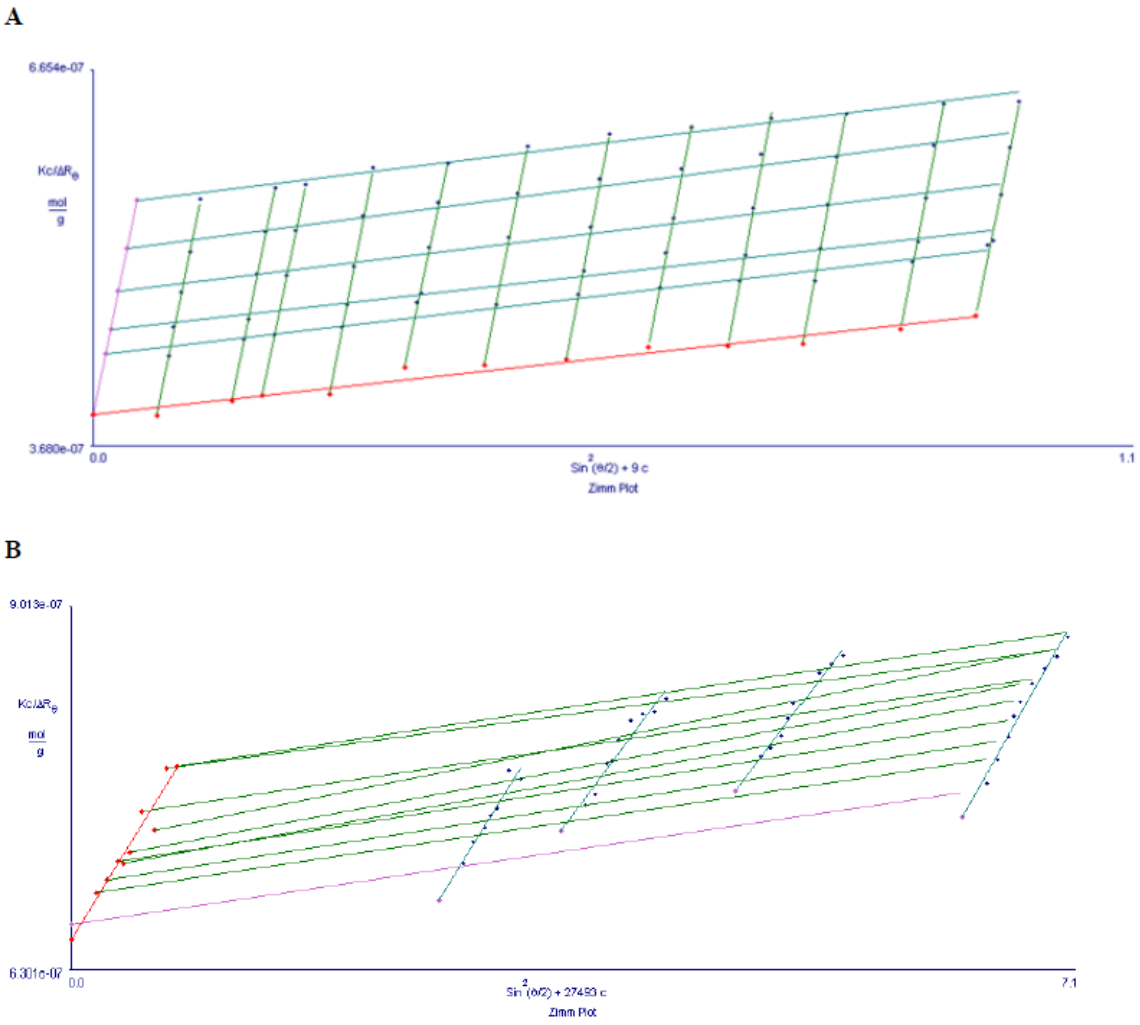

Figure A2.3. Zimm plots of (A) CdAc micelles in filtered 1,4-dioxane and of (B) QDMs in a 50/50 mixture of 1,4-dixane:toluene (v/v).

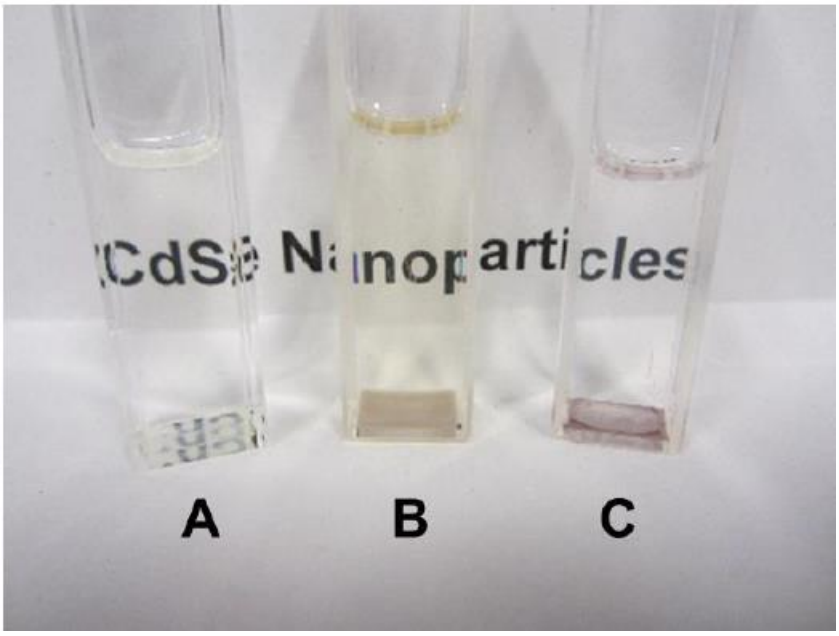

Figure A2.4. Photograph of the three solvent composition samples under ambient light after overnight settling. Samples A-C correspond to Dioxane/Toluene, DMF/Toluene and THF/Toluene mixtures respectively. Precipitate is seen at the bottom of the cuvettes in the B and C cases.

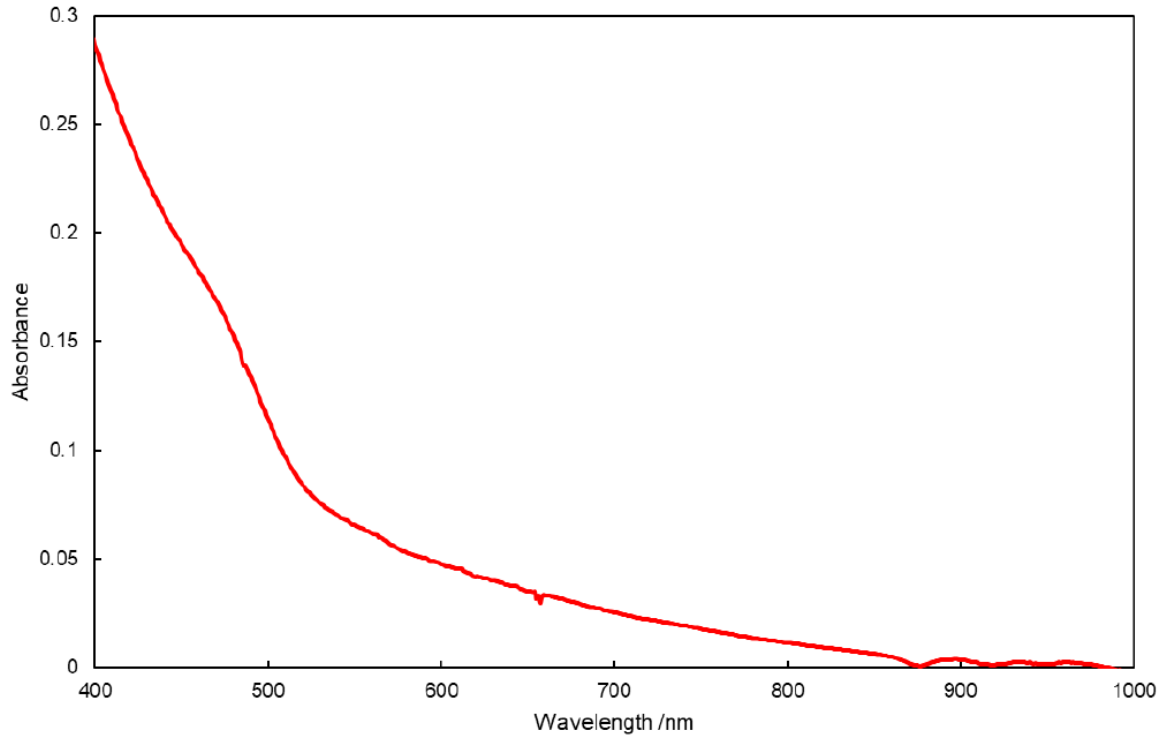

Figure A2.5. UV-vis spectra of the QDMs prepared in Dioxane, in a 50/50 mixture (v/v) of Dioxane/Toluene.

Figure A2.6.

Comparing QDM aggregation numbers calculated from different data:

1. From the molecular weight of an individual block copolymer chain (Mn,chain = 14900 g/mol) and the molecular weight of a QDM (Mw,QDM = 1.2 x 10^6 g/mol), we obtain an aggregation number of Nagg = 80 (Nagg = Mw,QDM /Mn,chain). This is a weight-average aggregation number from light scattering.

2. Alternatively, the QDM aggregation number can be calculated from QD diameters measured by TEM in the following manner:

For the mean QD diameter determined from TEM (d_{QD} = 3 nm), the volume of the QD is $V_{QD} = 4/3\pi r_{QD}^3 =$ 1.413 x 10^{-20} cm^3.

Using the density of CdSe, ρ_{CdSe} = 5.82 g/cm^3, the mass of a QD is

$m_{QD} = V_{QD} \times \rho_{CdSe}$ = 8.224 x 10^{-20} g.

The molar mass of a single CdSe unit is M_{CdSe} = 191.377 g mol-1, so the number of Cd2+ ions in each QD is

$N_{Cd2+,QD} = (m_{QD} / M_{CdSe}) \times N_A$ = 259.

Each chain contributes 39 acrylic acid repeat units ($N_{AA,chain}$) and each two of these repeat units bind a Cd^{2+} ion.

This gives a QDM aggregation number of:

$N_{agg} = N_{Cd2+,QD} \times 2 / N_{AA,chain}$ = 13

This is a number-average aggregation number from TEM.

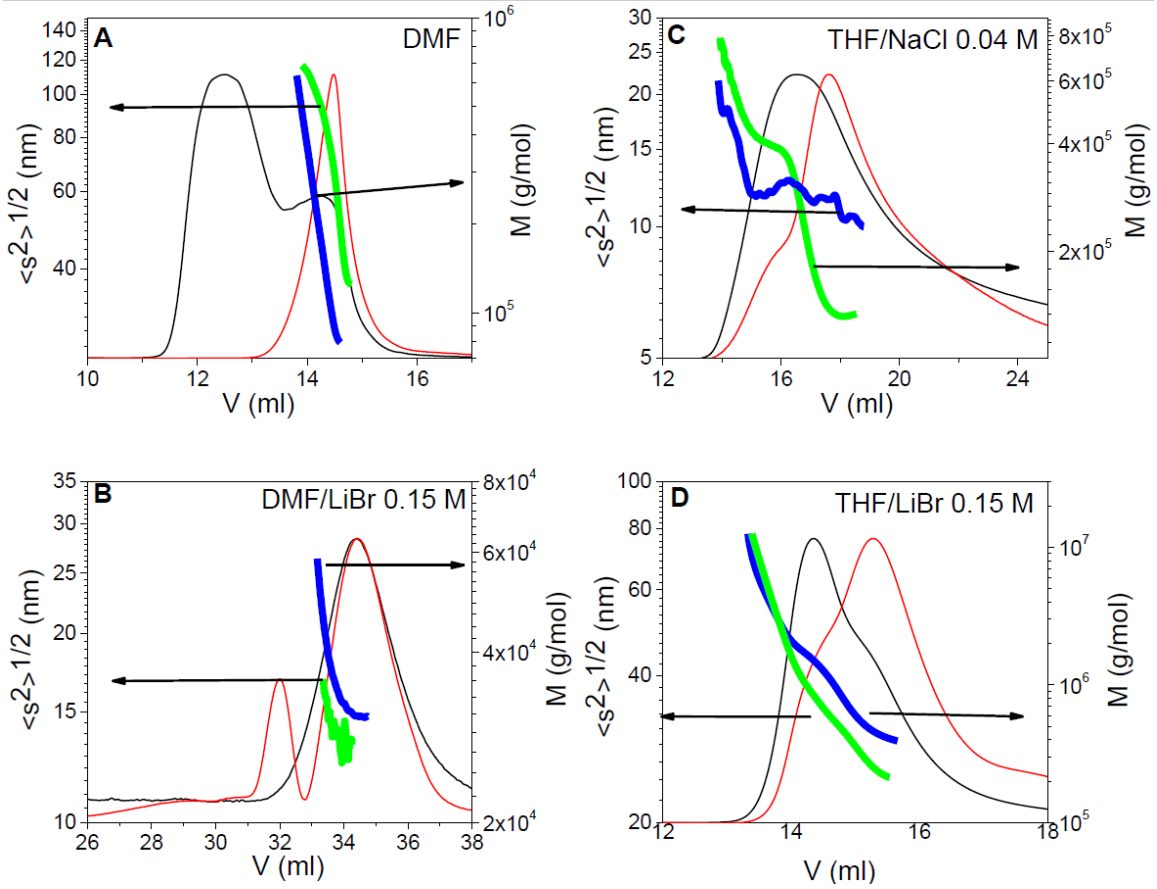

Figure A2.7. Refractive index signal (red) and the MALS signal at 90° (black) versus elution volume. Molecular weight (blue) and radius of gyration (green) calculated for each elution volume for the copolymer solutions in DMF (A); DMF with 0.15 M LiBr (B); THF with 0.04 M NaCl (C); and THFwith 0.15 M LiBr (D)

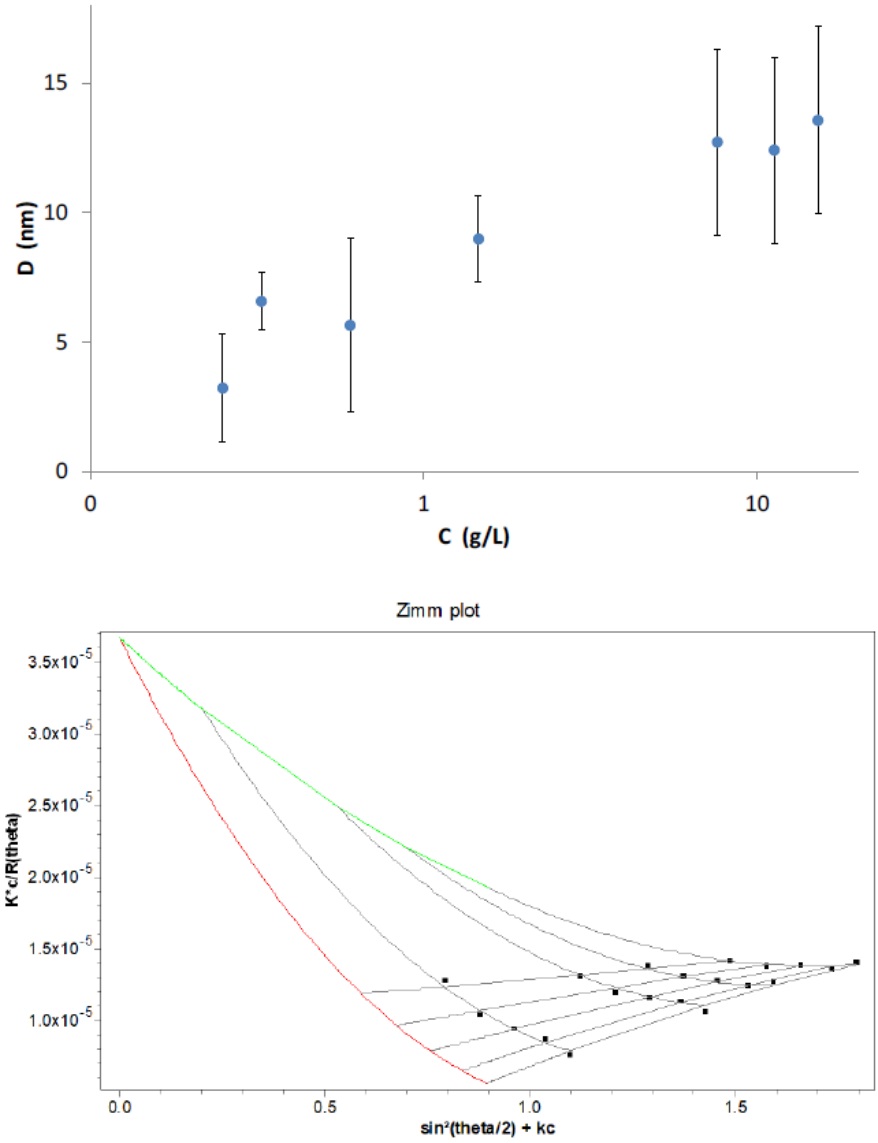

Figure A2.8. Average hydrodynamic diameter calculated from the number-weighted distribution obtained by dynamic light scattering of the PAA-*b*-PS-TTC-PS-*b*-PAA copolymer in 1,4-dioxane. **(B)** Zimm plot of PAA-*b*-PS-TTC-PS-*b*-PAA in Dioxane. The small amount of aggregation at high polymer concentrations affect static light scattering (SLS) measurements, leading to a large error in the Zimm plot slope of the (very weak) concentration dependence, so that it was not possible to determine the second virial coefficient and radius of gyration. The molecular weight, obtained from the intercepts, has much lower error, M_w = (1.7 ± 0.4) x 10^4, and is in very good agreement with SEC-MALS results.

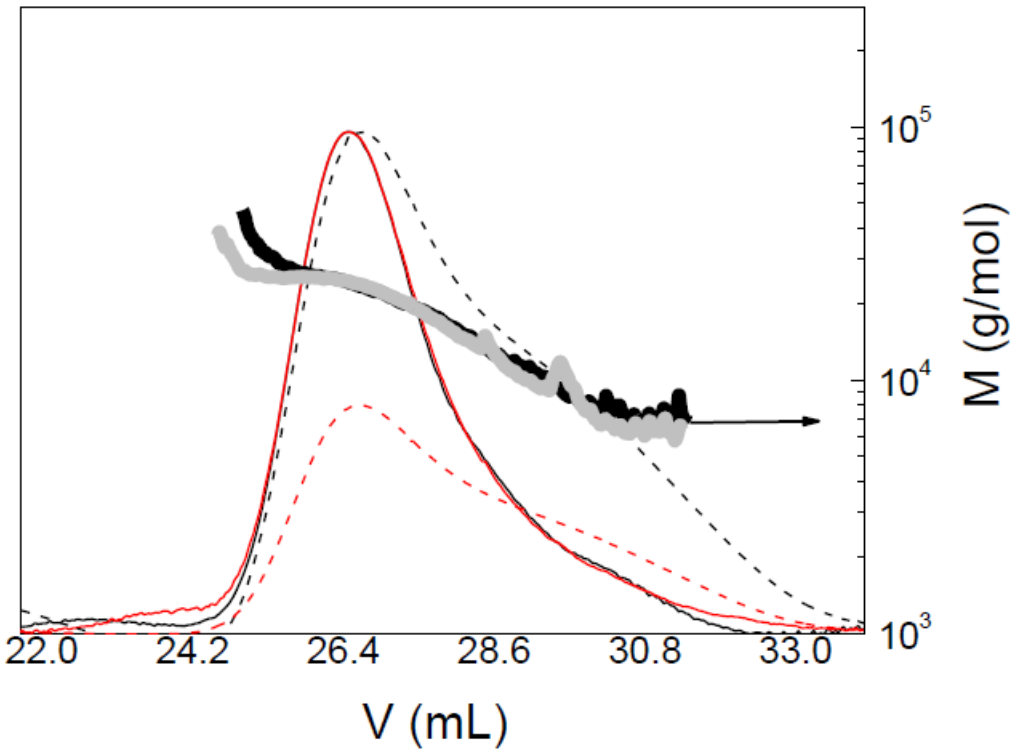

Figure A2.9. Juxtaposed traces of the refractive index signal (dashed curve) and the MALS signal at 90° (solid curve) for two injections of the copolymer in 1,4-dioxane at concentrations 4 mg/mL (red) and 9 mg/mL (black), and the corresponding molecular weight calculated for each elution volume for the 4 mg/mL (gray) and 9 mg/mL (black) solutions.

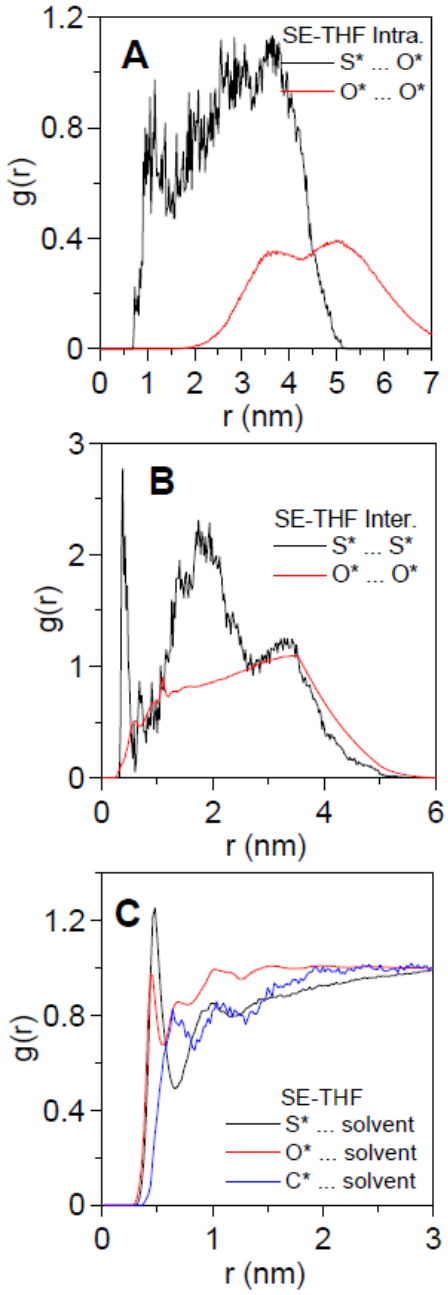

Figure A2.10. Radial correlation functions *g*(r) for the SE-THF system calculated from the MD trajectories. (A) Average intramolecular distances: from the central S* atom to the 22 O* atoms (*black*); from the 11 O* atoms in one block to the 11 O* atoms in the opposite block (*red*). (B) Average intermolecular distances: between the central S* atoms of different chains (*black*); from the 22 O* atoms in one chain to the 22 O* atoms in another chain (*red*). (C) Average distances from the center of mass of the solvent molecules to: the central S* atom (*black*), the 22 O* atoms (*red*), and the 20 C* atoms (*blue*) in one chain.

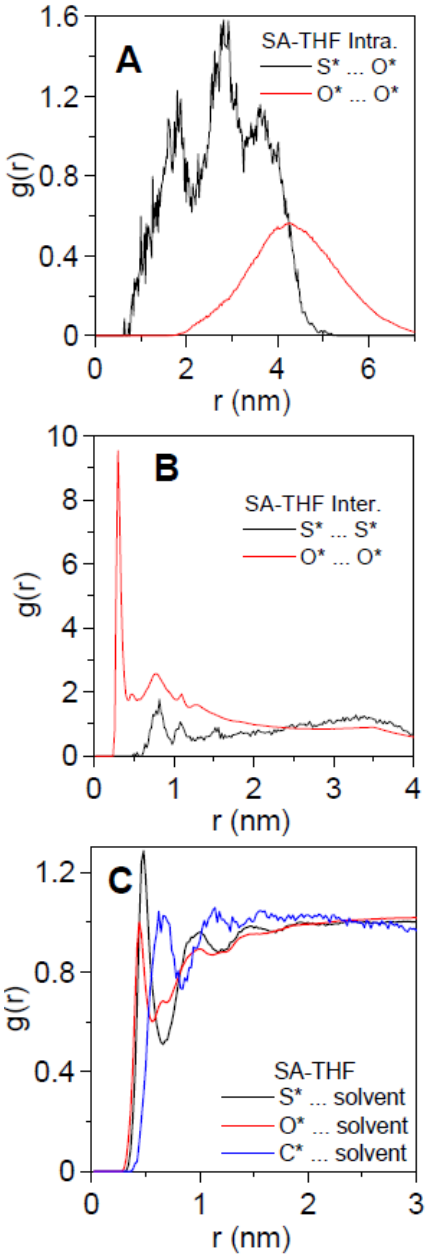

Figure A2.11. Radial correlation functions $g(r)$ for the distances of the SA-THF system calculated from the MD trajectories. (A) Average intramolecular distances: from the central S* atom to the 22 O* atoms (*black*); from the 11 O* atoms in one block to the 11 O* atoms in the opposite block (*red*). (B) Average intermolecular distances: between the central S* atoms of different chains (*black*); from the 22 O* atoms in one chain to the 22 O* atoms in another chain (*red*). (C) Average distances from the centre of mass of the solvent molecules to the central S* atom in one oligomer chain (black); the 22 O* atoms in one oligomer chain (red); and from the 20 C* atoms in one oligomer chain (blue).

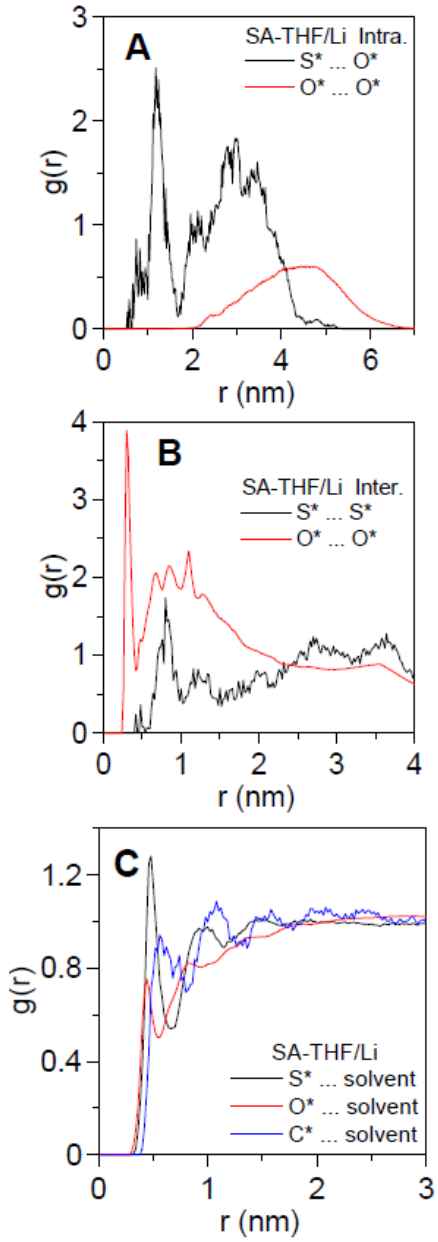

Figure A2.12. Radial correlation functions $g(r)$ for the distances of the SA-THF/Li system calculated from the MD trajectories. (A) Average intramolecular distances: from the central S* atom to the 22 O* atoms (*black*); from the 11 O* atoms in one block to the 11 O* atoms in the opposite block (*red*). (B) Average intermolecular distances: between the central S* atoms of different chains (*black*); from the 22 O* atoms in one chain to the 22 O* atoms in another chain (*red*). (C) Average distances from the centre of mass of the solvent molecules to the central S* atom in one oligomer chain (black); the 22 O* atoms in one oligomer chain (red); and from the 20 C* atoms in one oligomer chain (blue).

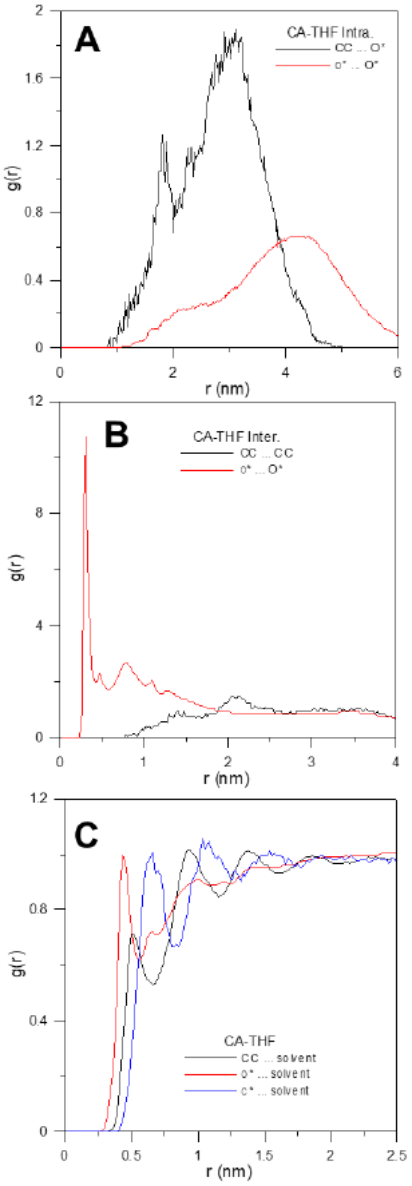

Figure A2.13. Values of the radial correlation function $g(r)$ for the distances of the CA-THF system (CA oligomer in THF) calculated from the MD trajectories. (A) Average intramolecular distances from the central CC atom to the 22 O* atoms (black); and from the 11 O* atoms in one block of the oligomer chain to the 11 O* atoms in the opposite block (red). (B) Average intermolecular distances between the central CC atoms of different oligomer chains (black); and from the 22 O* atoms in one oligomer to the 22 O* atoms in another chain (red). (C) Average distances from the centre of mass of the solvent molecules to the central CC atom in one oligomer chain (black); the 22 O* atoms in one oligomer chain (red); and from the 22 C* atoms in one oligomer chain (blue).

Appendix B:
Relating to the Supporting Information for Chapter 3

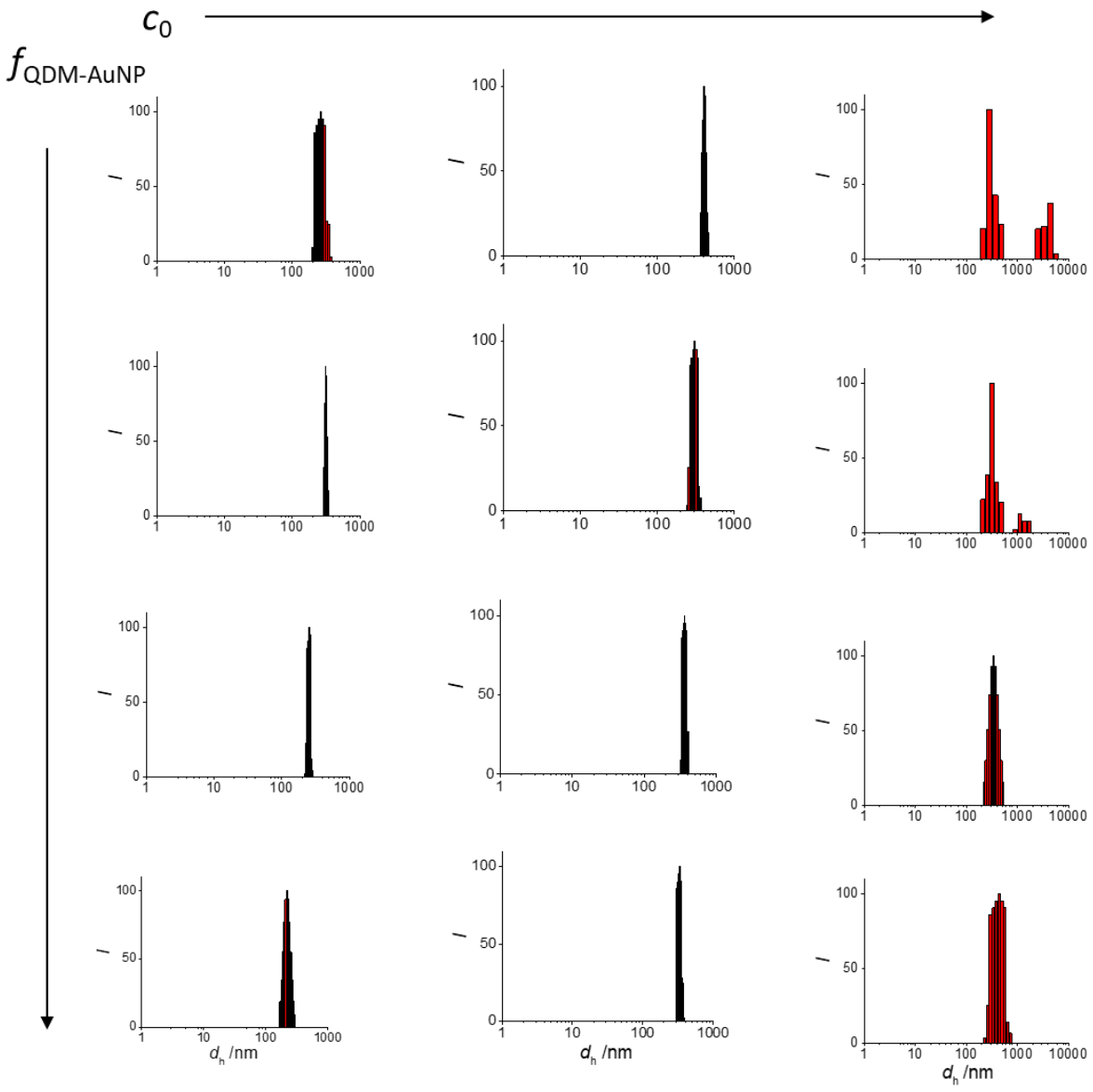

Figure B3.1. DLS CONTIN histograms of QDCM assemblies with increasing initial concentration (L-R) and increasing blending ration (Top-Bottom).

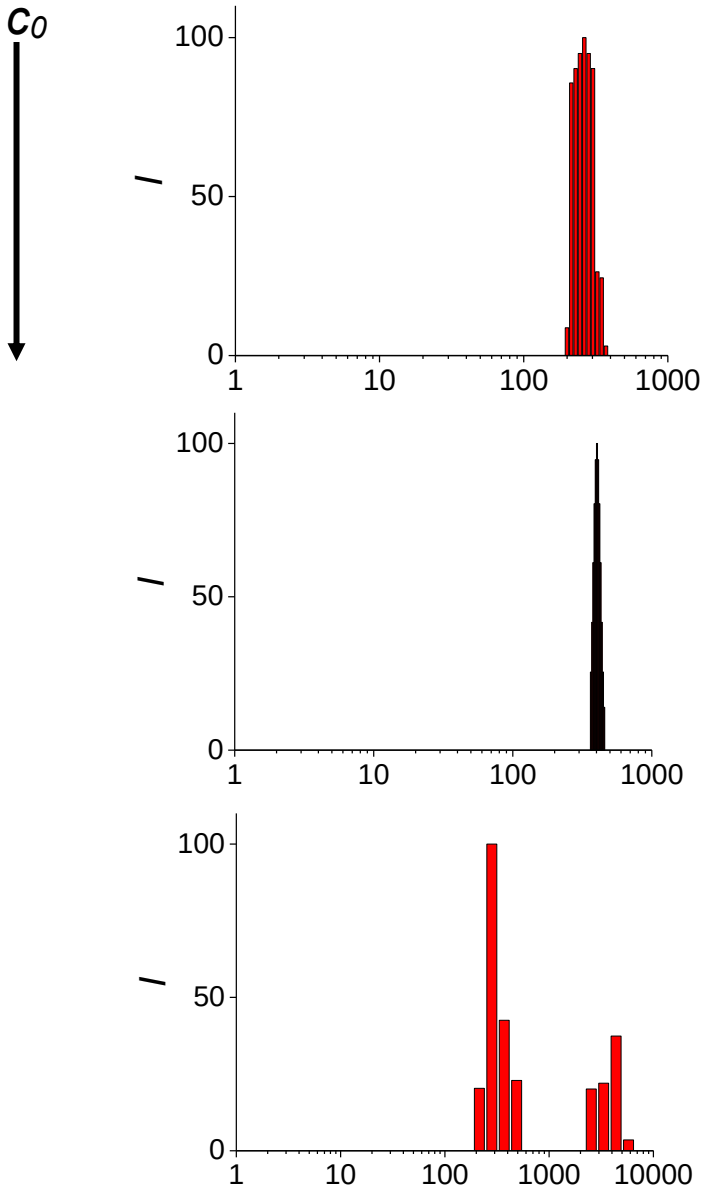

Figure B3.2. Influence of initial concentration ranging from 0.1 to 0.5 wt% from top to bottom at a blending ratio of 0.

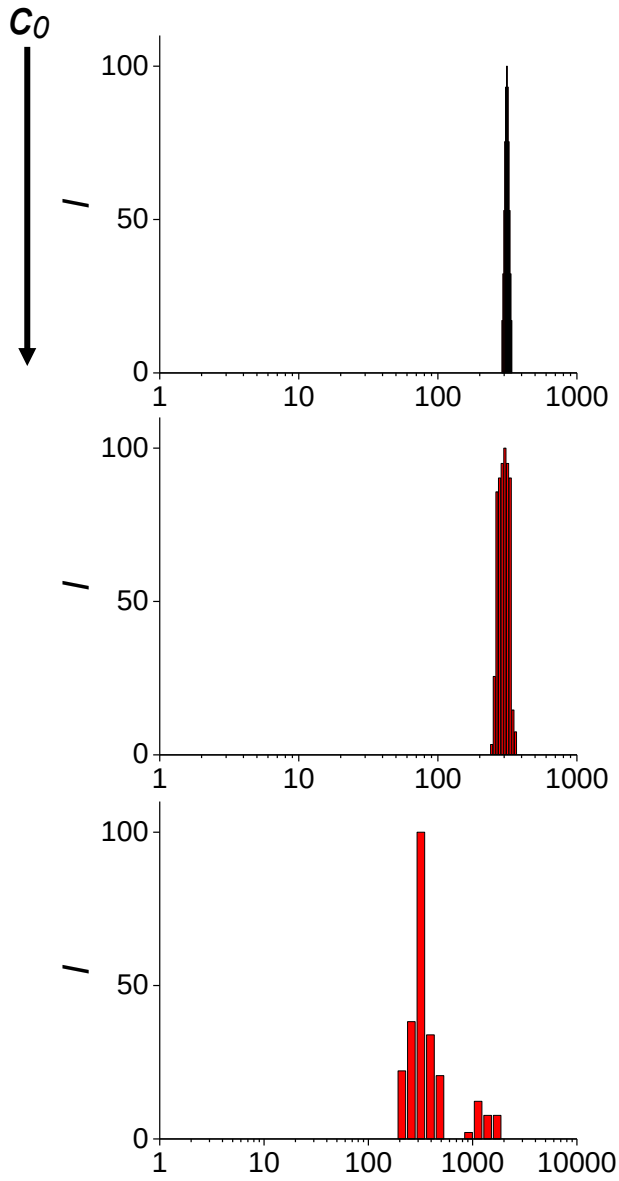

Figure B3.3. Influence of initial concentration ranging from 0.1 to 0.5 wt% from top to bottom at a blending ratio of 0.05.

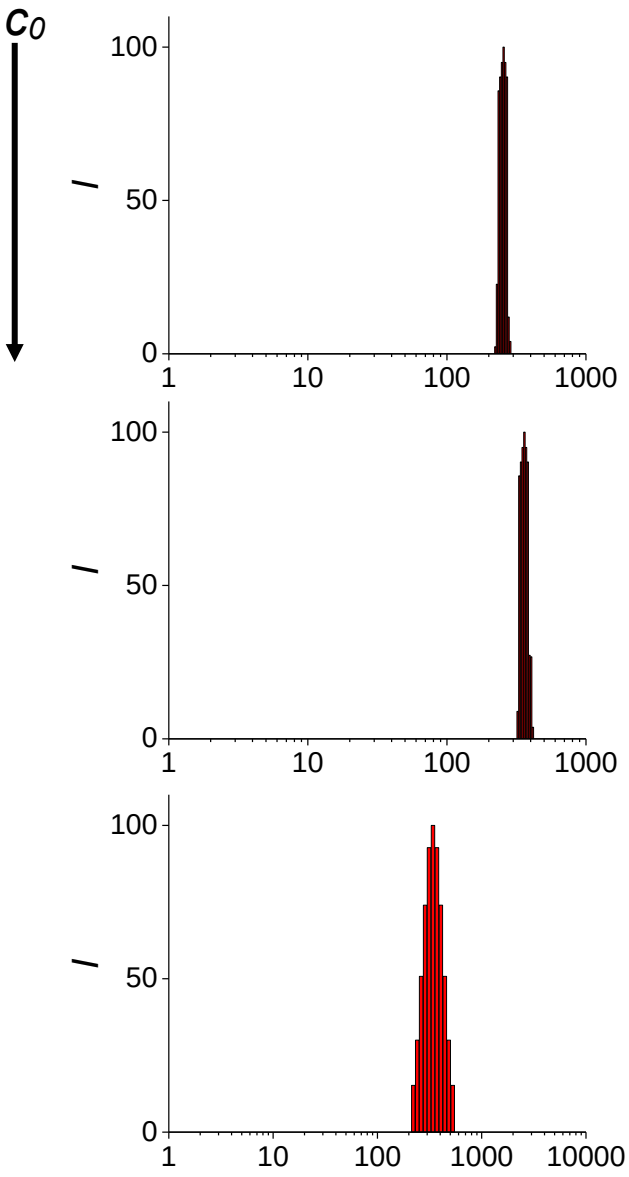

Figure B3.4. Influence of initial concentration ranging from 0.1 to 0.5 wt% from top to bottom at a blending ratio of 0.1.

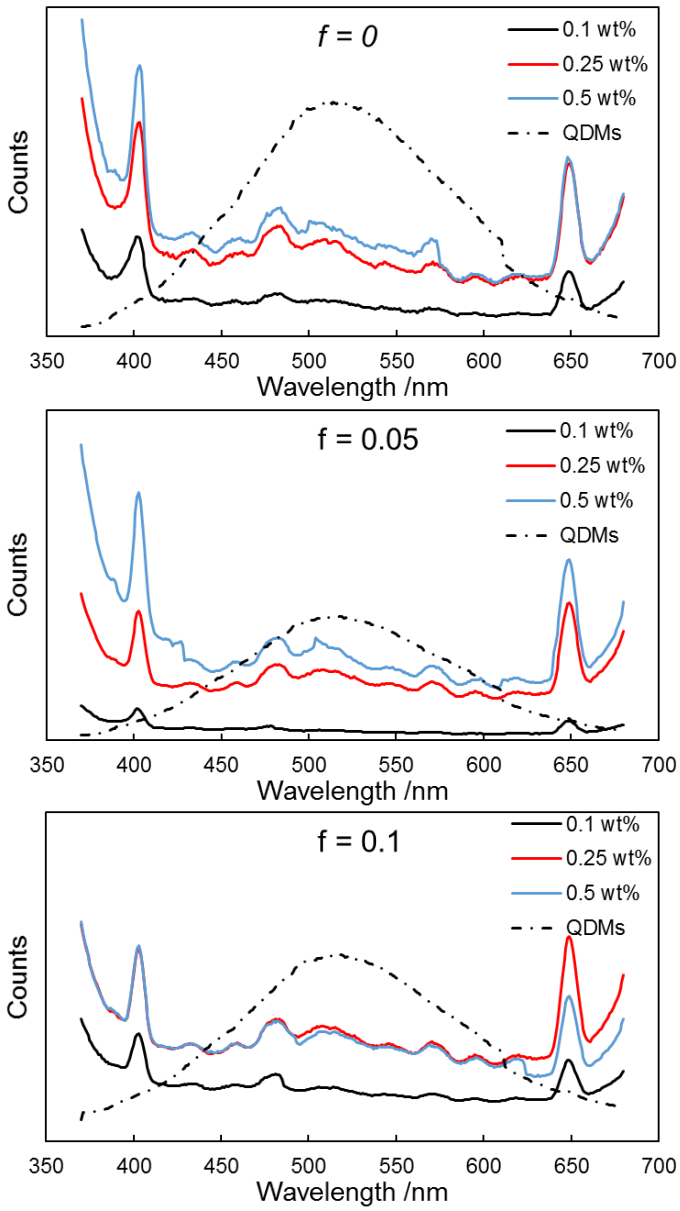

Figure B3.5. Emission spectra collected at 350 nm excitation, at an initial concentration of 0.5 wt% at three different blending ratios.